A New Combined Detection System for STXM and the Applicability of (CdSe)ZnS Nanocrystals to SLXM

A Thesis Presented

by

Simon Karl Moser

to

The Graduate School

in Partial Fulfillment of the Requirements

for the Degree of

Master of Arts

in

Physics

Stony Brook University

August 2008

Stony Brook University

The Graduate School

Simon Karl Moser

We, the thesis committee for the above candidate for the Master of Arts degree, hereby recommend acceptance of this thesis.

Chris J. Jacobsen – Thesis Advisor
Professor, Department of Physics and Astronomy

Konstantin K. Likharev – Chairperson of Defense
Professor, Department of Physics and Astronomy

Robert E. Shrock
Professor, C. N. Yang Institute for Theoretical Physics

This thesis is accepted by the Graduate School.

Lawrence Martin
Dean of the Graduate School

Abstract of the Thesis

A New Combined Detection System for STXM and the Applicability of (CdSe)ZnS Nanocrystals to SLXM

by

Simon Karl Moser

Master of Arts

in

Physics

Stony Brook University

2008

The topic of this work comprises two major tasks: first, a new combined detection system was developed and characterized for the scanning transmission x-ray microscopes at beam line X1A at the National Synchrotron Light Source at Brookhaven National Laboratory. A relatively simple and inexpensive detector with good performance that combines an x-ray detector through a scintillator/lightpipe/photomultiplier setup with a luminescence detector through a microscope objective/photomultiplier setup has been developed. The x-ray detector has been fully characterized and proposed as an alternative to the preexisting silicon detector now in use. Besides this development, this project focused on choosing the best scintillator for the energies the microscopes work at and the formation of a uniform thin film of these scintillators. This project was partly done as research support in collaboration with Benjamin Hornberger, Xradia Corporation, California. Secondly, the question whether quantum dot nanocrystals, such as (CdSe)ZnS can serve as useful cell labels in low energy scanning transmission x-ray microscopy, was investigated. In contrast to luminescence microscopy with UV excitation of the nanocrystals which has been in use for the last 20 years, where pair production primarily takes place via direct photoelectric absorption, leading to high quantum yields, x-ray scintillators obtain their fluorescence energy mainly through secondary and higher order electron-electron and photon-electron processes. These processes require large volumes in order to distribute as much x-ray energy as possible throughout the scintillator. Scintillators such as ZnS:Cu with an average crystal size of 5 μm have a large volume relative to (CdSe)ZnS quantum dots where the average size distribution is on the order of 5 nm, making the detection of a fluorescence signal from these particles challenging. In addition to the aforementioned topics, the experimental end station of the X1A beam line at the NSLS is presented. Further, initial unsuccessful approaches are shown as well as successful results of a UV/VIS/NIR spectrometer that is proposed to be included into STXM as a detector capable of energy resolved photoluminescence measurements.

To my home.

Contents

List of Figures

List of Tables

Acknowledgements

Of course, this work as main part of the exchange program I took part in would not have been possible without the help of so many people, regardless if it was of an emotional, a professional or a financial kind. Therefore I'd like to say thank you. First of all to my thesis advisor Chris Jacobsen who immediately adopted me in his research group and supported me strongly procuring educational, scientific and financial freedom. Holger Fleckenstein spent so many hours in helping me out with the whole STXM concept, with our network infrastructure and many many unnamed issues more. He integrated me beyond work as a friend. Sue Wirick trusted me in operating the beam line X1A and the STXM after no time, totally integrated me into the research community at the NSLS and supported me in thousand different other ways. She is the actual heart of beam line X1A (see 2.2). Mark Jablonski, Jeffrey Slechta and Walter Schmeling trained me in operating all the machines in the machine shop without loosing patience and always helped out in situations that I couldn't handle alone. Charles Pancake and Eugene Shafto from the electronics shop spent hours to debug my electronic circuits. Many thanks also to John Noe who must found himself in a constant state of being begged for experimental devices. Xiaowei Teng from the Center of Functional Nanomaterials, Brookhaven was very helpful concerning quantum dot sample preparation. Furthermore I would like to thank the whole rest of the x-ray group as well as my roommate Uvo Hölscher, Steffi Forster, my parents, my grannies and all the many others for all kinds of support. The German Academic Exchange Service (DAAD), the Department of Physics and Astronomy Stony Brook and the National Institute of Health (NIH) under contract No. 5R21EB006134-02 financed this exchange program for me.

Chapter 1

Introduction

Scanning transmission x-ray microscopy (STXM) is an imaging method that measures the x-ray absorption of a thin sample by scanning it through a focal spot. Soft x rays between the energy range 280 to 600 eV, encompass the carbon, nitrogen and oxygen K absorption edges where organic materials show good absorption contrast relative to water. The STXM is a useful tool to analyze all kinds of samples which can be studied at about 55 nm Rayleigh resolution.

Scanning luminescence x-ray microscopy (SLXM) is in principle similar to STXM, but records stimulated visible light emission from phosphors and dyes within the sample [4]. It is possible to match structure to biological function using special dyes which selectively bind to specific molecules associated with certain biochemical activities. Unfortunately, those dyes are typically developed for ultraviolet (UV) or visible (VIS) light excitation and emit at slightly longer visible wavelengths or the near infrared (NIR). While organic dye molecules usually suffer from radiation damage when using x rays, the more popular gold labels tend to require heavy cell processing which falsifies the natural environment of the examined specimen. Anyway, gold labels work as scattering centers rather than luminescence centers and therefore the signal is always recorded against x-ray background. To diminish background, annular dark field imaging can be used to view the gold particles if the particle size is comparable to the probe size or larger. Anyway, this is in contrast to luminescent centers where the background is in principle dark.

A very promising biological labeling material developed during the last twenty years and successfully applied to UV/VIS excitation based luminescence are so called quantum dot nanocrystals (qdots). These highly ordered semiconductor compounds of about 5 nm in diameter offer highly flexible surfaces and therefore can be bound to many different kinds of organic features using antigen-antibody key-lock principles. Being able to control the size of the qdots allows one to control the emission wavelength for photoluminescence continuously from about 400 to 2000 nm [5], and to be able to guarantee that no other material except the dye itself emits at its characteristic wavelength. Hence, different sizes of quantum dots emitting different colors can be attached to different compounds of an organic sample and studied via one single excitation wavelength, allowing co-localization studies (see figure 1.1). Additionally, the radiation damage would be low in comparison to most organic dyes.

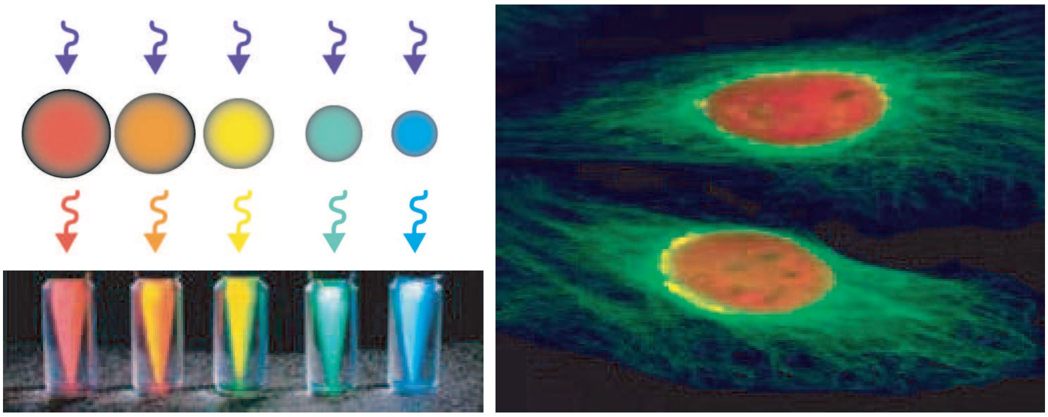

Figure 1.1: **Labeling with Quantum Dots.** (Images taken from Invitrogen Corp., General Information Brochure [6].)
Quantum dots with different diameters can be excited with ultraviolet light of one single wavelength (left). The diameter tunes the band gap and therefore the wavelength of luminescent light. Hence, quantum dots with different diameters emit light in different colors.
Co-localization studies on Hela cells using UV excited quantum dot nanocrystals (right). Tubulin fibers are marked in green, golgi bodies in yellow and nuclei in red. Similar images with a much better resolution might be achieved using soft x rays.

In 2006, Jan Steinbrener [7] worked on the question "are quantum dot labels a feasible means to further improve scanning luminescence x-ray microscopy in the soft x-ray energy range?" At this time, protocols for cell labeling with qdots were developed successfully: Steinbrener stated, "Once the correct protocol is figured out, the preparation of quantum dot stained cells for x-ray microscopy is easy and can be done within two days." Nevertheless, the actual applicability of quantum dots in SLXM, especially the well studied and characterized (CdSe)ZnS model systems which have been used as a standard in visible light microscopy to label cells for years, could not be determined. An avalanche photodiode was used to detect the luminescence signal of cells prepared with nano crystal labels, but concentrations were so low, the detector signal never got above its dark noise level. Hence, a new approach of characterizing the feasibility of quantum dots excitation in the soft x-ray energy range would be to test them using a well designed and characterized detector system in combination with known concentrations. In other words, knowledge of the quantum yield within the soft x-ray excitation energy range as well as the knowledge about the actual emission characteristics would be studied.

In Steinbrener's thesis he states, "Although it seems that, on the one hand, quantum dots have a low quantum yield for x-ray excitation, which is a disadvantage for SLXM, and that, on the other hand, their bleaching properties are good enough to qualify them as a SLXM label,..." [7] it is worth considering them once more for further investigation. With Steinbrener's research, it was not possible to record fluorescence image, using matching filters (*i.e.* those for the specified emission wavelength of the quantum dots). Assuming that qdots actually luminesce at soft x-ray excitation, this could mean two things: first, the fluorescence is actually not emitted from the quantum dots themselves, but rather from their bio conjugating hull or from cell proteins (autofluorescence); secondly, the quantum dots emitted light of a different wavelength when excited with x rays as compared to the emitted light when qdots are excited with visible light.

Several improvements were proposed in 2006 by Steinbrener. The assumption that the quantum dots do not emit on their specified wavelength when they are excited with soft x rays leads necessarily to an experimental approach of doing spectroscopy on the nanocrystals considering emission wavelengths in the UV/VIS/NIR frequency bands. These experiments can be done throughout the whole soft x-ray excitation energy range at different fluxes by use of a spectrometer. The spectra then would directly identify the nanocrystals even in the presence of other materials underlying fluorescence effects.

Approaching the topic, the development of a x-ray detector basing on a scintillator/lightpipe/photomultiplier combination was started in collaboration with Benjamin Hornberger, Xradia Corporation, California, who was developing a similar detector for commercial use at the same time based on a concept presented by Fakra *et al.* [8]. In order to be able to use this detector for luminescence detection it was built so that it is simple to change between the light pipe and a microscope objective. This detector is now installed in the X1A2 microscopy located at the NSLS.

Analysis of the quantum dots using this detector setup was not successful, so a spectrometer was purchased to try and detect the qdots as suggested by Steinbrener [7]. Results using the spectrometer show that, due to their small size, (CdSe)ZnS quantum dots are not a feasible biological label for SLXM.

Chapter 2

The Scanning Transmission X-ray Microscope at the National Synchrotron Light Source

2.1 The National Synchrotron Light Source at Brookhaven National Laboratory

2.1.1 Definition and History

In 1978, the U.S. Department of Energy's Office of Basic Energy Sciences budgeted funding for a "second generation" electron synchrotron at the Brookhaven National Laboratory, Long Island. The new synchrotron facility was called the National Synchrotron Light Source (NSLS) [9] (see figure 2.1). The vacuum ultraviolet (VUV) ring began operations in the late 1982, while the x-ray ring started in 1984.

The accelerator takes stationary charged electrons and drives them to velocities near the speed of light. Being forced by magnets to travel around a circular storage ring, the electrons tangentially emit electromagnetic radiation and, consequently, lose energy. This energy is emitted in the form of light and is known as synchrotron radiation.

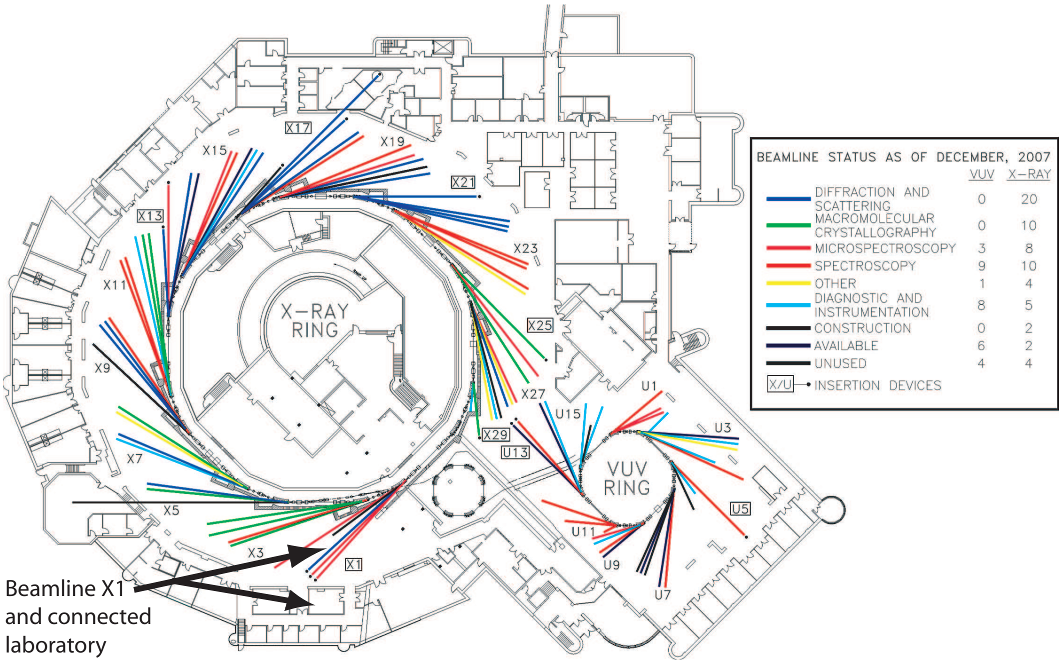

Beamline X1
and connected
laboratory

Figure 2.1: **The National Synchrotron Light Source at the Brookhaven National Laboratory.** Beam line X1A and adjacent labs are highlighted. (Image taken from the NSLS web page [9] and altered.)

Through the implementation of global orbit feedback systems, the orbit was stabilized and local orbit feedback provides enhanced stability for the insertion device beam lines. In Spring 1993, a current of 500 mA was stored at 2.5 GeV kinetic energy. Also, the vertical emittance was reduced by a factor of six down to below 2 Å, corresponding to a horizontal-vertical coupling of 0.002. In 1996, the operating current was increased to 350 mA at 2.8 GeV. In the period between 1999 and 2000, the x-ray ring had alternating operations between high emittance lattice at 2.8 GeV and low emittance lattice at 2.58 GeV. In August 2000, the ring started regular operations with low emittance lattice at 300 mA, 2.8 GeV. The increase of energy together with the reduction of vertical emittance yielded an order of magnitude increase in brightness.

Nowadays during normal operation, the ring is filled twice per day. The normal fill pattern is a train of 25 consecutive equal current bunches filled out of a possible 30 buckets. This fill pattern provides freedom from ion trapping and coupled bunch instabilities. Injection of the ring has been improved such that normal refill from zero current typically takes less than 10 min. Electrons are injected into the NSLS storage rings from a 750 MeV booster synchrotron fed by a 120 MeV linear accelerator (linac).

The electrons are first produced in a 100 KeV triode electron gun. After acceleration in the linac, the beam is injected into the booster on seven successive turns. After injection, the magnetic field of the booster increases to maintain a constant orbit radius as the radio frequency accelerating cavity boosts the electron energy to 750 MeV. At maximum energy, a kicker magnet is pulsed to send the beam past a septum and into the x-ray or VUV storage ring. In the future, the injection cycle will be decreased to 0.5 s and the maximum energy will be raised to 800 MeV for improved storage ring injection.

To increase the performance of state of the art experiments, a new synchrotron light source, located next to the original one, NSLS-II, is proposed to provide higher average brightness and higher flux. The new storage ring that is expected to start operation in 2015 will be able to produce x rays up to 10000 times brighter than those at the NSLS today.

2.1.2 The Undulator at X1

For imaging samples in scanning transmission microscopy as well as in scanning photoemission microscopy and soft x-ray diffraction, spatial and temporal coherence are very important [10]. Undulators are particularly suitable radiation sources since it is known that coherent intensity by collimation from an incoherent source is directly proportional to the source brightness [11]. When it comes to imaging in the soft x-ray regime from about 10-50 Å, a soft x-ray undulator (SXU) in combination with a monochromator and a zone plate can provide high spatial coherence at a high flux with spectral resolving power of about $\frac{\lambda}{\delta\lambda} \leq 200$ to 800. The X1 undulator is a permanent magnet/steel hybrid device, based on the so called Halbach scheme. It operates with 35 periods of 8 cm length each at a maximum power of 800 W. Its gap can be adjusted from 32 to 98 mm. This basically means a variation of K, the magnetic deflection parameter, from 2.47 to about 0.17 which itself determines the fundamental wavelength (fixed current for 43.5 mm $\sim K = 1.5$). Thus, fundamental wavelengths from 17 to 70 Å are possible. Usually, energies around the carbon edge are studied at a gap around 36 mm whereas energies around the nitrogen edge at 42 mm (see figure 2.2).

Going more into detail, the common rules for determination of the undulator radiation characterization are

$$\lambda \approx \frac{\lambda_0}{2\gamma^2}(1+\frac{K^2}{2}) \tag{2.1}$$

$$K = 0.934 B_{\max}\,[T]\,\lambda_0\,[cm] = \frac{e}{2\pi mc} B_0 \lambda_0 \tag{2.2}$$

and

$$B_0\,[T] \approx \frac{0.534}{\sinh\left(\frac{\pi \mathrm{GAP}[cm]}{\lambda_0\,[cm]}\right)} \tag{2.3}$$

where λ_0 is the undulator's magnetic period, B the magnetic field and $\gamma = 1/\sqrt{1-v^2/c^2}$ is the Lorentz factor of the electrons. Since the intrinsic divergence of undulator radiation $\sigma_{R'} = \sqrt{\frac{\lambda}{L}} \approx 35$ μrad for $\lambda = 3.6$ nm is much smaller than the electron beam divergence, the source phase space of the undulator's radiation is determined almost entirely by the electron beam.

Calculations especially for the soft x-ray undulator (SXU) X1 were made by Jacobsen *et al.* [12] and can be accessed via an IDL program called X1_und.

For the m^{th} harmonic, N periods of length λ_0 and a magnetic field parameter as introduced in equation 2.2, undulator radiation with wavelengths within the natural line width $\Delta\lambda_m/\lambda_m = 1/2mN$ has an approximate angular spread of

$$\sigma_{R'} = \sqrt{\frac{\lambda_m}{N\lambda_0}} = \frac{1}{\gamma}\sqrt{\frac{1+\frac{K^2}{2}}{2mN}} \tag{2.4}$$

where the electron beam is assumed to be an infinitely thin thread of current. Taking into account the effects of electron beam emittance by treating an undulator as an extended source of radiation, Gauss distribution in space and angle with standard deviation $\sigma_{R'}$ can be assumed.

Figure 2.2 shows the X1 undulator output for continuous gap sizes as well as for two typical gap sizes as used at X1A. For a gap size of 36 mm, the undulator fundamental covers the region near the carbon K-absorption edge while the second harmonic provides good intensity near the oxygen K-edge. A gap of 42 mm is optimized for the region of the nitrogen K- and iron L-absorption edges. The presence of the second harmonic peaks on-axis is due to the finite electron beam divergence in the low-L straight section where the undulator is located. Phenomenologically, the first harmonic peak results from coherent interference of radiation resulting from the electrons oscillating perpendicular to the magnetic field and the electron beam, respectively. In contrast, the second harmonic results from the electron speed modulation along the electron beam path that leads to forward radiation emission due to Lorentz contraction. Higher order harmonics result from interference of these two effects.

2.1.3 The Beam Line X1A

X1 supplies three different beam lines, X1A1, X1A2 and X1B which is run by another group. The undulator itself is terminated by NSLS standard components as an isolation valve followed by a water cooled mask, a fast acting valve, a safety shutter and a 15 mm water cooled aperture that restricts the angular spread of the beam to 0.6 mrad high and 1.6 mrad wide [13–15]. The water cooling is necessary whereever there is high power in the beam on optical elements which could be damaged, or lose position and shape if they were not cooled.

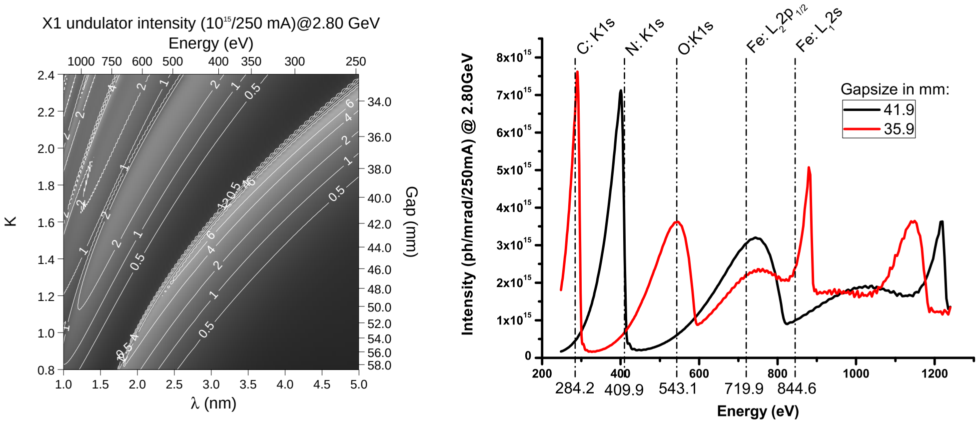

Figure 2.2: **The X1 Undulator Output.** (Data retrieved by the IDL program X1_und [12].)
Calculated undulator output for continuous gap sizes (left).
Calculated undulator output for two typical gap sizes as used at X1A and according binding energies of some important elements (right).

A beam position monitor which was meant to maintain the direction of the x-ray beam via a beam stabilizing feed back system follows. Since beam position can nowadays be fully controlled by a digital feedback system, the beam position monitors are turned off. Beam is further restricted via special beam defining apertures. Four motor driven water cooled inclined jaws collimate the beam. The coupling of the beam into the beam line can be seen in figure 2.3.

The safety shutter is closed while the beam line does not operate. During operation, to stop possible *bremsstrahlung* radiation which result in hard x rays and gamma rays, lead shielding is used. The front end is shielded by a leaded concrete wall. A beam stop catches undeflected *bremsstrahlung* after the beam being deflected into the beam line by the water cooled primary mirror. The highest dose level near the beam line is about 1.0 mRem/h behind the beam stop, at the experimental stations about 100 times lower.

About 12.95 m from the source, the beam splicing to X1A and X1B is done by a water-cooled plane scraping mirror (nickel coated) of 40 mrad grazing angle which directs 35 % of the beam towards X1A and 65 % to X1B. Beyond, it absorbs radiation above 2 keV. A rough schematic of X1A is presented in 2.4.

After the heat load is taken out by a water cooled Cu mask, X1A splits into X1A1 and X1A2, the end stations for each beam line being a room-temperature

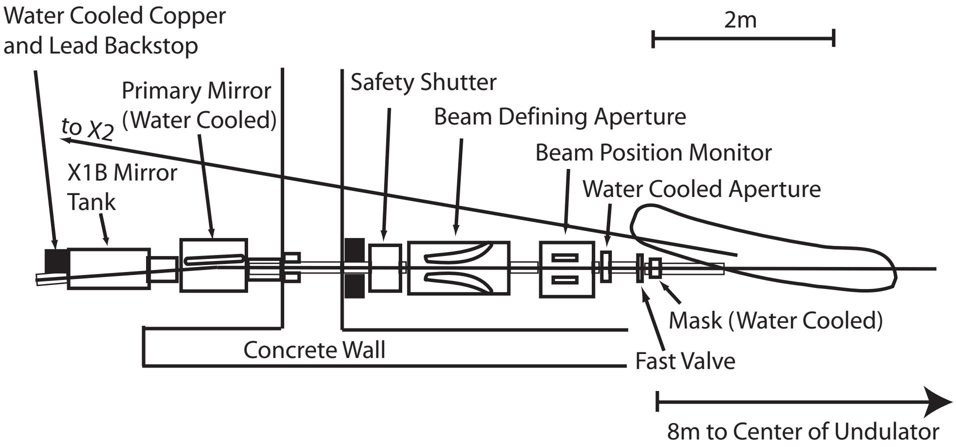

Figure 2.3: **Schematic Diagram of the Principal Components of the X1 Beam Line Front End.** (Image taken from Rarback *et al.* [16] and altered.)

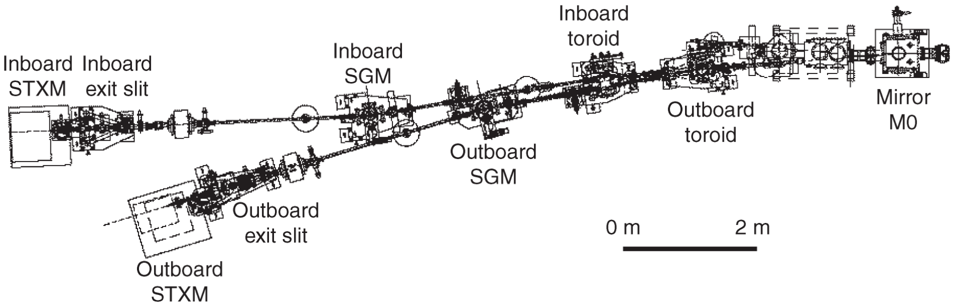

Figure 2.4: **Schematic of the Beam Line X1A.** The x-ray beam is split into three parts by two toroids, one to supply a STXM at X1A1, one to supply a STXM at X1A2 and one to supply X1B which is operated by another group. For each part, a spherical grating mirror (SGM) in combination with entrance and exit slits serves as a monochromator. (Image taken from Winn *et al.* [17] and altered.)

scanning transmission x-ray microscope (STXM) [17]. The splitting of the beam between X1A1 and X1A2 is approximately 50 %, done by two gold coated toroidal mirrors which focus in both the horizontal and vertical directions. The first toroidal mirror focuses the beam horizontally for X1A1 onto a water cooled entrance slit with a magnification of 0.12 and vertically onto the exit slit of the X1A1 spherical grating monochromator (X1A1 SGM) with a magnification of 0.48. This toroid has a $\sim$ 50 mrad grazing angle, a major radius of 70.6 m and a minor radius of 0.509 m and is located about 16.3 m from the source. The undeflected part of the beam hits a second similar toroid (same focusing parameters on X1A2). Both mirrors are made of single-crystal silicon blanks which are gold coated over the footprint of the beam. Both toroids are water cooled.

Upstream of the experimental end station is a set of already mentioned discrete water cooled entrance fixed, slits ranging in size from 10, 25, 40, 70, 120, 200 μm and 1 mm. They are made in a single sheet of 0.37 mm thick nickel-coated beryllium-copper. Aluminum photodiodes downstream of the entrance slits help to monitor the beam intensity at these points. Before the beam enters the monochromator chamber, a grating mask restricts the height and the width of the beam on the gratings. This mask is followed by a horizontally dispersing spherical grating of $\sim$ 3.5° grazing angle (X1A1: nickel coated, X1A2: gold coated) with a stepper motor driven sine arm mechanism that is linear in the photon energy. For accurate and reproducible adjustment of the radiation energy, an encoder is provided. Since the undulator beam does not have sufficient spatial coherence to be used directly for diffraction limited imaging, the monochromator serves to gain high spatially coherent flux with moderate temporal coherence ($\sim$ 200 to 1600 waves) [10].

Further downstream, a set of slits to measure and define the vertical extent of the beam at the monochromator exit slit is provided. These fixed vertical exit slits with slit sizes of 10, 25, 40, 70, 120, 200 μm and 1 mm come together with a continuously variable size horizontal exit slit. The exit slits are followed by higher order sorting mirrors.

The X1A1 end station microscope runs at atmosphere with helium flowing around the sample area. The X1A2 microscope runs in a helium environment at 620 torr. To separate the beamline ultrahigh vacuum environment from the microscopes, a silicon nitride exit window is used on X1A1 and a silicon window is used on X1A2 [10]. The windows are 300×300 μm^2 and 120 nm thick. An aluminium vacuum photodiode is located just downstream of the horizontal exit slits on both beamlines, acts as a shutter and, when closed, as a detector to measure the beam current. It is used to align both the fixed entrance and exit slits for maximal flux. To be able to find and align the beam properly, *e.g.* after a shut down of the NSLS, phosphor pads are provided at different stages of the beam line. In addition, X1A1 has a photodiode consisting of four sections to be able to monitor the beam position.

Although the concept for the X1A2 beam line is in principle the same as for X1A1, there are slight differences between them mainly affecting the optimization of the two different branches for different energy ranges. As stated in Eberhardt *et al.* [18], the K absorption edges of elements like C, N, O, and F as well as the L edges of the first row transition metals all fall within a photon energy range of 250 eV to 1 keV (lifetime widths are usually shorter than 100 meV). Nevertheless, the study of different elements requires different conditions.

2.2 The Scanning Transmission X-ray Microscope STXM

The experimental heart of X1A that is well established nowadays and well known worldwide among scientific institutions as in the field of environmental science or geology as well as among global players as ExxonMobil Research and Engineering Co., is of course not the infrastructure of the beam line in itself but the scanning transmission x-ray microscope as multi functional soft x-ray imaging end station. The microscope is used to not only image samples but to map elements and obtain chemical information using X-ray Absorption Near Edge Structure (XANES) spectroscopy.

In any microscope, the resolution can be no better than the limit set by the objective lens. In a scanning transmission x-ray microscope (STXM), a Fresnel zone plate serves as the objective lens, focusing a coherent beam down to a small spot through which the specimen is scanned. In the X1A STXMs, the focused flux is typically about 10^6 photons per second, and the spot size has a radius (Rayleigh resolution) of about 40 nm. Here, zone plates are mounted just downstream of the exit windows.

As illustrated in figure 2.5, a zone plate with N zones of radius $D = 4Ndr_N$ and outer most zone width dr_N consists of alternate transparent and opaque rings with radii given by

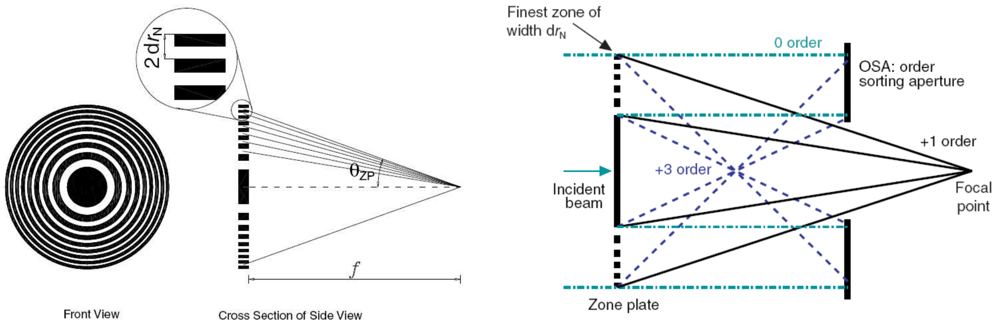

Figure 2.5: **The Fresnel Zone Plate Schematic.** (Images taken from Hornberger [19].)
Schematics illustrating front and side view of a Fresnel zone plate as well as the crucial parameters "outermost zone width", "numerical aperture" and "focal spot" (left).
The combination of a central stop on the zone plate and an order sorting aperture (OSA) helps to absorb all other orders then the first (right).

$$r_n^2 = nf\lambda + n^2\lambda^2/4 \tag{2.5}$$

where n is the zone number, λ is the wavelength of the incident light and $f = Ddr_N/\lambda$ is the first-order focal length [20]. Phase shifting instead of completely opaque rings are used to increase the efficiency of the zone plate [21]. The Rayleigh resolution is given by

$$\delta_t = 1.22 \cdot dr_N \tag{2.6}$$

and the numerical aperture by

$$NA = \sin\Theta_{ZP} = \frac{\lambda}{2dr_N} \tag{2.7}$$

In order to absorb all other orders then the first, a combination of a central stop and an order sorting aperture (OSA) is used as shown in the right part of figure 2.5 [19].

Down stream of the zone plate and the OSA, a sample mount follows. It is attached to a x-y piezo motor stage sitting on x-y-z stepper motor stages, where

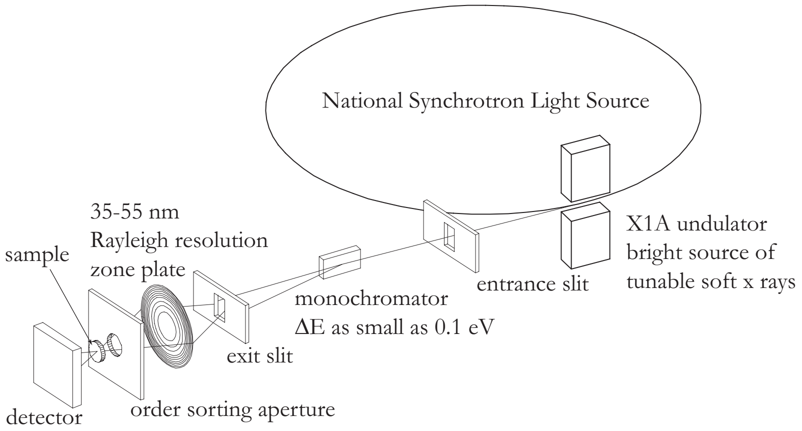

Figure 2.6: **Sketch of the STXM Working Principle.** The x-ray beam coming from the undulator is prepared by a monochromator, focused onto a sample by a Fresnel zone plate and collected by a detector. The sample can be scanned through the x-ray focus; in x- and y-direction to scan the sample and in z-direction (beam direction) to adjust the focus. (Image taken from Wang [22].)

x stands for the horizontal, y for the vertical and z for the beam direction. During operation, the sample mount holding a sample is brought into x-ray focus and interesting regions are scanned according to the operator's demand. The transmitted x-ray signal is captured by the detector that is placed further downstream. Practically, one can obtain 80×80 μm^2 scans of a resolution beyond the zone plate resolution limit with the piezo stage and much bigger scans of about 1 μm resolution with the stepper stages [23]. Stage drift is corrected by a commercially available interferometer feed back system with 2 nm spatial resolution, well below the spatial resolution of any of the zone plates used.

A very elaborate microscope control environment combined with an IDL user interface called "sm_gui" allows the user to do microscopy on an almost completely automatic basis. Some common terms that will be used in the following shall be explained more precisely.

- Stepper Scan: a transmission image that is obtained by scanning the sample in the x-ray focus using the stepper stages.
- Piezo Scan: an transmission image that is obtained by scanning the sample in the x-ray focus using the piezo stages.

- Point Spectrum: a transmission spectrum that is obtained by keeping the sample at one point in x-ray focus and varying the incident x-ray energy.

- STACK: a series of stepper or piezo scans concentrating on the same sample region obtained at different x-ray energies. One can align the STACK data set in x and y after data collection to obtain absorption spectra for each pixel of the scanning range and thus a chemical mapping of the scanned area is possible. By choosing regions of equal transmission behavior one can average over their signal and therefore further improve statistics for such spectra. For a single point spectrum this is often accomplished by increasing the exposure time or averaging multiple point spectral scans [24].

Of course, the x-ray detector can be replaced by a visible light detector to measure visible light fluorescence as will be discussed later in this work.

Chapter 3

A Combined Detector System for STXM

3.1 The Photomultiplier Tube PMT

3.1.1 Working Principle

Photomultiplier tubes (PMT) in general consist of an evacuated glass tube with an input window in the front to guide light to a photocathode, where electrons are excited [25]. In the case of sufficiently high photon energy, photoelectrons are emitted into the vacuum by the external photoelectric effect and accelerated to the first dynode. Electrodes help to focus the electrons so that a maximum of released electrons is able to hit the dynode where they are multiplied by means of secondary electron emission. This secondary emission is repeated throughout a whole set of successive dynodes until the generated electron avalanche is collected by the anode. The working principle of a PMT is shown in figure 3.1.

Of course, photoelectrons at the photocathode can only be released in the case where the incident photon energy exceeds the work function of the cathode material which is basically the energy difference between Fermi level and vacuum level.

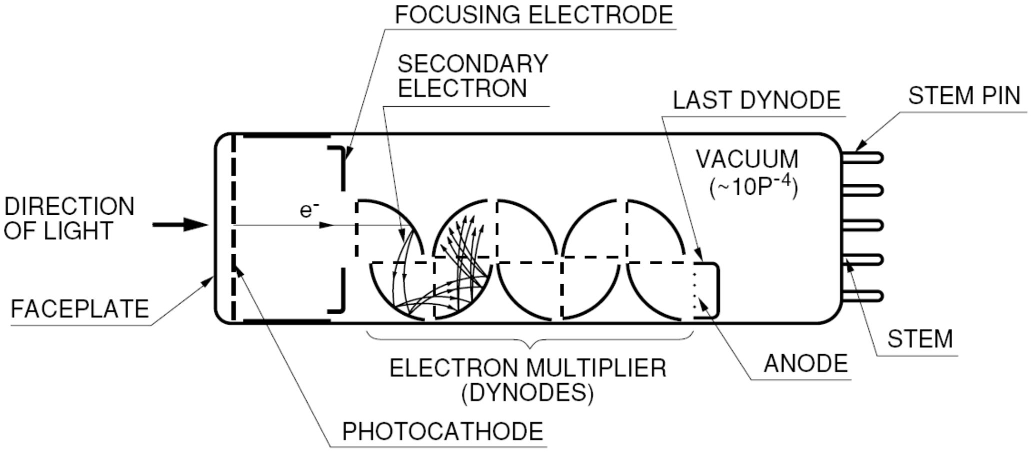

Figure 3.1: **Construction of a Photomultiplier Tube.** Photoelectrons generated by incident photons on a photo cathode are accelerated and avalanched over a set of dynodes until they generate a pulse at the anode. (Image taken from Hamamatsu, Photomultiplier Tubes - Basics and Applications [25].)

3.1.2 General Properties

Photomultiplier tubes offer the advantage of very weak light detection with typically very linear charge amplifications to about $10^7 - 10^{10}$ electrons [25–27]. In order to free an electron, the energy of an incoming photon has to overwhelm the potential barrier (work function) of the photocathode which is typically $1.5 - 2$ eV and therefore causes a long wavelength cutoff. The maximum response wavelength and the long wavelength cutoff are determined by the combination of alkali metals used for the photocathode and its fabrication process. Hence, most photocathodes are made of compound semiconductors which consist of alkali metals with a low work function. A short wavelength limit on the other hand is defined by the window material which often times absorbs light within the UV-region. This cutoff of the glass is situated typically around 350 nm (see figure 3.3).

In semiconductor photocathodes with a bandgap E_{gap}, electrons that are excited from the valence to the conduction band suffer phonon decay to the bottom of the conduction band in timescales of about a picosecond from where it takes about another 100 ps to recombine. Therefore, electron escape happens only in the case where the electron reaches the surface of the cathode before phonon decay is possible. Photoemission time then is on the order of 0.1 ns.

Concerning the time characteristics, one can expect very fast time response which is determined mainly by the transit time. It depends as well on the dynode type as on the supply voltage ($t \propto 1/\sqrt{V}$) and is usually situated in the range of 20 to 50 ns from cathode to anode. The electron pulse duration is typically also on the order of nanoseconds and in principle reflects fluctuations of the transit time of around 300 ps for each photoelectron within one avalanche. Timing properties are highly dependant on construction characteristics such as the shape of the photocathode or electron trajectories.

The quantum efficiency $\eta(\nu)$ of a PMT, which is the ratio of output electrons to incident photons can be calculated as a statistical process:

$$\eta(\nu) = \frac{\text{number of photoelectrons emitted}}{\text{number of incident photons}} = (1-R)\frac{P_\nu}{k}\frac{1}{1+\frac{1}{kL}}P_s \qquad (3.1)$$

R and k are the reflection and full absorption coefficient of photons of light frequency ν determined by the cathode material. The probability P_ν, that light absorption may excite electrons to a level greater than the vacuum level, is dependent on the cathode material. L on the other hand is the mean escape length of excited electrons and depends on the crystal structure; the more crystalline the material, the longer L will be. The probability that electrons reaching the photocathode surface may be released into the vacuum, P_s, depends on the electron affinity. Usually the quantum efficiency η is on the order of 20 to 30 %.

Nevertheless, the conversion efficiency (photocathode sensitivity) varies with the incident light wavelength. This relationship between the photocathode and the incident light wavelength is referred to as spectral response characteristics which are expressed in terms of radiant sensitivity S_k (photoelectric current generated by the photocathode I_k divided by the incident radiant flux L_p at a given wavelength, expressed in units of amperes per watts) and quantum efficiency η (see figure 3.3). Another relation for the quantum efficiency is:

$$\eta = \frac{hc}{\lambda e}S_k = \frac{hc}{\lambda e}\frac{I_k}{L_p} \qquad (3.2)$$

The amplification effect of the photoelectrons to generate a whole avalanche takes place via electron multiplication at a series of dynodes with bandgaps on the order of 2 to 3 eV. A dynode voltage of about 100 V therefore corresponds to a theoretical amplification of about 30 excited electrons per incoming electron. The collection efficiency of the first dynode is usually around 60 to 90 %. The multiplication factor δ for a single dynode is defined as

$$\delta = \frac{\text{number of secondary electrons emitted}}{\text{number of primary incident electrons}} \propto E^k \tag{3.3}$$

where E is the interstage voltage of dynodes and k which lies between 0.7 and 0.8 depends on the dynode material. δ can be increased by use of negative electron affinity materials in which an electron has still enough energy to flee even if it already decayed to the conduction band surface (bent band). The overall gain μ of a PMT with n equal dynodes and an equally distributed voltage divider of voltage V is

$$\mu = \alpha\delta^n = \alpha(aE^k)^n = \alpha a^n(\frac{V}{n+1})^{kn} \tag{3.4}$$

where α is the fraction of all photoelectrons collected by the multiplier structure. Typical values are $\delta \sim 5$, $\alpha \sim 1$ and $n \sim 10 - 19$ but $\delta = \delta(V)$ is a function of V. Hence, a normal overall gain would be about V^6 to V^9.

Noise is present without light input (dark current) and is also generated by the input of the signal from light. Usually, photocathode thermionic emission and shot noise resulting from the signal current are the governing factors. A typical noisy signal with its characterizing parameters can be seen in figure 3.2.

In most cases where $I_p \gg I_d$, the dark current can be neglected and the signal to noise ratio will be

$$S/N \approx \frac{I_p}{i_p} \tag{3.5}$$

where I_p is the mean value of the signal component and i_p is the AC component (r.m.s) of the signal. i_p consists of a component associated with the statistical fluctuation of photons and the photoemission process and a component created in the multiplication process. Regarding the statistics in the most simple model, the production of secondary electrons is Poisson distributed with mean

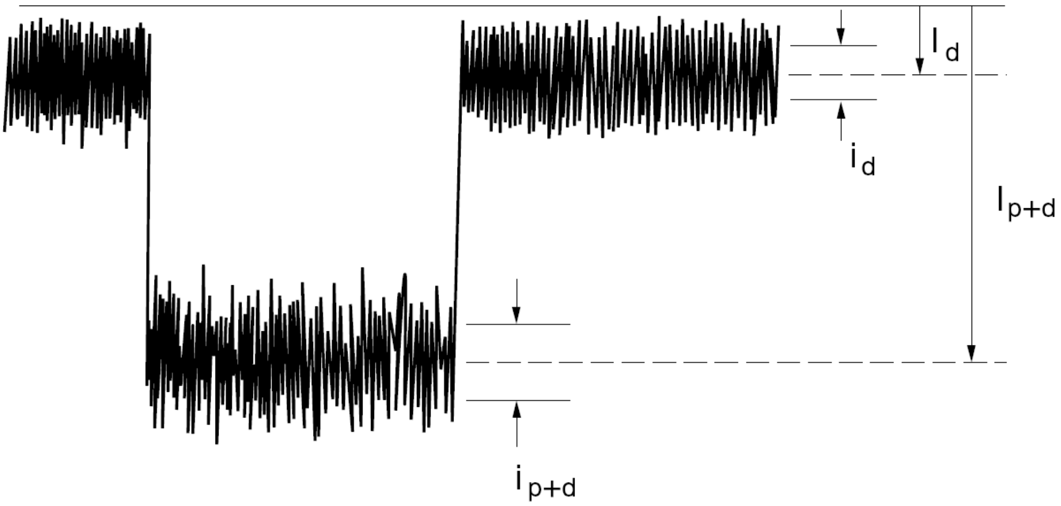

Figure 3.2: **Signal to Noise Ratio of a Photomultiplier Tube.** (Image taken from Hamamatsu, Photomultiplier Tubes - Basics and Applications [25].)
I_p is the mean value of the signal component only, which is obtained by subtracting I_d from I_{p+d}.
I_d is the mean value of noise component.
i_d is the AC component (r.m.s.) of the noise.
I_{p+d} is the mean value of the signal, noise component included.
i_{p+d} is the Ac component (r.m.s) of signal, noise component included.

δ, standard deviation $\sigma = \sqrt{\delta}$ and relative variance $(\frac{\sigma}{\delta})^2 = \frac{1}{\delta}$. To express how much the signal to noise ratio degrades between the in- and output signal, the so called noise figure NF is defined:

$$\mathrm{NF} = \frac{(S/N)^2_{\mathrm{in}}}{(S/N)^2_{\mathrm{out}}} \tag{3.6}$$

$(S/N)_{\mathrm{in}}$ is the signal to noise ratio on the PMT input side and $(S/N)_{\mathrm{out}}$ is the signal to noise ratio on the PMT output side. With a PMT having n dynode stages, the NF from the cascade multiplication process is given by

$$\mathrm{NF} = \frac{1}{\alpha}(1 + 1/\delta + 1/\delta^2 + ... + 1/\delta^n) \sim \frac{1}{\alpha}\frac{\delta}{(\delta - 1)} \tag{3.7}$$

where α is the collection efficiency as introduced in equation 3.4 and $\delta \gg 1$ is the secondary emission ratio at each stage. Adding NF to the AC component i_p, leads to

$$i_p = \mu \left(2eI_kB \ \mathrm{NF}\right)^{1/2} \tag{3.8}$$

B is the bandwidth of the measurement system, I_k the cathode current and e the electron charge. Since I_p can be described in terms of the overall gain $I_p = I_k\alpha\mu$, the following equation can be obtained giving a measure of the actual signal to noise ratio:

$$(S/N) = \frac{I_p}{i_p} \left(\frac{I_k\alpha^3}{2eB}\frac{\delta - 1}{\delta}\right)^{1/2} \tag{3.9}$$

Usually PMTs respond quite linearly with respect to incoming photons within a wide range of incident light levels as well as down at the single photon counting region. Nevertheless, nonlinearities might emerge from very large pulses caused by space charge effects, at very high flux or for deviations of a dynode voltage from the equilibrium value. A very stable high voltage supply at around 1 to 2 kV with a stability within 0.1 %, combined with a voltage divider circuit for distributing an optimum voltage to each dynode compensates for some of the nonlinearities. For stable operation of a PMT, a warm up period of about 30 to 60 min is important.

Furthermore, dark counts may arise from noise due to changes in the ambient temperature. A room temperature of $T = 300$ K corresponds to a mean electron kinetic energy of about $\langle E_{kin} \rangle \sim 25$ meV which can lead to spontaneous emission. In a metal, this spontaneous emission can be on the order of 10^2 to 10^4 emitted electrons per square meter and second, in semiconductors about 10^6 to $10^8/\mathrm{m}^2\mathrm{s}$. Nevertheless, semiconductors have higher noise rates because they are more photosensitive.

A prediction of the spontaneous emission by W. Richardson is described as $T^{5/4}e^{-e\Psi/k_BT}$, where Ψ is the work function of the photocathode, e the electron charge, k_B the Boltzmann constant and T the temperature of the photocathode. This equation is a modification of the Boltzmann factor. The thermic dark current is composed of

$$I_{dark} = \mu \cdot e \cdot \text{thermal emittance} \tag{3.10}$$

Beyond thermic influences, dark current can also emerge from: leakage current; photocurrent produced by scintillation from the glass envelope or electrode supports; field emission current caused by high voltage; ionization current from residual gases as helium; and noise current caused by cosmic rays as well as radiation from radioisotopes contained in the glass envelopes and environmental gamma rays. In general, dark current increases nonlinear with increasing supply voltage.

As can be inferred from equation 3.10, cooling the tube may decrease I_{dark} by a factor of ~ 100 (refer to figure 3.3). As a coolant, one might use dry ice or liquid nitrogen but there are problems associated with cooling the PMT such as water vapor condensation and an increase in photocathode electrical resistance, which leads to less photoelectron collection. Moreover, PMTs are very sensitive to stray magnetic fields, even the earth magnetic field, and therefore have to be shielded by a cylinder of Mu-metal around the outside glass envelope of the PMT. To avoid additional noise, it is the best to keep this shielding at the photocathode potential. In most cases, the sensitivity of the photocathode is nonuniform. 30 to 40 % variations are possible within the whole sensitive surface. Light pipes serve to spread the signal uniformly over the entire sensitive area and therefore average out variations. Especially when voltage is supplied to a PMT, it should be stored in the dark. Otherwise, a persistent increase of the dark current can emerge. When the incident light or the supply voltage is changed in a step function, a PMT tube may not produce an output comparable with the same step function. This effect is referred to as hysteresis and may appear as both over- and under-shoot.

Over time, PMTs change their performance. Here, one talks about "drift-" over short time, and "life-" characteristics over long time span alterations. Both of them primarily depend on variations in the secondary emission ratio and indicate the extent of gain variation with operating time. Performance deteriorations that result from the stress imposed by the high supply voltage, currents and ambient temperatures are usually referred to as "fatigue".

Another common problem with PMTs, especially in pulse detection mode, is elastic scattering of electrons on the first dynode. This causes pulses shortly after the actual event (afterpulses). Also, the ionization of residual gases by electrons will cause more electrons when the resulting ions hit the photocathode, thus causing non-sample pulses to occur. For example, helium penetrating through the evacuated silica bulb causes such effects.

3.1.3 The Photon Counting Head

A Hamamatsu Integrated Photon Counting Head H6180-01 was used in this study [28]. One clear advantage of this integrated system is that it already comprises a PMT, a low level discriminator, a pulse shaper and a high voltage power supply. Hence, its operation only requires a 5 V DC power supply and a pulse counter to capture the 3 V TTL signal. In addition, a magnetic shield is already implemented. The current pulses from this PMT are amplified and then only those pulses higher than a certain threshold are discriminated by the comparator and converted to voltage pulses by the pulse shaper for output. In photon counting heads like ours, the high voltage to be applied to the PMT is already preadjusted by the manufacturer.

According to Hamamatsu, the dynamic range is highly linear up to an incident light power of about 10^{-11} W $\sim$ 20 MHz @ 400 nm. The dark count at room temperature is about 10 counts/s and the pulse pair resolution about 18 ns $\sim$ 55 MHz [28] (see figure 3.3). This makes it especially feasible for STXM, where one is interested in the total number of photons detected within one scan pixel [19]. Time resolution within one scan pixel is therefore not required but the detector should still be capable of measuring high photon flux. This is a problem for most counters because of the dead times in which the detector is not responding to incoming photons. The rapid read out of this detector matches well the data aquisition time of the STXM. The typical dark count behavior due to temperature changes can be seen in figure 3.3 as well as the spectral counting characteristics.

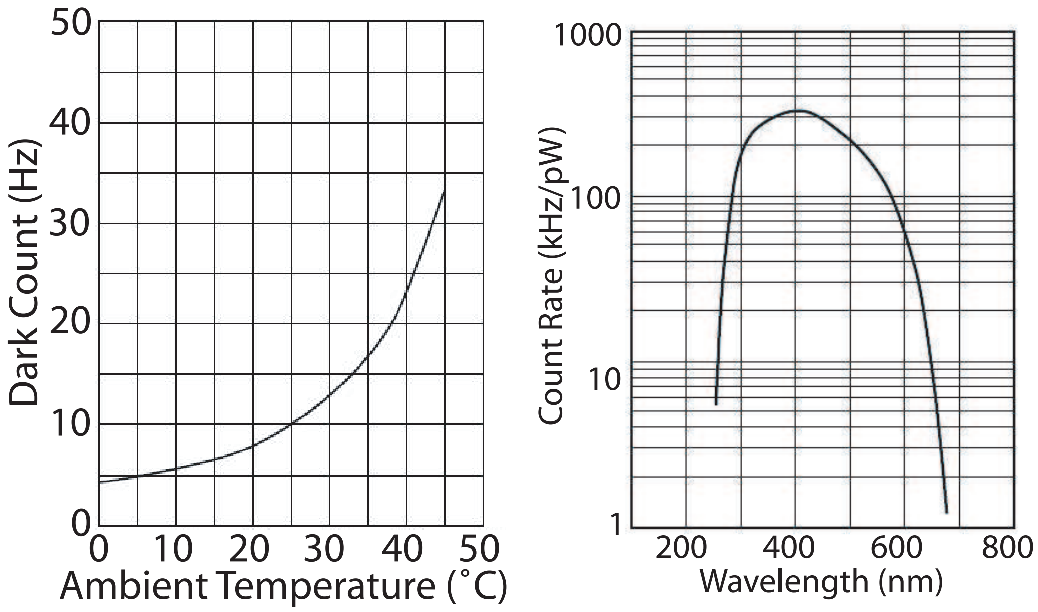

Figure 3.3: **Characteristics of the PMT H6180-01.** (Images taken from the Hamamatsu H6180 data sheet [28].)
Temperature dependance of the PMT dark count. Low temperatures result in better signal to noise ratios (left).
Spectral counting characteristics of the PMT photocathode. At 400 nm, the PMT is the most sensitive (right).

From this figure it indeed makes sense to keep the temperature of the photocathode between 0 and 5 °C to minimize the dark signal.

3.2 The Detector Setup

3.2.1 Mechanical Implementation

A PMT detector was developed for the STXM at the Advanced Light Source (ALS), Berkeley, CA by Fakra *et al.* [8]. Similar PMT detectors are also in use in the STXMs at the Canadian and the Swiss Light Source. According to Fakra *et al.* [8], the ultimate detector for STXM should have a very high efficiency over a wide energy range, single photon counting up to 1 GHz, a high rejection of parasitic visible light (like scattered laser light from the stage stabilizing interferometer in the STXM chamber described in chapter 2.2), fast response, and it should work in both vacuum and atmospheric pressure. One goal of this project was to design and build a PMT detector setup that satisfies the following conditions:

- low cost
- simple design of the mechanical components
- high flexibility and adaptability
- ability to be magnetically shielded
- ability to be cooled
- vacuum (esp. helium) tight
- easy to handle

The first two requirements listed above were achieved by most of the parts required to install the PMT into the microscope being designed and manufactured by the author using inexpensive materials. Taking part in each step of the manufacturing process indeed makes a lot of sense as one easily can intervene and react to any unexpected alteration. Spontaneous improvising is possible at any time without a big time loss. The photon counting head itself is mounted into a stainless steel housing (see figures 3.4, 3.5 and 3.6). For more flexibility and adaptability, the two face sides welded to the stainless steel tube were chosen to be made of 2 3/4" conflate flanges recycled from an old cryo STXM, which allows for connection from both sides of the chamber to any kind of other standard attachment. For example, the back side of the tube is connected to a 2 3/4" flange with four integrated BNC feed-throughs to couple the PMT power supply as well as to couple the PMT TTL signal. On the other side, the tube is terminated by a 2 3/4" flange to 1 1/3" mini flange adapter followed by a vacuum window and a connecting piece for a later connection to an objective slide for a microscope objective. Instead of this connecting piece it is also possible to mount light pipes of different diameters to this adapter. These light pipes will be explained later in 3.2.3. Magnetic shield ability always remains an option. In fact, this problem is solved by choosing an integrated photon counting head where a Mu-metal shield is already included coating the PMT tube directly (see 3.1.3). For the cooling design, a copper tube was integrated coaxial to the stainless steal tube and attached to a solid copper rod that can be screwed into a thread located in the connector side of the front flange. The heat conducting connection between rod and tube was done using a thermo coupling paste. The thread was sealed using a vacuum tight glue to guarantee a good seal to avoid helium leakage. Vacuum seals in this design used o-rings wiped with vacuum grease. Basically the seals are used to keep air in the tube while the STXM chamber is pumped down to a few millitorr and later on to keep the helium used in the STXM out of the PMT. It was described earlier that helium can cause after pulsing on a long term timescale. To prevent water condensation on electronic parts, the PMT itself and the optical path, a bag of silica gel is installed in the back of the tube as desiccant. The final design is illustrated in figure 3.4. This detector is easy to assemble and disassemble.

3.2.2 Signal Feed Throughs

Due to the difficulty of achieving low noise signal transfer, it is worthwhile to mention some basic rules concerning the design of electrical feed-throughs and their impedances [29]. The signal out from the PMT is a 3 V standard TTL pulse with rates that can go up to about 30 MHz. To ideally transmit this signal without any cable interference, standard coaxial cables are used. The impedance here is defined as

$$|Z| = \sqrt{\frac{L}{C}} = \frac{1}{2\pi} \ln \frac{b}{a} \sqrt{\frac{\mu_r \mu_0}{\varepsilon_r \varepsilon_0}} \tag{3.11}$$

where μ_r, μ_0, ε_r and ε_0 are relative permittivity, permittivity of free space, relative and free space permeability and a and b are the core and the shield diameter. Usually, impedances of the coaxial cables are standardized to 100, or in our case 50 Ω. The output impedance of the photon counting head is designed to be approximately 50 Ω, too, in order to handle high speed signals. Problems emerge in the case where one tries to connect different cables of different impedances Z_1 and Z_2 to each other. The simplest version of a feed through would be to tap into the coaxial cable two wires. This will cause an abrupt impedance change and therefore a signal reflection of the order of

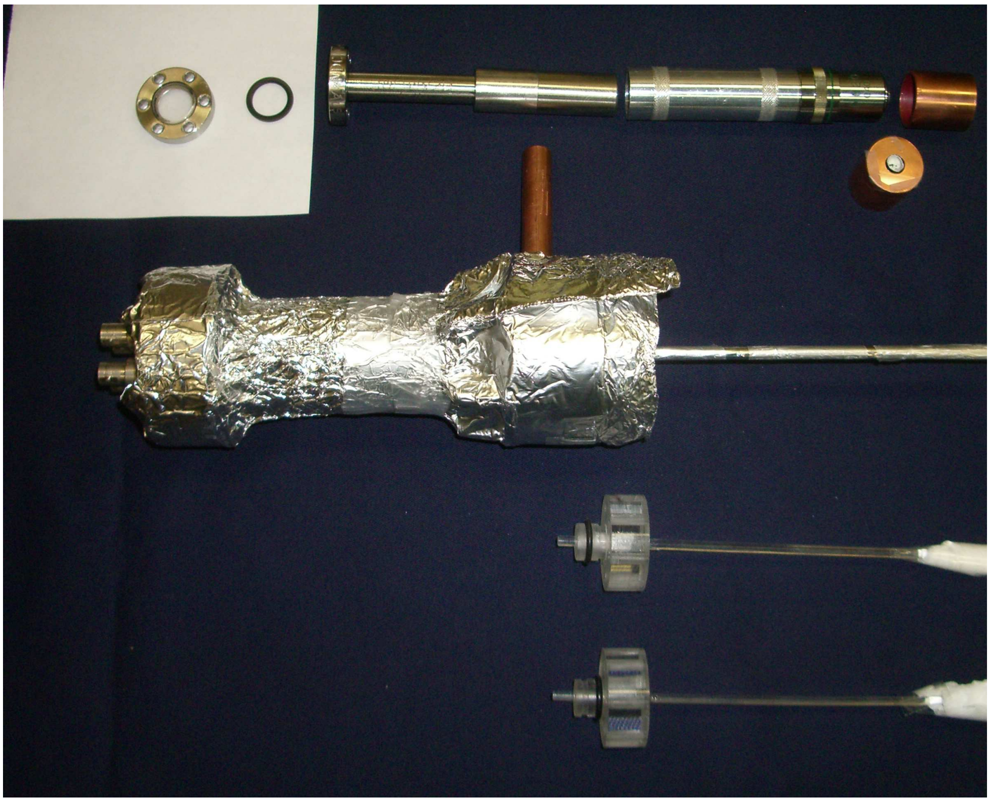

Figure 3.4: **Photograph of the PMT Detector Assembly with all Essential Components.** In the first line, the parts for the microscope objective option can be seen. A vacuum window and an o-ring are followed by the objective telescope and the microscope objective itself. The Objective can be covered by a scintillator carrying copper cap. The second line shows the detector completely assembled in light pipe mode. To reduce dark count, the whole setup is covered in several layers of aluminum. The third and fourth line show two additional light pipes with different diameters.

$$\rho = \frac{Z_1 - Z_2}{Z_1 + Z_2} \tag{3.12}$$

especially at high frequencies. In the worst case, one generates whole oscillating circuits within a part of the cable. Noise on this level falsifies the actual TTL signal by changing the shape of the pulse, and by causing pulse avalanches due to reflections from the input end of the external circuit to the photon counting head. This changes the count rate significantly and uncontrollable. Hence, impedance matching is very important in order to process the signal correctly. The signal must be terminated dependant on the actual data acquisition environment.

3.2.3 The Light Pipe Option

The whole concept of the detector relies on flexibility. Thus, there are several modes of operation. First, it is possible to use the PMT as an x-ray detector using light pipes. In this configuration, the x rays are converted to visible light by an appropriate scintillator screen (see chapter 4). This secondary VIS signal is then coupled into an optically transparent light guide made of a relatively long lucite rod (transmission factor ~ 0.48 m^{-1} [30]) using optical grease for refractive index matching. ($n_{\text{lucite}} \sim 1.49 - 1.51$) Total internal reflection within the lucite pipe then directs the light signal directly to the sensitive area of the PMT tube. Only light emitted within a certain cone angle will be incident on the rod surface at the critical angle or greater and therefore undergoes total internal reflection [26]. The fractional solid angle is calculated as

$$F = \frac{1}{2}(1 - n_1/n_0) \tag{3.13}$$

where n_0 is the refractive index of the light pipe material and n_1 of the surrounding area. For $n_0 = 1.5$ (lucite) and $n_0 = 1$ (air) this will be about 16.7 % of the isotropically generated light directed in one direction. To avoid background light penetrating the sensitive area and light losses, the light pipes have a polished smooth regular surface (see appendix C.1) and are shielded by a reflective coating, in this case aluminium foil (aluminized mylar has also been used). Great influence on the efficiency may be achieved by special designed tip shapes which in some cases may lead to an increase of the relative efficiency of about 10 % [30]. Fakra *et al.* [8] recommend a flat tip for use with single crystal scintillators and conical tips with a 1 mm flat top when a phosphor powder is used. Nevertheless, in this work, we use flat light pipe tips which expose the whole face of the lucite rods of 3.25, 3.95 and 4.75 mm diameter. This makes repolishing of the surfaces easy, enables simple exchange of different scintillators and leaves the light pipe stiff and stable in position. Additionally, the entire x-ray beam cone has large clearance on the sensitive area.

The light pipes are designed in such a way that they can be mounted to provide vacuum tightness, no vacuum window is needed in this configuration. To guarantee optimal visual contact between light pipe and the PMT, the integrated counting head is slightly spring loaded from the back of the detector housing. Optical grease is used for better optical connection.

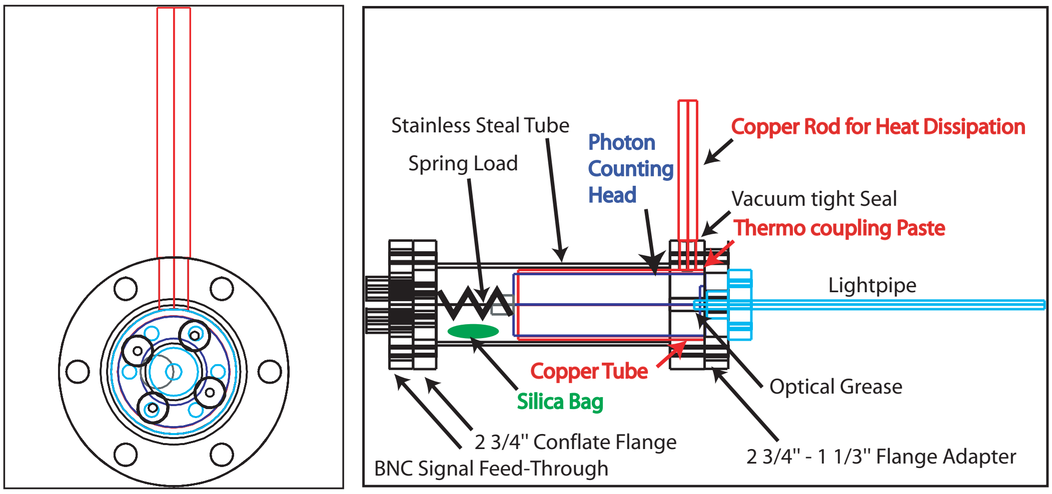

Figure 3.5: **CAD Drawings of the Light Pipe Detector.**
Front view of the detector (left).
Side view of the detector (right).

From figure 3.5 one can easily notice that the light pipes where chosen to be very long in comparison to its diameter. This offers two advantages: first, in this configuration, the light pipe can sit inside the piezo stage with the PMT-tube set back far enough to allow for a large scanning range. Second, the PMT can be kept far away from the stages and therefore the exposure to electromagnetic fields are held to a minimum.

3.2.4 The Microscope Objective Option

Another operating mode of the detector is as a visible light detector, *i.e.* for luminescence measurements. In this mode, a 20× DIN standard microscope objective is used, mounted on a carrier tube. This tube slides over a directing tube which acts as an objective slide (see figure 3.6). It is possible to adjust the distance between the sensitive area and the microscope objective and so the fraction of the photocathode that is actually illuminated. To prevent helium getting into the PMT housing, a vacuum window is provided. Using this configuration, it is also possible to run the detector as an x-ray detector. In that case, copper caps designed for scintillator mounting are provided that can be used to cover the microscope objective allowing for pre scanning to look for interesting sample regions.

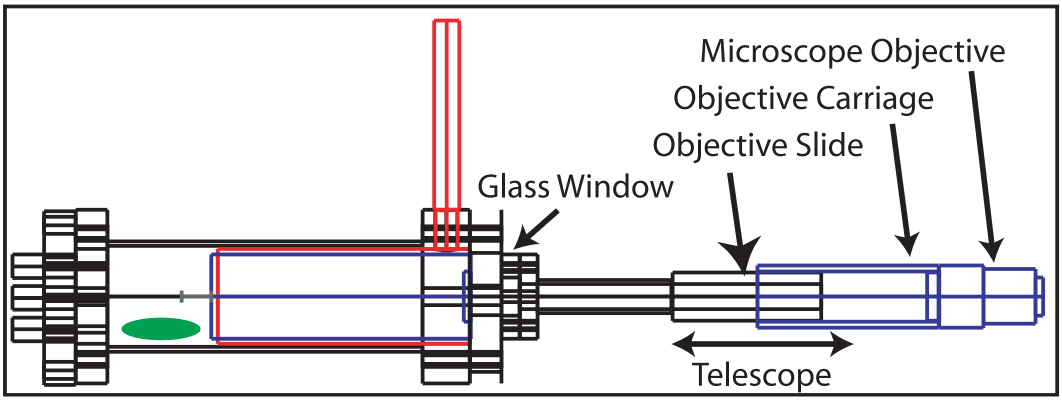

Figure 3.6: **CAD Drawing of the Microscope Objective Detector** (side view).

3.3 Detector Characteristics

3.3.1 Response of the Microscope Objective Detection System

The best way to measure the response of the microscope objective detector would be to compare its count rates to those of a calibrated detector analogous to the PMT/light pipe combination (see 3.3.2). In our case, we just do a rough estimation. Thinking of a point source in the focus of the microscope

$\frac{\Omega(\text{det})}{4\pi}$	T_{glass}	$\frac{\text{TTL pulses}}{\text{incident photons}}$	total fraction
4.2 %	82 - 93 %	3.5 % @ 563 nm	0.12 - 0.14 %
		14.9 % @ 400 nm	0.522 - 0.82 %

Table 3.1: **Sensitivity of the Visible Light Detector.** Basic losses emerge from the confined solid angle of the numerical aperture, the glass window absorption and the quantum efficiency of the photocathode.

objective, the first important factor is the numerical aperture of the objective ($N.A. = 0.4$). The solid angle that is covered is

$$\Omega_{\text{det}} = \int_0^{2\pi} \int_0^{\sin^{-1}(N.A.)} \sin\phi \; d\phi \; d\theta = 0.525 \tag{3.14}$$

and therefore, only a fraction of $0.525/4\pi = 4.2\%$ of all emitted photons is collected. Further in the beam path, some light will be absorbed by the vacuum window (see figure 3.6). Since we are not exactly sure what kind of glass is used, we take indices of refraction from about 1.48 to 1.85 into account. For two index of refraction interfaces at the glass window, this corresponds to a transmission of about

$$T = \left(1 - \left(\frac{1 - n_{\text{glass}}}{1 + n_{\text{glass}}}\right)^2\right)^2 \sim 83 \text{ to } 93 \ \% \tag{3.15}$$

The last step of consideration relates to the sensitivity of the photocathode (see figure 3.3). For example, at 563 nm, there will be about 3.5 % of photons converted to TTL pulses, at 400 nm about 14.9 %. All together, the total fraction of detected pulses per photon created in the point source will be about 0.12 - 0.14 % at 563 nm and 0.522 - 0.82 % at 400 nm. A summary of these estimations is presented in table 3.1.

3.3.2 Response of the Light Pipe Detection System

To measure the response of the x-ray detection system, an International Radiation Detectors, Inc. AXUV 100 Al photodiode was used. According to Gullikson *et al.* [31], these diodes offer an internal quantum efficiency of 1 in the soft x-ray range. Basically, an AXUV photodiode is built as shown in the left part of figure 3.7. Usually, several dead layers (*e.g.* to prevent VIS light sensitivity) are followed by a n-doped active region and a p-doped substrate region.

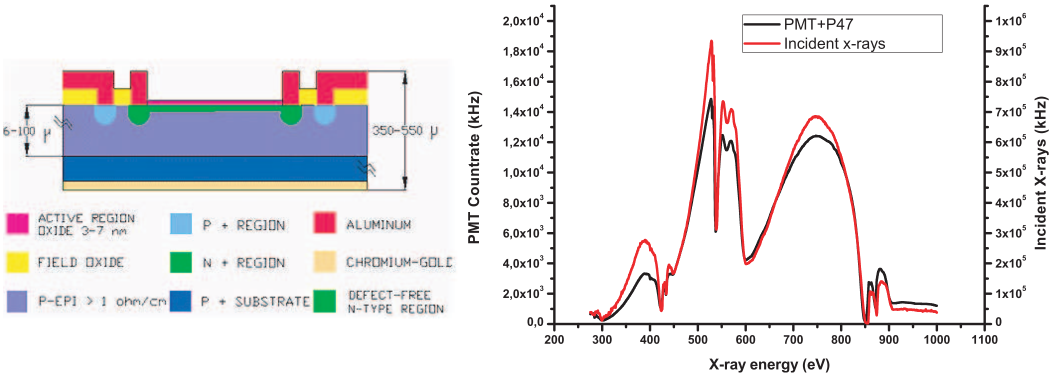

Figure 3.7: **The AXUV Photodiode.**
Construction of the AXUV photodiode (left). Several dead layers are followed by a n-doped active region and a p-doped substrate region. The photodiode is built in such a way that experimental quantum efficiencies of 1 are achieved within the soft x-ray region.
Comparison of the x-ray flux measured by the photodiode (red curve) to the count rates of the PMT detector (right).

Once the absorption A of the photodiode is known as a function of the incident x-ray energy E, the theoretical response for soft x-rays as a function of incident angle ϕ is

$$S_{\mathrm{AXUV}}(E) = \frac{E}{w}A(E) = \frac{E}{3.65\ eV}\exp\left(-\frac{1}{\cos\phi}\sum_i \frac{t_i}{\lambda_{\mathrm{i}}}\right)\frac{nA}{6.24\cdot 10^6\ kHz} \tag{3.16}$$

where $\mathrm{t_i}$ and λ_i are the thicknesses and the x-ray attenuation lengths of the dead layers, respectively. The mean electron-hole-pair production energy w is about 3.65 eV for silicon. One crucial problem for absolute calibration is the knowledge about the dead layer thicknesses. These are roughly specified by the distributing company but would have to be measured for an exact treatment. Usually, materials as carbon, silicon dioxide and bulk silicon may have played a role during the manufacturing process. In addition, we were not sure about where exactly the aluminum comes into play.

If all parameters listed above would be known exactly, the response function of the PMT/lightpipe/scintillator detector could be calculated as

$$S_{\mathrm{PMT}}(E) = S_{\mathrm{AXUV}}(E)\frac{I_{\mathrm{PMT}}(E) - I_{\mathrm{PMT\ dark}}}{I_{\mathrm{AXUV}}(E) - I_{\mathrm{AXUV\ dark}}} \tag{3.17}$$

In our case, the second part of equation 3.17 was calculated from measurements at different x-ray fluxes and for continuous x-ray energies and the first part was calculated taking only a 100 nm aluminum dead layer into account. The x-ray attenuation lengths for aluminum were taken from the "Henke data base" [32, 33]. The result is shown in figure 3.8.

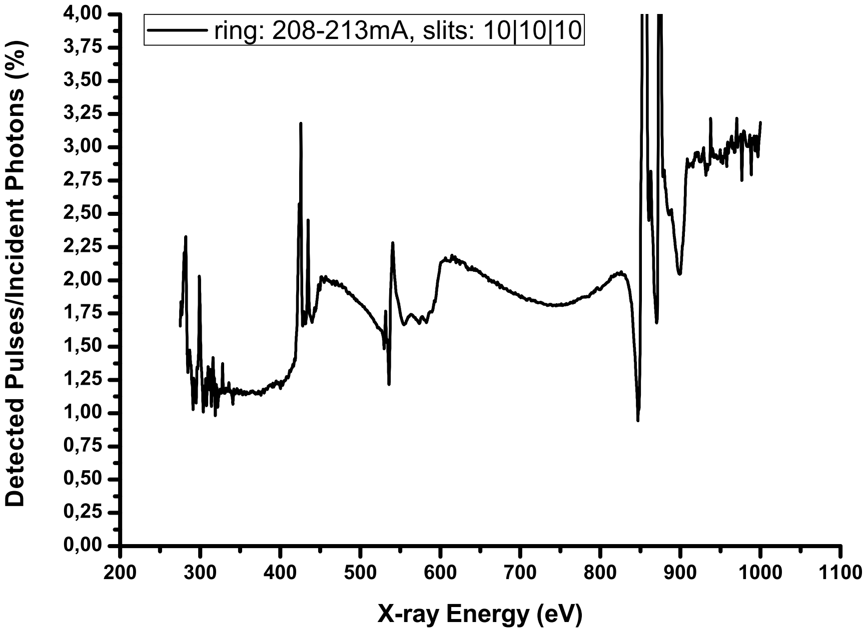

Figure 3.8: **Absolute Response of the PMT/Lightpipe/P47 Detector.** An undulator spectrum was taken for energies from 275 to 1000 eV with a step size of 1 eV. In a timely close manner, the same spectrum was taken with an AXUV photodiode where the response in principal can be calculated theoretically. Both curves are corrected by their dark signal and the response calculated according to equations 3.16 and 3.17.

The data presented in the graph was obtained by measuring the PMT count rate throughout energies from 275 to 1000 eV with a step size of 1 eV continuously. Directly after that, the photodiode that was mounted at the same z-position regarding the x-ray beam, was inserted and the photocurrent was measured for the same energies. A comparison of both spectra in terms of count rate is shown in the right part of figure 3.7. The diode was implemented unbiased and the current measured by a current gauge. This procedure was recommended by Jeffrey Keister, NIST. The entrance- and exit slits were all chosen 10 μm to obtain highest available energy resolution. To maximize flux, zone plate and order sorting aperture were taken out of the microscope and distances were minimized. The experiment was done at X1A2 in helium atmosphere at about 630 torr. As can be seen, the efficiency of the detector in this very simple configuration, where P47 powder is attached to the light pipe by hand and all detector parameters are chosen rather simple and convenient than efficient, there are still about 2 % of x-ray photons converted into electrical TTL pulses throughout all energies. Remarkably, we detect specific features around the carbon (284.2 eV), the nitrogen (409.9 eV), and the oxygen (543.1 eV) edges. Since these features were highly reproducible for different x-ray fluxes at different times, it is unlikely that these are residues resulting from atmospheric turbulence within the STXM chamber. A much better interpretation of these features is the following: usually, within the dead layers of the AXUV photodiode, silicon-dioxide, carbon and nitrogen are used as materials. At the crucial energies, there therefore is more absorption in the dead layers of the diode which do not contribute to the electron-hole-pair production and the photocurrent drops leading to the observed lines in figure 3.8. At 850 to 930 eV, cerium, the P47 activator material, seems to play a dominant role causing very high peaks. In addition, the photocurrent in this regions dropped to almost 0 due to the low undulator flux in combination with high nickel absorption on beam line mirrors (see chapter 2.1.3) and so gives another reason for the singularities. In general, the curve at these energies is not as reliable in comparison to the lower energy regions. The overall tendency of the curve goes upwards. This is a result of the quantum efficiency of P47 behaving as $E^{0.64}$.

3.3.3 Comparison with the Silicon Detector (SIDET)

General Description of the SIDET and its Problems

The silicon detector used in the inboard STXM at X1A2 has been described by Feser [23] as well as in a review by Hornberger [19]. A comparison of the

PMT/Lightpipe setup with the well characterized SIDET is useful. But to do this, a basic understanding of the SIDET, both its capabilities and limitations is necessary.

At the time it was constructed, the SIDET was basically designed to gain the additional information of spatial intensity distribution for phase contrast imaging. Therefore, eight p-n-junctions serving as photodiode segments where embedded in thick, high resistivity n-type silicon. Segments are read out individually and current integrated by signal processing electronics. The segmentation and the n- as well as the p-type side can be seen in figure 3.9.

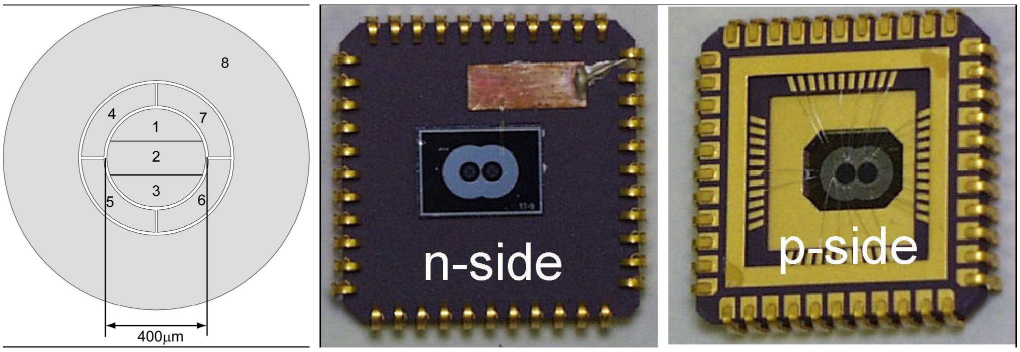

Figure 3.9: **The Silicon Detector.** (Images taken from Feser [23].)
The SIDET chip consists of eight separate segments that can be used for phase contrast imaging (left).
The n-type side of the SIDET detector. Two segmentations are mounted on one chip (middle).
The p-type side of the SIDET detector (right).

By the designer and the operators well known problems have always been noise, calibration and dynamic range. When the p/n junctions are biased in the backward direction, a leakage current flows. Radiation damage causes this dark current to increase significantly over time scales of one hour in regular operation. Although this effect is reversible by annealing at 350°C from time to time, its behavior is highly unpredictable and therefore makes calibrating the detector extremely difficult. In back illumination mode on the other hand, leakage current is a little higher but remains more constant over time. Annealing the detector chip is not required as often. The dark current of course is amplified by thermally generated electron hole pairs in the depleted detector region and the x-ray signal generated by the electron hole pairs formed in the absorption process.

Another problem with this detector is the dead time of the charge integrating electronics which occurs at about 100 μs and hence causes a 10 % signal loss for dwell times of 1 ms. This means a critical performance forfeit especially for large time consuming scans. The silicon detector segments are not 100 % independent from each other, in other words there is detector channel crosstalk due to capacitive coupling between the preamplifier outputs and the inputs of other preamplifiers. Additionally, the energy response differs for the segments respectively. This has great impact on the reliability especially of point spectra in the case where the SIDET is not calibrated perfectly which is valid in most practical cases.

Scanning Range, SIDET vs. PMT/Light Pipe/P47

One crucial advantage of the light pipe setup was already noted in section 3.2.3. The scanning range of the light pipe within the x and y direction of the scanning stage is much bigger than for the SIDET where a 4.75 mm diameter stands against a 40×40 mm^2 square that has to fit into a 50×50 mm^2 stage frame. Another advantage of the PMT detector is that the detector can be kept far away from the stages and therefore the exposure to electromagnetic stray fields are held at a minimum.

Point Spectra, SIDET vs. PMT/Light Pipe/P47

To compare the point spectra behavior of the two detectors in the Inboard STXM reliable, the sample mount was completely removed from the microscope. Instead of a specimen, the chamber gas atmosphere between the entrance window and the detector was used as a sample. To take an I_0 reference spectrum, the chamber was completely pumped down to about 2 mtorr and refilled with helium to about 610 torr and an I_0 point spectrum in the desired energy range and resolution taken. After the I_0 spectrum was collected, the chamber was slightly vented with air and the pressure increased by about 40 torr. Then the I spectrum was collected.

All scan parameters where adjusted in such a way as to optimize the spectra with respect to the detector capabilities respectively. Therefore, the PMT spectra were done at dwell times of 200 ms whereas the SIDET was operated at 5 ms dwell times to avoid saturation of the detector. The scintillator used in conjunction with the PMT detector was P47 which was applied without any binder such as gelatin to avoid additional features coming from the binder. P47 was used in powdered form, mounted onto a glass slide using optical grease (refer to chapter 4.5.1).

Even though the SIDET was calibrated and in most cases no saturation occurred, the point spectra depend highly on the evaluated segment of the detector. In other words, the energy response of the segments depends on their configuration and surface. This might be due to dead areas in the silicon that may vary in size between the different segments. The point spectra of the PMT/lightpipe/P47 configuration were nicely reproducible. It was sometimes possible to find SIDET detector segments whose spectra showed qualitatively similar results. Nevertheless, these are not shown here due to their unreliability. An example of an oxygen and nitrogen spectrum taken by the PMT detector is shown in figure 3.10.

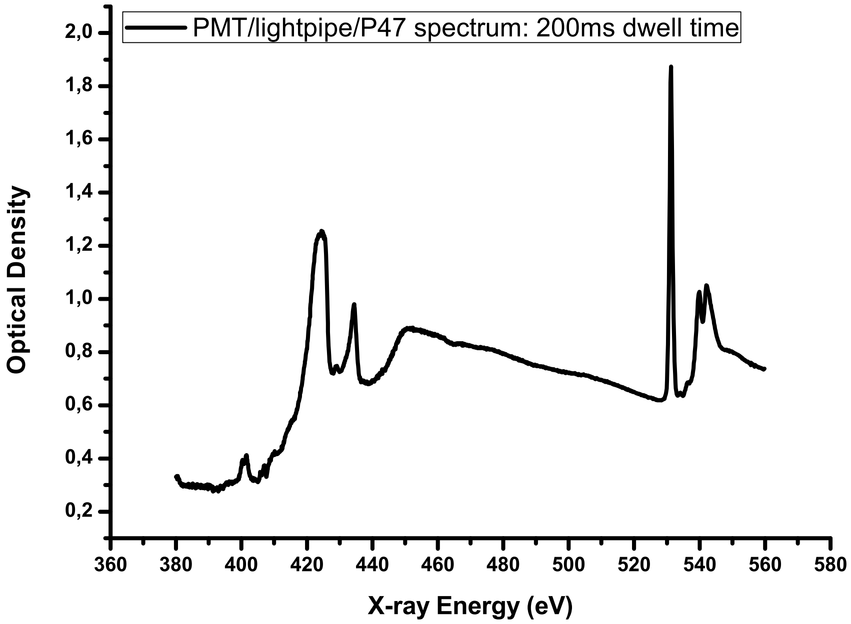

Figure 3.10: **Oxygen and Nitrogen PMT/Light Pipe/P47 Point Spectra.** Pi and sigma bonds of both oxygen around 543 eV and nitrogen around 409.9 eV were detected. The SIDET always showed results that were not reproducible and highly depended on the evaluated segment of the silicon chip and therefore is not shown here.

Nevertheless, the SIDET, although not reproducible, always showed features within the spectrum not recorded by the PMT. Since it cannot clearly be said if these are real it is necessary to compare point spectra with the proportional counter and the relative energy response with a calibrated photodiode (sections 3.3.2 and 3.3.4).

Scans, SIDET vs. PMT/Light Pipe/P47

To estimate the actual imaging quality of the PMT/Light Pipe/P47 detector, we looked at a 30×30 μm^2 region of a $ZnCO_3$ sample that was mounted on a copper grid. The spatial resolution due to the pixel size was 0.3×0.3 μm/pixel. This region was scanned in a STACK procedure (see chapter 2.2) at energies from 520 to 570 eV with a step width of 0.4 eV with both the PMT and the SIDET. Images obtained at 529 eV are shown in figure 3.11 (A). Whereas the SIDET in the high flux areas (blue) tends to saturate, the PMT does not and therefore shows more structure. In the high absorption areas (red) results compare. Figure 3.11 (B) shows the two dimensional fourier transformation of the image. Since an image is collected line per line, it can be interpreted as a time dependent intensity function. Hence, the fourier transformation reflects the periodic noise level picked up by detector and electronics. Expected noise features at 60 and 120 Hz were absent with both detectors. 150 Hz peaks could be identified in both cases but not be related to noise. More likely, these 150 Hz are intrinsic image features.

As explained in chapter 2.2, a STACK can be used for absorption spectroscopy. Areas with high flux are chosen as I_0 reference signal and image features that want to be studied as I regions. An IDL program called Stack_Analyze by Chris Jacobsen is used to calculate the optical density within these two regions for each image respectively resulting in an absorption spectrum. The results for the STACK described in this section are shown in figure 3.12. The general characteristics of both detectors are similar. The broad peaks that can be seen in the figure state the sigma bonds of $ZnCO_3$. The spectra obtained with the PMT/lightpipe/P47 detector show a significant dip at the K1s oxygen absorption edge at 543.1 eV. This is due to the oxygen in P47 - $Y_2SiO_5 : Ce$ and states a problem for spectra measurements at these energies. At an energy of 534 eV, the SIDET spectrum shows an additional peak that was not collected by the PMT. This reflects the carbon bonded to three oxygen atoms in the $ZnCO_3$. It is not quite sure why the PMT did not detect this bond. The fact that this peak consists of one single data point infers that maybe the energy resolution was not fine enough. Response problems of the P47 scintillator may also be taken into account.

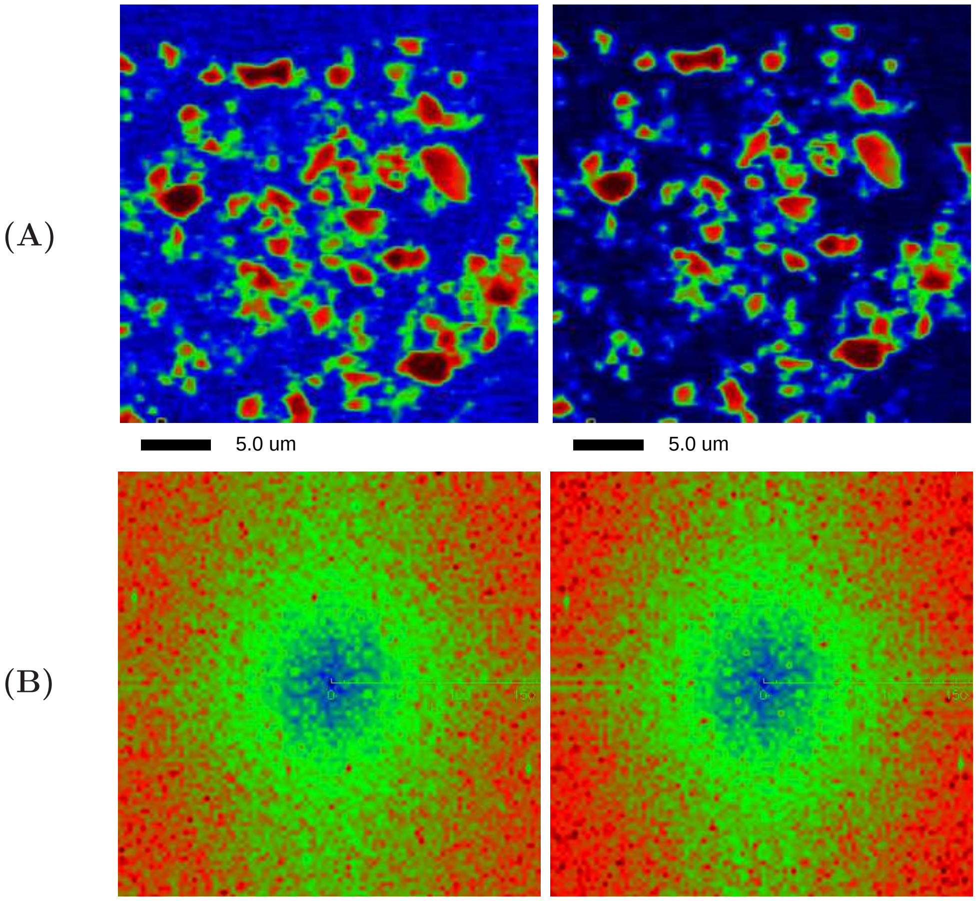

Figure 3.11: **Comparison of PMT/Light Pipe/P47 (left) (P47 on Glass Slide with Gelatin Binder) and SIDET (right) Stepper Scans.**
(A) 100 × 100 stepper scans of a $ZnCO_3$ sample @ 529 eV with a resolution of 0.3×0.3 μm/pixel.
(B) 2D power spectra: a quasi 2D fourier transform of the signal in scanning time can reveal noise frequencies (here at about 150 Hz).

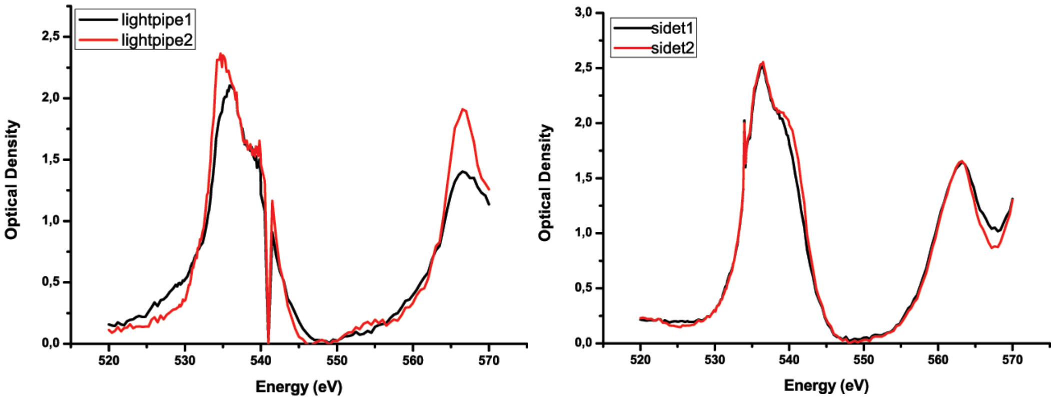

Figure 3.12: **Comparison of PMT/Light Pipe/P47 (left) and SIDET (right) Stepper Scans: STACK Spectra.** 100 × 100 stepper scans of a $ZnCO_3$ sample from 520 to 570 eV with a resolution of 0.3 × 0.3 μm/pixel. The peaks correspond to sigma bonds in $ZnCO_3$. The PMT spectrum shows a significant K1s oxygen feature at 543.1 eV due to the oxygen in P47 - Y_2SiO_5 : Ce. At 534 eV, the SIDET spectrum shows an additional peak that was not collected by the PMT. This is the carbon bonded to three oxygen atoms in the $ZnCO_3$.

3.3.4 Comparison with the Proportional Counter

General Description of the Proportional Counter

Because of the problems that emerged in the last sections concerning the reliability of the SIDET, it also makes sense to compare the PMT/Lightpipe setup with another well established x-ray detector, the proportional counter of the outboard (X1A1) STXM. This continuous flow proportional counter is described by Feser [23]. It has no dark noise which is ideal for low count rates, good signal to noise and is insensitivity to visible light. Since it is a counter, a comparison can be done directly by comparison of the raw count rates under identical x-ray illumination conditions.

In principle, the proportional counter works like a Geiger counter. Photons are directed into a gas chamber of a noble gas, in this case argon, where they ionize the molecules creating ion-electron pairs. An applied electromagnetic field causes the ions to drift to a cathode, the electrons to an anode. The strong field around the anode causes high electron velocities and therefore creation of secondary electron production which leads to an avalanche effect with an amplification of several thousand electrons. Unlike Geiger counters, the amount of charge created is proportional to the primary charge whereas in the Geiger counter setup one has to deal with saturated signals. Nevertheless the proportional counter also may saturate.

Count Rates of the Proportional Counter vs. PMT/Light Pipe/P31

The limit of the PMT detector became most obvious comparing it with the counter. Whereas the counter usually can be operated without dark noise and achieves high sensitivity resulting in high count rates above 1 MHz, the PMT has to suffer dark noise resulting from stray light and is much less sensitive. Dark noise can be limited below 20 kHz covering the microscope chamber in several layers of aluminum. Efficiency highly depends on the layer thickness and density of the used scintillator and the light guide coupling. In general, efficiency is below the proportional counter.

Point Spectra, Proportional Counter vs. PMT/Light Pipe/P31

Collecting point spectra, efficiency problems of the PMT emerged. Whereas the proportional counter could be operated at 25 μm slits resulting in high energy resolution, the PMT had to be operated at 70 μm to increase the incident x ray flux. Measurements were done six weeks after the SIDET comparison. By that time, the P47 scintillator largely lost efficiency (see chapter 4.4.3) due to uncertain effects. Count rates with P31 were three times better than with P47 though the PMT response at the emission wavelength of P47 (400 nm) is 2.5 times higher (see figure 3.3, refer to chapter 4.4) than for P31 (520 nm).

Absorption spectra on CO_2 gas were done with both detectors, respectively. Both detectors were operated with a 100 ms dwell time and an energy step size of 0.2 eV. The sample mount was completely removed from the microscope and the I_0 reference signal collected. The air was slightly depleted by a helium flow between zone plate and detector. Then, carbon dioxide was blown in and the absorption measured again. The resulting optical density is shown in figure 3.13.

The count rates for the proportional counter were still much higher than for the PMT and were scaled down. Nevertheless, most CO_2 absorption lines (C K shell of CO_2: K1s@290.77 eV [34], K2s: not specified, K3s@292.74 eV, K3p@294.96 eV, K4s@296.16 eV, K4p@296.38 eV [35]) that were detected by

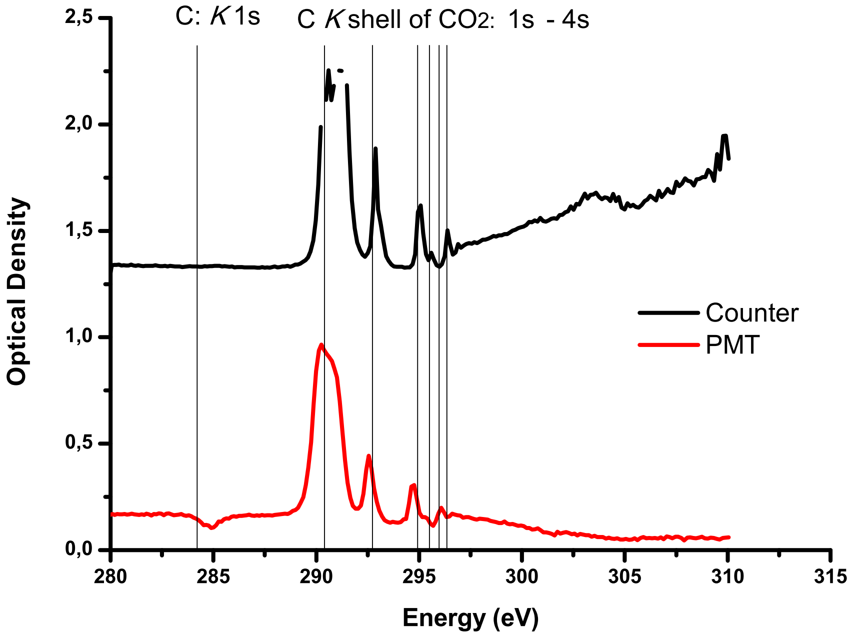

Figure 3.13: **Comparison of PMT/Light Pipe/P31 and Proportional Counter: Point Spectra.** The counter signal was scaled down. The C K shell absorption lines of CO_2 that were detected with the counter were also identified by the PMT/lighpipe setup. The PMT shows a relict of carbon K1s which could not be normalized out due to the bad signal to noise ratio.

the proportional counter could be identified by the PMT detector. At 284.2 eV the PMT shows a relict of the Carbon K1s edge resulting from nonlinearities due to the small count rates combined with dark noise that of course is the same at all times. Carbon absorption is always present due to low concentrations on mirrors and other places in the beam path.

Conclusively, the efficiency of the PMT/lightpipe/scintillator detector has to be improved to become an alternative to the proportional counter. For energies around the nitrogen edge, where the SIDET detector was used implemented in X1A2, it is an alternative and point spectra reliability can be expected.

Scans, Proportional Counter vs. PMT/Light Pipe/P47

As already explained in 3.3.4, it is hard to achieve the efficiency and dark noise characteristics of the proportional counter by a visible light sensitive detector as it is the PMT. Therefore it is necessary to find out where the limits of the PMT/lightpipe/scintillator are. Since the proportional counter has shown good performance for all kinds of samples in the past already we here compare the results that were achieved by the PMT using two samples with two different "degrees of difficulty". The easier sample is an oceanic sample with low absorption contrast and high organic concentration. The other samples are matrix minerals from ALH84001, a Mars basaltic meteorite that dates from the early formation of Mars, approximately 4.5 billion years ago (see left part of figure 3.14). The rock contains carbonates and magnetite which formed later in the history of the meteorite, in cracks in the matrix, during a time on Mars when scientisits believe there was liquid water on the surface of Mars, the Noachian Epoch (3.5-3.8 billion years ago). It is the meteorite which Dave McKay's group at Johnson Space Center claims that it shows evidence of life on Mars. Using STXM, organic matter associated with both the carbonates and magnetite has already been found. Nowadays, scientists look at the older matrix minerals to see if the organic associated with these minerals is similar to the organic associated with the carbonate and magnetite. The answer to this is that the organic in the matrix is very different than the organic that can be found in the carbonates. Because of its high absorption contrast and low concentration of organic material, we use this sample to determine the limits of the detection system. As can be seen in the right part of figure 3.14, the "soft" organic material from the ocean (blue curve) delivers a reasonable STACK spectrum (for an explanation of STACK see chapters 2.2 and 3.3.3). Thereby we scanned a 100 × 100 pixel region of 0.2 μm per pixel at a dwell time of 5 ms. Both entrance and exit slits were chosen 70 μm, respectively. Scans within the stack go from 280 to 291 eV with an energy resolution of 0.3 eV. Clearly, the organic material reflects in a distinct carbon peak at around 290 eV. The much “denser” meteorite samples are much more of a challenge. Low count rates in the high absorption areas in combination with dark counts lead to an “over counting” and falsifies the absorption spectrum. This leads to a negative peak in the spectra. For ALH84001, the experiment was done for two different regions (black and red curve) for energies from 280 to 310 eV with an energy resolution of about 0.3 eV.

Conclusively, the detectors efficiency as well as the dark count have to be improved in order to be able to detect even small concentrations of organic materials in high absorbing samples.

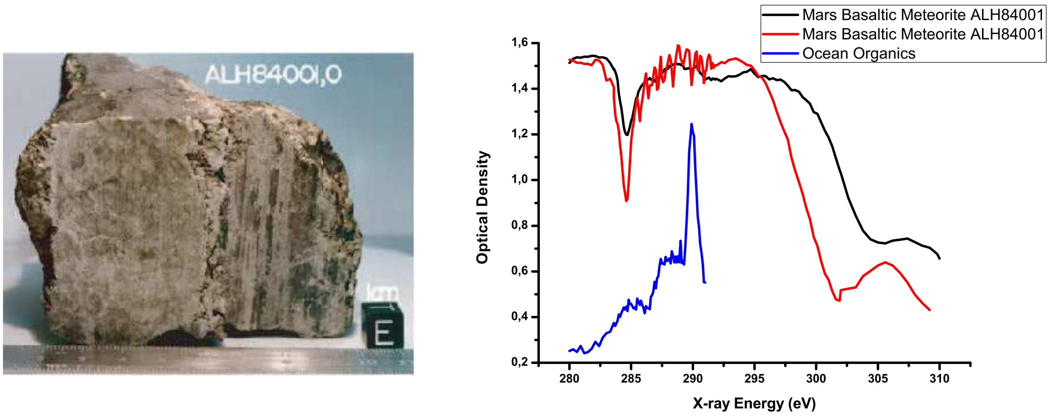

Figure 3.14: **The Mars Basaltic Meteorite ALH84001.**
Photograph of the Mars Basaltic Meteorite ALH84001 (left). (Image taken from the meteorite curatorial web site at Johnson Space Center in Houston, Texas.)
STACK spectra obtained from 100 × 100 stepper scans of 0.2 μm per pixel at a dwell time of 5 ms (right). The black and red curves show the optical densities for two different regions of the ALH84001 sample. Due to the high absorption contrast in combination with PMT noise, carbon features always present in the beam path do not normalize out and remain as negative peaks. In the red curve, small peaks in the 290 eV region let assume organic material on the sample. In contrast, a relatively optical thin oceanic sample with high enough signal to noise ratio all over the sample region shows a distinct carbon peak (blue curve).

Chapter 4

An Inorganic Scintillator Review

4.1 Clarification of Terminology

Since scintillation terminology is often used in different and confusing ways by different authors, basic terms as summarized in a very analytical definition by Princeton Instruments Inc. [36] shall be reviewed. A terminology tree can be seen in figure 4.1.

One speaks of **luminescence** as a general light emission phenomenon that can be equally observed at any temperature, in contrast to the hot body spectrum, also referred to as cold-light emission. Some energy sources excite an electron in a quantized energetic system (*e.g.* atom) from a low-energy state into a higher-energy state. Then, the electron emits the energy in the form of a photon so it can fall back to its "ground" state. Intermediate processes between absorption and emission duration lead to loss of correlation between phases of absorbed and emitted light. This is contrasted by reflected and stray light, in which the phase correlation can always be observed.

In the case of light absorption in the UV/VIS/NIR spectral region and an emission at a longer wavelength mostly in the VIS/NIR range indicating a vibrational energy loss, the term **photoluminescence** is used.

The delay time between absorption and emission processes, serves as a criterion

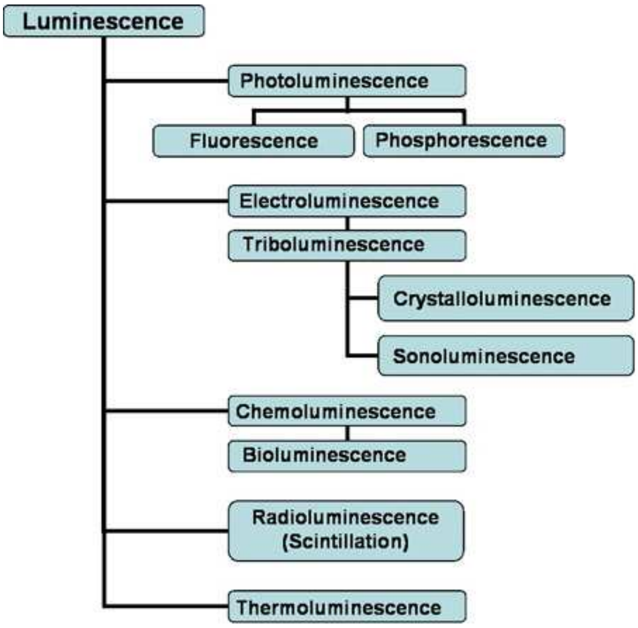

Figure 4.1: **The Terminology of Luminescence.** Beyond the terms defined in the text, there are many other phenomena with their own specific term (Image taken from the Princeton Instruments Inc. web page [36].)

to distinguish **fluorescence** and **phosphorescence**. To give a rough feeling, the delay times for fluorescence are from about 10^{-12} to 10^{-7} s and much longer for phosphorescence even up to a few hours or days. For delay times somewhere in between, one also often talks about **delayed fluorescence**. In addition, phosphorescence emission usually takes place at longer wavelength light than fluorescence [26].

Scintillation (**Radioluminescence**) results from excitation by high-energy particles or radiation as α-particles, neutrons or x rays.

In this work the author will use these terms as they are defined in the current literature. Terms such as scintillation and fluorescence will be interchanged.

4.2 The Electronic Structure and Mechanism of Inorganic Scintillators

Unlike organic scintillators where the scintillation process is an inherent molecular property, it is a crystalline property in inorganic scintillators. For practical use one mostly deals with crystal structures that are activated by added impurities. Nevertheless there are also self activated scintillators [30].

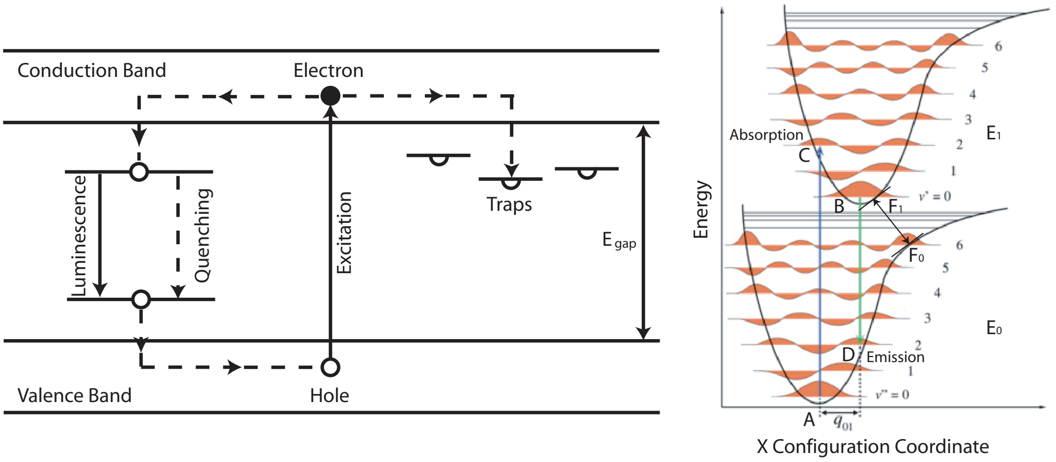

Figure 4.2: **Illustration of Phosphor Theory.**
A sketch of the energy bands in impurity-activated crystal phosphors, showing excitation, luminescence, quenching and trapping processes (left). (Concept taken from Birks [30] and altered.)
A potential energy diagram of a luminescence center or molecule (right). (Image taken from WIKIPEDIA [37] and altered.)

Due to the crystal structure, the outer electronic energy levels of the atoms respectively merge to the well known band structures as shown in the left part of figure 4.2. Usually, scintillator materials are chosen as insulators with completely filled valence and completely empty conduction band orbitals separated by a forbidden zone with large energy gap E_{gap}. An incoming photon with sufficiently high energy will lift an electron from the valence to the conduction band leaving positive holes. (This excitation process actually is not that simple. A detailed discussion will be given in chapter 6.6.1.) Some electrons remain free in the conduction band and one observes photoconduction, some form exciton-bonds with the holes and no net charge is transported.

One would expect an immediate recombination process via emission of the same photon energy. However, this return of the electron to the left hole via the reversible process would be inefficient.

Hence, doping this "perfect" crystal with impurities is necessary to create local electronic energy levels in the normally forbidden region. If these **activators** are unoccupied, excitons or electrons from the conduction band can enter these centers of which there are three kinds, luminescence, quenching and meta stable [26, 30, 38].

Luminescence centers are where photo emission takes place. They are formed from impurities, interstitial ions and/or defects and introduce local discrete energy levels corresponding to the ground and excited states of the center. Photo emission can only take place when both ground and excited states are occupied by a hole and an electron respectively.

So called **quenching centers** are in principal formed in the same way as luminescence centers but offer other ways of capturing electrons and holes at the activator site. Certain non radiative decay processes will be possible causing a decline in efficiency.

Also, there are meta stable **traps**, excited configurations with forbidden transition to the ground state. From these meta stable traps, there is either the possibility for the electrons to be released from this configuration after a delayed time (phosphorescence) when thermal fluctuations cause some increment of energy, or non radiative decay. Traps are often caused by lattice disturbances besides those caused by quenching centers and exist for both electrons and holes. These non-quenching lattice disturbances are what cause the so called **afterglow** (ghosting).

In the perfect scintillation process, electrons in the conduction band migrate to luminescence centers where they de-excite with typical half lifes of about 50 to 500 ns. Since the migration times of electrons and holes are much smaller, the half life determines the scintillator time characteristic. Most scintillators show more than just one single decay time component.

The conditions for photo emission were explored by a theory of Hippel (1936) and Seitz (1938,1939): In figure 4.2, the potential energies of the ground and excited electronic states of a luminescence center are plotted against some configurational coordinate. Curve E_0 indicates the vibrational amplitudes in the electronic ground state, E_1 those of the excited state. Point A and B mark the stable energy positions within the system at the two different energies which will be displaced by thermal vibrations at the order of k_BT at nonzero temperatures.

In the case of an incident photon, absorption occurs via a vertical line $A \rightarrow C$ according to the Franck-Condon principle. This principle states that electronic transitions take place in shorter time periods when compared with atomic or ionic movements. Moreover, Fermi's golden rule predicts the highest likelihood for absorption is in the case where the overlap of ground- and excited state wave functions is large which restricts absorption to the outer boundaries of the E_1 curve. Then, non radiative, thermal relaxation from C to the minimum B happens. The lifetime of the state B depends on the probability of the optical transition $B \rightarrow D$. After the emission process, overall minimum A is re-achieved by another thermal relaxation event $D \rightarrow A$.

Obviously, emission will always happen at significantly lower energies than excitation (**Stokes shift**), but there might be an overlap between absorption and emission bands. These overlaps should be small for an efficient scintillator to avoid self absorption and guarantee high transparency within the emission wavelengths. Small overlap in activator based scintillators therefore makes the material much more transparent to the emission wavelength. This is in contrast to a pure crystal where self absorption occurs.

As seen in figure 4.2, the closest approach to curves E_0 and E_1 occurs at the points F_0 and F_1. If an excited electron is able to reach the point F_1, this may lead to a non-radiative transition to F_0. This process is called quenching. Labeling the relative probability for an emission process k_f and the relative probability for internal quenching k_i, which depends on the relative positions of B and F_1 as well as on the temperature T, then the luminescence quantum efficiency can be expressed as

$$QE = \frac{k_f}{k_f + k_i} \tag{4.1}$$

If F_1 is at an energy W_q above B, the probability that the excited center may be thermally activated to the point F_1 is proportional to the Boltzmann factor $k_i \propto exp(-W_q/k_BT)$ and thus the luminescence quantum efficiency turns out to be

$$QE = \frac{1}{1 + const\ exp(-W_q/k_BT)} \tag{4.2}$$

This equation by Mott and Gurney (1939) is in inorganic crystal scintillators only applicable to the intrinsic quantum efficiency of the luminescence center and not to the overall lattice process where additional competitive processes might occur.

As a thumb rule, it takes about an average of three times the band gap energy to create an electron hole pair for most materials which then can lead to luminescence (*e.g.* silicon: band gap: 1.12 eV, mean electron-hole-pair production energy: 3.65 eV) [26].

4.3 The Choice of the Right Scintillator

Concerning the question as to what scintillator to choose, there are several factors one has to consider. These factors have been discussed by many authors and will be briefly described here [3, 25, 26, 39, 40].

Crucial requirements are a linear conversion of the incident radiation to detectable light as well as transparency to the emission wavelength and a short decay time. Especially for our application the powder should be of good optical quality and have an index of refraction near glass or lucite ($n \sim 1.5$) for photons to be efficiently coupled in the detector system. Of course, the emission spectrum must be matched to the spectral response of the photocathode in the photomultiplier (in our case maximal response at 400 nm, see figure 3.3).

Phosphor films are usually characterized through their conversion efficiency η:

$$\eta = \frac{N_{\text{light}} E_{\text{light}}}{E_{\text{in}}} \tag{4.3}$$

where N_{light} is the total number of optical photons emitted upon interaction with an x-ray quantum and E_{light} is the associated mean energy of emitted photons. E_{in} is the incident x-ray energy. We therefore require large x-ray absorption, that is, high specific gravity and a composition which includes elements of large average atomic number to maximize conversion efficiency. Furthermore high luminescence efficiency under x-ray excitation is required.

One could consider an organic scintillator to use in our application which are much faster. However, because of their excellent energy conversion efficiency, their high absorption efficiency, a good probability for the photoelectric effect and their better radiation damage resistance, inorganic scintillators are favored over organic scintillators.

Furthermore, inorganic scintillators offer a better linear energy response than organic scintillators. The quenching within the inorganic crystal leads to non-linearities. Unfortunately, they are not easy to handle because of their hydrophobicity.

For good photon statistics, the largest possible fraction of isotropically emitted light is required from the scintillator. The factors involved with this requirement are optical self absorption and losses at the scintillator surface for photons at angles greater than the critical angle

$$\Theta_c = \arcsin \frac{n_1}{n_0} \tag{4.4}$$

where n_0 and n_1 are the index of refraction of the scintillation medium and the surrounding medium respectively.

A crucial part in the detector performance relies on the maintenance of the scintillator characteristic over long exposure times. Hence it is very important to characterize radiation damage effects that might occur throughout the illumination process. In inorganic scintillators, radiation damage often emerges from the creation of color centers that absorb the scintillation light and therefore spoil the optical transparency within the emission wavelengths. Radiation damage depends on the dose rate, the type of incident particle, the energy of the particle and the presence or absence of oxygen or other impurities. Some effects are partly reversible by annealing.

4.4 General Properties of some Selected Scintillators

Traditionally, most inorganic scintillators consist of halogen compounds such as NaI(Ti), BGO (Bismuth Germanate), BaF_2, CsI(Ti) and ZnS. Of these, the NaI(Ti) scintillator is most commonly used [25, 30, 38]. The quest for better efficiencies and shorter decay times lead to newer developments such as P43 - Gd_2O_2S:Tb and P47 - Y_2SiO_5:Ce on which the author will focus on in the following and compare them to P31 - ZnS:Cu a classic that ruled the scintillator world for the first half of the 20th century. The "P" numbers here are the phosphor screen symbols specified by the Electronics Industries Association (EIA) of the US.

4.4.1 P31 - ZnS:Cu

Zinc sulphide can be activated with silver or copper which occupy interstitial locations in the crystal and serve as activation sites where incident x rays trigger visible photon cascades as described earlier [39]. It is only available as crystalline powder of mean particle size around 16 to 20 μm and is one of the most efficient and radiation hard scintillators known [26]. Peak quantum efficiencies of about 10^{-3}photons/(nm eV) and a production of one green photon for each 8 to 10 eV deposited into the crystal matrix have been reported [39].

There is a theoretically predicted decay timescale of

$$\frac{I}{I_0} = \frac{1}{(1+At)^2} \tag{4.5}$$

where A is situated somewhere in the regions of 5×10^5 s^{-1} to 4.2×10^6 s^{-1}. Apparently, observations depend on the experimental circumstances and the purity and conformation of the phosphor powder that was used. Most authors agree that 99 % of P31 emission decays to zero within the first millisecond. Some confusion emerges for the emission peaks of P31. Yang *et al.* [41] report the one emission maximum at 520 nm with an emission band width of 60 nm whereas Knoll [26] states this maximum occurs at 545 nm and WIKIPEDIA lists this emission band energy at 531 nm.

One crucial advantage of P31 for imaging applications is a nearly linear response to x-ray flux in the range of 10^7 to 10^{10} photons/(s mm^2) @ 600 eV represented by a x-ray flux response function that goes like F^n, with $n = 1.035 \pm 0.010$ [41]. The almost linear energy response E^m with $m = 0.995 \pm 0.015$ in the soft x-ray range of 300 to 800 eV makes P31 feasible for several different kinds of applications.

In general, absorption features emerge at the binding energies of any of the elements used in the phosphors. In P31, the Zn L absorption edges of first

Type	P31	P43	P47
Composition	ZnS:Cu	Gd_2O_2S:Tb	Y_2SiO_5:Ce
max Emission Peaks	523 nm (green) [26]	545 nm (green) [8]	420 nm (blue) [42]
Decay Time	$\sim$ 1 ms [26]	1 ms [8]	55 ns [8]
Density	4.1 g/cm^3 [26]	7.34 g/cm^3	4.36 g/cm^3
Bandgap of main component	3.7 eV [43] (335 nm)	4.4 eV [44] (282 nm)	5.1 eV [45] (243 nm)
Refractive Index	2.4 [26]	not specified	not specified
max efficiency @ layer concentration	$10 - 25$ mg cm^{-2} (x rays) [26]	not specified	$1.4 - 2.5$ mg cm^{-2} (e^-) [1]

Table 4.1: **Some Properties of the Scintillators P31, P43 and P47.** Note that most of the properties variations are strongly dependant on characteristics such as temperature, grain size, conformation, impurity conformation, *etc.* Therefore, different authors quote different observations.

order at 1022 and 1045 eV; second order at 510 and 525 eV; and also third order at about 340 eV are especially relevant. Some crucial properties of P31 taken from the literature are shown in table 4.1 next to those of P43 and P47.

In the experiments, a single peak was found with an emission maximum at 533 nm. This peak seems to consist of at least three different copper transitions. A multiple peak fit therefore was done as shown in figure 4.3 and results summarized in table 4.2. Except the 449 nm peak, no exact transition of copper can be identified. This is due to the energy structure of copper largely varies in the ZnS, dependant on doping concentration, crystal structure and impurities in the crystal. The size distribution of the scintillator particles also may play a role. The measurements were done without zone plate and order sorting aperture, with open slits, exposure time was between 250 and 300 ms and 100 spectra were averaged, respectively. The intensity variations in the left part of the plot therefore reflect the undulator output flux.

4.4.2 P43 - Gd_2O_2S:Tb

P43 (terbium doped gadolinium oxysulfide) has been widely used in indirect x-ray imaging applications [3]. According to Tao *et al.*, the emission spectrum of light is a discrete distribution between 500 and 900 nm and has a peak at 560 nm (green light). Fakra *et al.* [8] however report the wavelength of

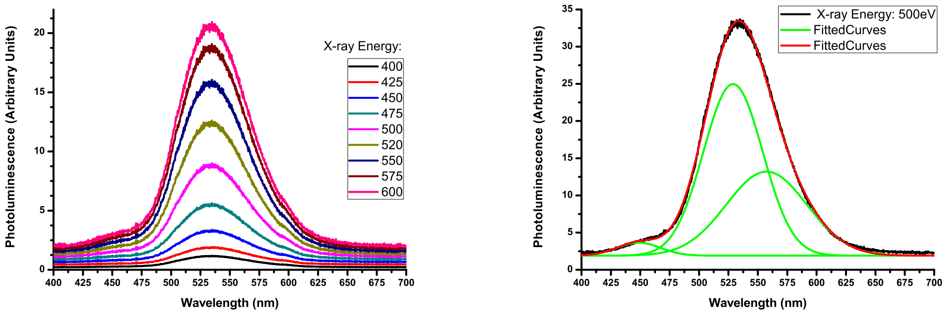

Figure 4.3: **X-ray Stimulated Emission of P31.**
400 to 600 eV x-ray stimulated emission spectra (left). Multiple peaks cannot be resolved. Peak position, width and relative height remain constant for different energies and fluxes. The intensity difference is due to the flux profile of undulator radiation @ 36 mm gap size. Exposure time for all spectra was 300 ms.
Multiple Gaussian fit of a spectrum (right). Three different parts may be identified. The global maximum is at 533 nm.

Peak	1	2	3
λ [nm]	449	529	557
2σ [nm]	36.9	50.5	68.7
h/h_{max} [%]	7.6	100.0	49.0
$\int / \int_{\text{max}}$ [%]	5.5	100.0	66.7

Table 4.2: **X-ray Stimulated Photoluminescence Spectrum of P31.**
Generally, one major peak can be resolved with a global maximum at 533 nm. Having a closer look, this peak is built up of three parts. The table shows peak maxima wavelengths, standard deviations, normalized peak heights and normalized integrated intensities obtained from multiple Gaussian fits.

maximum emission at 545 nm with a decay time of 1 ms whereas Gorokhova *et al.* [44] refer to a decay time of ∼ 600 μs. As explained before, parameters such as particle size, purity and doping concentration and the actual experimental setup affect the characteristics of the phosphor powder and the experimental results. Many trials have been undertaken in order to increase the performance of P43. The addition of a very small amount of Ce (Gd_2O_2S: Tb(0.08 wt%)Ce(0.002 wt%)) leads to an energy efficiency of emission in the visible wavelength range up to 20 %. Hot pressing P43 in vacuum forming solid ceramics can further increase its transparency in the emission region of about 50 %. Thermal quenching can be greatly reduced at cryogenic temperatures. This is due to an inhibition of the ground state vibrational states at low temperatures. (This is discussed further in chapter 6.3.)

The left part of figure 4.4 was taken directly from Gorokhova *et al.* [44] and shows what kind of emission spectrum can be expected for x-ray excitation of P43 as well as pure Gd_2O_2S at about 40 keV. The great impact of impurity doping can hardly be neglected.

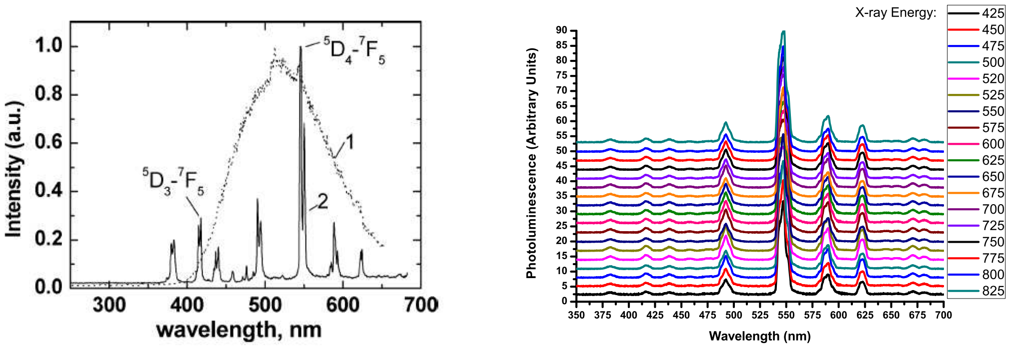

Figure 4.4: **X-ray Stimulated Emission of P43.**
40 keV x-ray stimulated emission spectra of P43 (left). (Image taken from Gorokhova *et al.* [44].) 1: Gd_2O_2S, 2: Gd_2O_2S:Tb,Ce in ceramic form. Integral intensity of Gd_2O_2S is 20× lower than of Gd_2O_2S:Tb,Ce
425 to 825 eV x-ray stimulated emission spectra of P43 (right). Multiple peaks cannot be resolved. Peak position, width and relative height remain constant for different energies and fluxes.

The right part of the figure shows the results for soft x-ray energies from 424 to 825 eV. During the measurements the synchrotron ring current varied from 184 to 179 mA, the undulator gap was operated at 36 mm (see figure 2.2) and the exposure time maximized to the point that no saturation occurred (*e.g.* 80 ms @ 725 eV and 500 ms @ 425 eV). To further improve statistics, we

Peak	1	2	3	4	5	6	7	8	9
λ [nm]	382	417	439	482	546	584	622	671	681
σ [nm]	3.7	3.1	3.4	3.7	3.6	3.8	2.8	3.3	3.7
$h/h_{\max}$ [%]	2.3	3.2	2.3	15.2	100.0	21.9	15.1	3.0	2.3

Table 4.3: **X-ray Stimulated Photoluminescence Spectrum of P43.** Nine peaks were resolved with a 6.5 nm accurate spectrometer. Here, peak wavelengths λ, Gaussian standard deviation σ and the normalized peak height $h/h_{\max}$ are shown.

averaged over 100 spectra respectively. For the measurements, the zone plate and order sorting aperture were completely taken out of the microscope which was operated in helium at about 630 torr.

Nine peaks can be identified (see table 4.3). Due to the low resolution of 6.5 nm for our spectrometer, the peak splitting as expected could not be resolved. Nevertheless, asymmetry of the peaks can be observed which gives a hint for multiple peaks. All peaks where fitted Gaussian, peak wavelength, standard deviations and normalized peak heights shown in table 4.3. The data presented in figure 4.4 as well as a continuous scan throughout the whole undulator spectrum show that neither the peak wavelength nor the standard deviation or the peak height ratios changes for different x-ray energies or fluxes within the obtained resolution. For the flux observation, the exit slit was scanned continuously from 25 μm to 1 mm.

4.4.3 P47 - Y_2SiO_5:Ce

P47 or Y_2SiO_5:Ce has the fastest decay characteristics of all of the phosphors presented in this work with the decay time being 55 ns [8]. This makes it especially useful for time critical experiments. Its wavelength of maximum emission at 400 nm (blue color) matches it exactly to the response curve the PMT used in this study (see figure 3.3). It is a compound material consisting of about 74 to 84 wt% of yttrium dioxide (Y_2O_2), 16 to 26 wt% silicon dioxide (SiO_2) and a low concentration of CeO_2. Although not as efficient as P31, P47 has significant higher luminescence than many other phosphors and a very linear x-ray flux response function that goes as F^n with $n = 1.028 \pm 0.010$ in the range of $10^7 - 10^{10}$ photons/(s mm^2) and a quantum yield that behaves as E^m with $m = 0.64 \pm 0.02$, which is nonlinear [41]. Concerning radiation hardness, P47 looses luminescence intensity with prolonged exposure to x rays.

With photons of 640 eV energy and flux of about 5×10^8 photons/s in a 40 nm size spot, the luminescence decreases about 30 % after 10 min exposure as reported by Fakra *et al.* [8]. For typical exposure times used in STXM this should not lead to a significant change of quantum efficiency for one scan, or for larger exposure times such as that needed to collect a STACK. For a STACK consisting of 100 scans with a dwell time of 200 ms per pixel, with a typical x-ray flux at the detector of about 1000 kHz, this would correspond to a loss of efficiency of only about 0.002 % and therefore be negligible.

More problems seem to emerge from the storage of the phosphor powder. After about six weeks of un-careful storage of P47, the phosphor seemed to lose efficiency. This is probably due to its hygroscopic character. Drying out the powder in the oven did not lead to better results (see chapter 3.3.4). The experimental setup was the exact same as for P31 and P43. Figure 4.5 shows the obtained spectra in the excitation range from 475 to 540 eV with a global maximum at 397 nm. The Spectrum shows four peaks where three of them were fitted Gaussian and the results can be seen in table 4.4. The fourth peak may result from noise integration effects that differ from pixel to pixel of the spectrometer chip. Due to the bad signal to noise ratio even at exposure times of 1 s per spectrum and averaging over 50 data sets, the results are questionable.

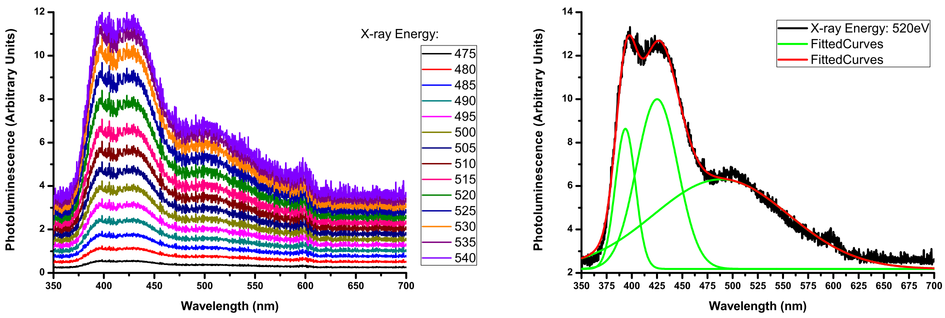

Figure 4.5: **X-ray Stimulated Emission of P47.**
475 to 540 eV x-ray stimulated emission spectra of P47 (left). Multiple peaks cannot be resolved. Peak position, width and relative height remain constant for different energies and fluxes. The intensity difference is due to the flux profile of undulator radiation @ 36 mm gap size. Exposure time for all spectra was 1 s.
Multiple Gaussian fit of a spectrum. Four different parts may be identified (right). The global maximum is at 397 nm.

Peak	1	2	3	4
λ [nm]	394	425	488	598
2σ [nm]	20.0	40.9	133.9	n.s.
h/h_{max} [%]	82.6	100.0	52.8	n.s.
$\int / \int_{\text{max}}$ [%]	23.4	57.9	100.0	n.s.

Table 4.4: **X-ray Stimulated Photoluminescence Spectrum of P47.** the efficiency when it was measured was at its minimum (see text). This curve is built up of four peaks. The table shows peak maxima wavelengths, standard deviations, normalized peak heights and normalized integrated intensities obtained from multiple Gaussian fits. For the fourth peak a fit was not possible.

4.5 Scintillator Screen Deposition and Homogeneity

As already mentioned in section 3.2.3 the scintillator is attached to the tip of the light pipe. This is accomplished by either directly depositing the powder onto the lucite itself, or indirectly by covering a substrate such as a thin glass cover which then is glued to the light pipe via some optical grease or high viscosity silicone oil. A uniform, thin coating of the powder is required for good quantum efficiency and therefore a technique needed to be developed that can be achieved in an easy, timely and inexpensive manner and simple enough so that even an unexperienced STXM user would be able to make and mount a scintillator.

4.5.1 Methods

In general, there are two different ways to produce scintillator screens, film coating and vapor deposition [40]. With film coatings, the most common way they are formed is by sedimentation. Nevertheless there are much more elaborated ways such as centrifugal settling, electrophoretic, spraying and sprinkling techniques [39]. In any case, phosphor powder scintillators, produced by settling processes, suffer intrinsically from incomplete substrate coverage particularly at low screen densities. A number of easy to handle methods have been gathered within this work and the protocols are quoted in appendix B.

One approach using gelatin as a binder to enhance the mechanical strength of the phosphor layer and which also results in a uniform distribution of the phosphor as seen by using a visible light microscope was reported by Comins *et al.* [1]. Their studies, using transmission electron microscopy concluded that a layer thickness at about 10 crystal layers for a P47 with a grain size distribution maximum at about 2.5 μm had the highest efficiency. They show additionally, that there is little influence on the light output for a binder content as 2 g m^{-2} to 1.6 g m^{-2} which corresponds to 0.05 wt% in aqueous solution. Optimizing the light output suggests the use of a screen density in the range $14-25$ g m^{-2}, where the signal to noise ratio has reached its plateau region. Of course, this method has to be adjusted for soft x rays and different grain sizes. The protocol by Comins *et al.* [1] works well for making efficient screens. For P31 as a different example, Knoll [26] recommends settling out the coarser grains from an aqueous solution with a 1.3 % gelatin concentration which turned out to be too high of a concentration for screens made in this study.

Another way of easy creation of phosphor screens based on an old protocol by Warnking *et al.* [2] uses water glass as a binder (sodium or potassium silicate $\bullet$ $9H_2O$). The whole idea relies on a settling-draining procedure where the substrate is situated in a solution of phosphor grains in distilled water and Na silicate. Rather than water, methyl alcohol or isopropyl suspensions could also be used [39]. The grains are allowed to settle down on to the substrate and the aqueous solution is carefully drained. This procedure can be repeated until the desired layer thickness and density is achieved. In contrast to gelatin, an organic binder, the amount of radiation damage will be much less severe for water glass. In order to avoid unwanted absorption completely, one merely could omit the binding agent.

The most simple almost trivial but for our purposes also most feasible technique relies on an idea by Tolek Tyliszczak, Lawrence Berkeley National Laboratory, California. A thin layer of optical grease is applied to the substrate, wiped off and dipped into the phosphor powder. After that the excess is removed by tapping. Beyond being a really simple way of creating a phosphor screen, high grain densities can be achieved by pressing the substrate into the powder. If the optical grease film was wiped of carefully, the homogeneity of the grain film will also be guaranteed to a certain extent. Beyond that, there are no further absorption features coming from any kind of additional binder. Doing point spectra experiments with a gelatin/P47 screen and then changing to the optical grease method instantly doubled the achieved count rates.

4.5.2 Grain Size and Detector Distance

Of course, for any powder of any grain size there will be an optimal method achieving an ideal density as well as the ideal thickness and homogeneity and the required stability within the whole scintillator screen. But are all these demands really needed for a single channel STXM detector?

Concerning thickness and density, this question has to be answered with "Yes", since the phosphor film must be thick and dense enough to enable a significant fraction of the incident x rays to interact and produce sufficient optical photons for detection.

But the uniformity of the screen is most important to achieve good spatial resolution which is mainly determined by screen parameters such as size, packing density, *etc.* of the constituent phosphor particles. For example, in the case of covering a whole CCD array [39], the uniformity of the phosphor film is highly important for the quality of the image [3].

Regardless of how efficient the illuminated screen area will be, this area will stay the exact same at all times since neither the x-ray beam nor the detector will move within a common stepper or piezo scan. Therefore, the footprint of the beam cone roughly should stay the same on the sensitive area.

Nevertheless, the scanned sample itself will include a phase landscape that refracts the x-ray cone by an angle Θ_r dependent on the phase gradient as

$$\Theta_r = \frac{1}{k}\frac{d\Phi}{dx} \tag{4.6}$$

where $\Phi = \delta k t$ is the total phase advance of the specimen relative to vacuum propagation, and $k = 2\pi/\lambda$ is the wave number [19].

This leads to a shift of the beam footprint (see figure 4.6) on the detector by an amount of $a \sim \Theta_r \cdot d$, where d is the distance from the focus to the detector. To determine the order of magnitude of such a shift which actually can be used for phase contrast microscopy, Benjamin Hornberger described in his PhD thesis a phase shifting sphere of 1.6 μm diameter (typical specimen size) with a maximum phase shift of 0.5 rad at its center and zero absorption. At the point where the sphere is curved 45°, the phase gradient can be calculated to $d\Phi/dx = 0.72\ \mu m^{-1}$. In the following we use this value as a typical phase

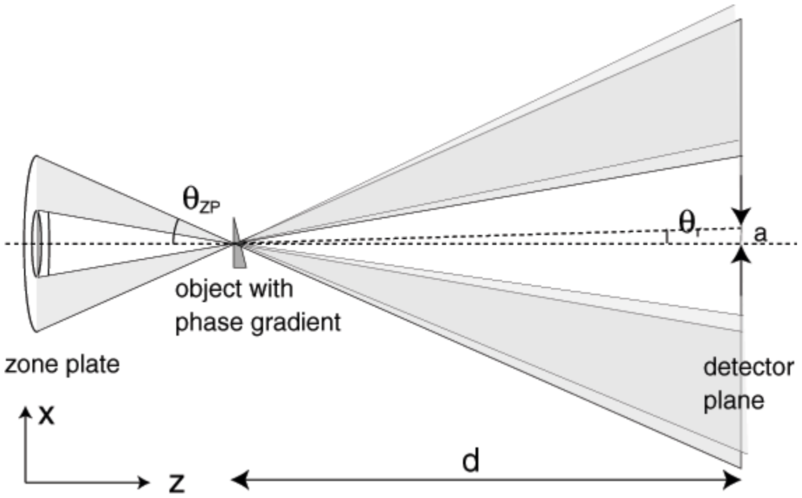

Figure 4.6: **Shift of the Beam Cone on the Detector.** We assume a zone plate optic with a central stop, as it is commonly used in scanning x-ray microscopy. (Image taken from Hornberger [19].)

gradient within a sample.

If we now assume the detector performance will not change within one scan if the beam footprint shift remains smaller then the average particle size of the scintillator grains, we can calculate a maximum distance of the detector to the specimen as

$$d_{\max} = \frac{2\pi\bar{a}}{1239.842\ eV\ nm} E\,[eV]\,\frac{1}{d\Phi/dx} \tag{4.7}$$

where E is the incident photon energy and $\bar{a}$ the average grain size of the phosphor. Beam shift behavior for different energies as well as the maximum operating distance of the detector is given for both phosphors, P43 as well as P47 in figure 4.7.

The right curve shows that an operating distance of not more than 1 cm is the best distance for optimal detector performance.

Of course the detector distance is also confined by the diameter of the light pipe. The zone plate creates a beam cone in such a way that its half opening angle is the numerical aperture

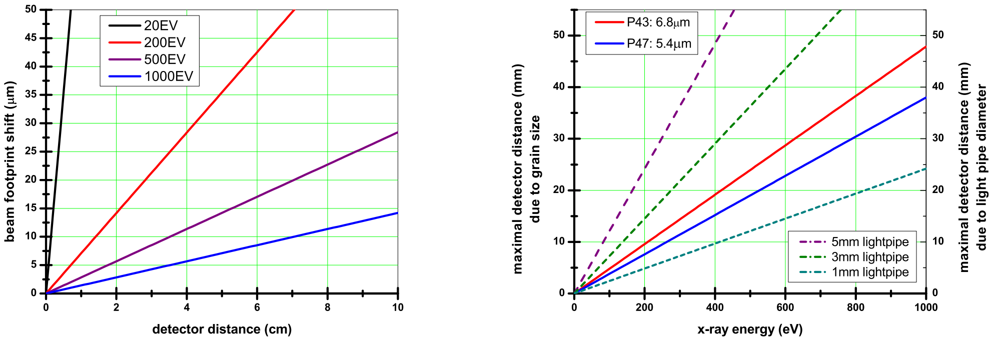

Figure 4.7: **Dependance of the Detector Distance on the Scintillator Grain Size for a Typical Phase Shift of $d\Phi/dx = 0.72\ \mu\mathrm{m}^{-1}$.**
The beam footprint shift for different energies (left).
The maximum detector distance for two different median diameters of grain sizes (solid lines) and three different light pipe diameters (dashed lines) (right).

$$NA = \Theta_{ZP} = \frac{\lambda}{2dr_N} \tag{4.8}$$

where dr_N is the outermost zone width of the zone plate (see figures 2.5 and 4.6). Using typical dr_N of 30 nm also defines a maximum detector distance dependant on the diameter of the light pipe and x-ray energy by following equation:

$$d_{\max} = \frac{\sigma dr_N}{1239.842\ eV\ nm} E\,[eV] \tag{4.9}$$

The dependencies for three different light pipe diameters σ to detector distance are shown in figure 4.7 as dashed curves on the right hand side. In order to distribute the x-ray signal homogeneously over as large an area of the scintillator as possible to achieve a broad illumination of the PMT photocathode, operation around these maximum values is desired as long as this does not conflict with the maximum distances given by the grain size restriction.

Chapter 5

The Spectrometer Setup

5.1 Purpose

Because an integrated luminescence signal can not be used to identify specific spectral lines in the UV/VIS/NIR regime, a spectrometer setup was installed in the microscope (see figure D.1). An attempt to identify spectral lines using another approach was not successful (see appendix A).

5.2 The Collimating Lens and the Fiber

For the collection and collimation of the luminescent light, an Ocean Optics 74-UV Collimating Lens was used. The $f/2$ fused silica lens is designed for a wavelength range of 200 to 2000 nm and attached to the detector stage. It directly couples to a fiber via a SMA905 connector and its small size (lens diameter without housing: 5 mm) makes it an appropriate solution for limited space inside the microscope chamber. The main advantage of a combined x-ray and VIS/NIR detector is discussed in section 5.4. From the focal point, beam divergence is approximately 2° or less, depending on the fiber diameter. To be more precise, the divergence of a beam focused using a single lens is $\tan a = d/f \sim 2.29°$ where $f = 10$ mm is the focal length of the lens and $d = 0.4$ mm is the aperture or in our case the fiber diameter.

A 400 μm core fiber couples the light out of the STXM chamber via a special fiber feed-through and into the spectrometer. The fiber transmission curve can be seen in figure 5.1.

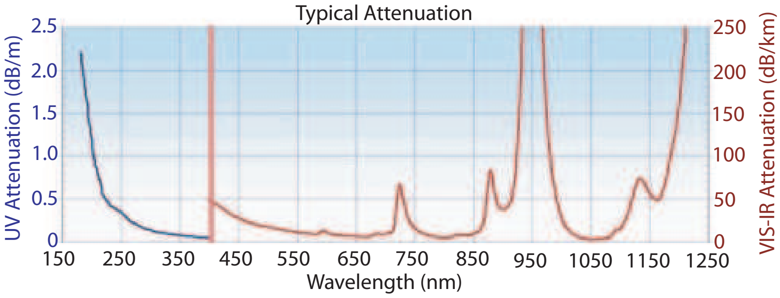

Figure 5.1: **Fiber Transmission Curve of the Luminescence Collecting Fiber.** The fiber is especially designed for the wavelength region between 250 and 700 nm. Beyond, attenuation gets significant. (Graph presented by courtesy of Brian Dewan, Photon Control Inc.)

5.3 The Photon Control SPM002-E Compact Spectrometer

5.3.1 General Properties

The spectrometer SPM002-E designed by Photon Control Inc., Canada, is based on a Czerny-Turner optical bench [46]. A schematic can be seen in figure 5.2. The light coming from the 400 μm core fiber (A) is focused onto an entrance slit (B) of 200 μm width and is further collimated by a curved mirror (C). The slit was customized for this size because a high light throughput is more crucial in our application then high resolution. The collimated beam is diffracted from a grating (D) and the dispersed beam re-focussed by a second mirror (E) to a linear CCD photochip (F). Each wavelength of light is focussed to a different pixel of the chip which can then be read out separately. According to this description, there are no moving parts which is a major advantage in contrast to former monochromators, which use a rotating grating to scan the desired wavelengths within one single detector. The grating that is used in the SPM-002-E has a groove density of 400 groves/mm and a blaze wavelength of 500 nm. A 70 mm focal length input (collimating) mirror and a 70 mm output (focusing mirror) gives a 1:1 imaging ratio. Thus, the 200 μm wide slit is imaged onto a 200 μm wide image on the CCD. Regarding the resolution,

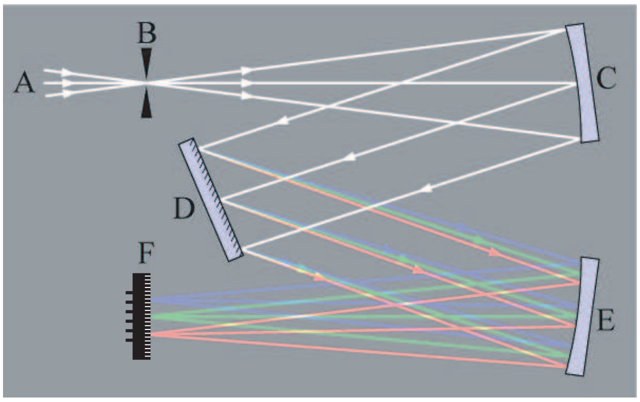

Figure 5.2: **Czerny-Turner Schematic.** The light coming from a fiber (A) is separated by a grating (D) into its spectral colors and mapped on a linear CCD array (F). (Image taken from WIKIPEDIA [37] and altered.)

the approximate wavelength resolution in nm/pixel is about 0.26 determined by the grating. The pixels on the Toshiba TCD1304 CCD used are 8 μm wide. Therefore, the 200 μm slit is imaged over $200/8 = 25$ pixels, the estimated resolution is therefore 25 pixel × 0.26 nm/pixel = 6.5nm. The grating is orientated in such a way that a spectral range from 200 to 1090 nm is obtained. Further crucial specifications are an integration time range from 10 μs to 65 s; data can be read out at a maximum refresh rate of 20 Hz.

5.3.2 The CCD Array

The CCD array is a Toshiba CCD linear image sensor TCD1304DG. The integrated circuit can be seen in figure 5.3 (left) next to its spectral response @ 25°C (right) [47].

The photo sensing region consists of 3648 8×200 μm^2 photodiodes of p-n type. For an UV enhancement, a special coating is applied.

5.3.3 Software and Remote Control Options

The software that comes with the spectrometer is SPECSOFT 2.3.1, which is a “user friendly” interface to the spectrometer operation. The whole concept is basically plug and play. The software provides basic data acquisition and

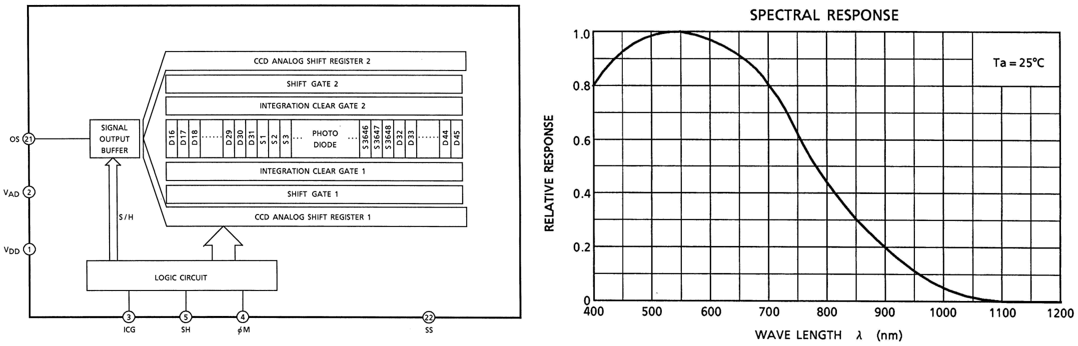

Figure 5.3: **The Linear Image Sensor TCD130DG.** (Images taken from the TCD130DG data sheet [47].)
The integrated circuit of the sensor (left). The charge generated at a linear array of photodiodes is integrated in two gates and shifted into a signal output buffer. This buffer is the interface to the outer logic circuit.
The relative spectral response curve of the sensor shows a broad maximum at about 550 nm, which makes the spectrometer especially feasible for measurements in the UV/VIS region (right).

display functions as well as more complicated evaluation procedures and trigger operation. The operation of the software itself is straight forward and mostly self explaining. A screen shot of the user interface is shown in figure 5.4.

More important for the integration of the spectrometer into STXM is a C++ development kit purchased with the spectrometer that allows application software to interface with SPM002 series spectrometer using a development library (DLL) directly [48]. The SPM002 DLL provides an access to control the SPM002 spectrometer's operation. The number of available functions is confined to 11 interface functions included in the DLL, which makes programming rather clear. The software developer can so concentrate on the operation functionality.

5.4 The Idea of Combined Detection

In principle, this spectrometer could be combined with the light pipe detector described in chapter 3 in such a way that scanning transmission x-ray

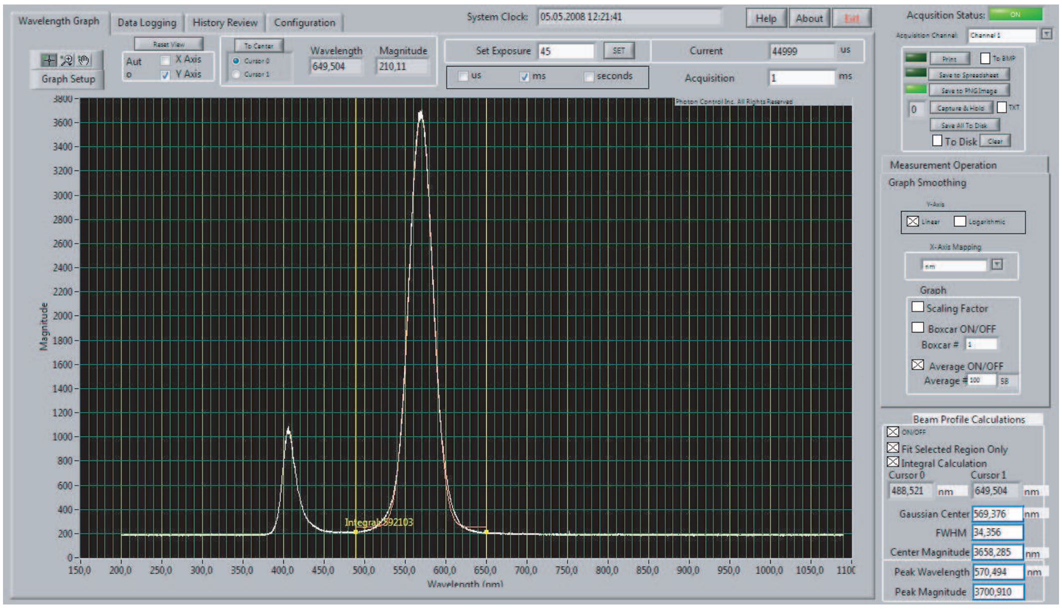

System Clock: 05.05.2008 12:21:41

Auto ☐ X Axis ☑ Y Axis

Wavelength 649,504 Magnitude 210,11

Set Exposure 45

☐ us ☑ ms ☐ seconds

Current 44999 us

Acquisition 1 ms

Acqusition Status: ON

Acquisition Channel: Channel 1

☐ To BMP

0 ☐ TXT

☐ To Disk

Y-Axis ☒ Linear ☐ Logarithmic

X-Axis Mapping nm

Graph

☐ Scaling Factor

☐ Boxcar ON/OFF

Boxcar # 1

☒ Average ON/OFF

Average # 100 58

☒ ON/OFF

☒ Fit Selected Region Only

☒ Integral Calculation

Cursor 0 Cursor 1

488,521 nm 649,504 nm

Gaussian Center 569,376 nm

FWHM 34,356

Center Magnitude 3658,285 nm

Peak Wavelength 570,494 nm

Peak Magnitude 3700,910

Figure 5.4: **Screen Shot of the SPECSOFT Software.** An UV light source (left peak) excites quantum dots in solution which luminesce at 569 nm (right peak). The signal is fitted Gaussian and the crucial values are displayed in the right bottom corner of the figure. 100 spectra were averaged with an exposure time of 45 ms respectively.

microscopy would be possible at the same time as scanning luminescence x-ray microscopy. Therefore, adequate implementation of the SPM002 into the STXM data acquisition environment would make it possible to obtain STXM data matched to a luminescence map. How the results of such an application could look like is shown in figure 5.5. Here, the spherical grating mirror (SGM) of the beam line was scanned continuously while the spectrometer collected spectra from P43 scintillator (see chapter 4.4.2). Since there was no communication between spectrometer and SGM, the energies are estimated by linear interpolation. A small IDL program called "read_spectra" converts and evaluates the spreadsheets delivered by the spectrometer.

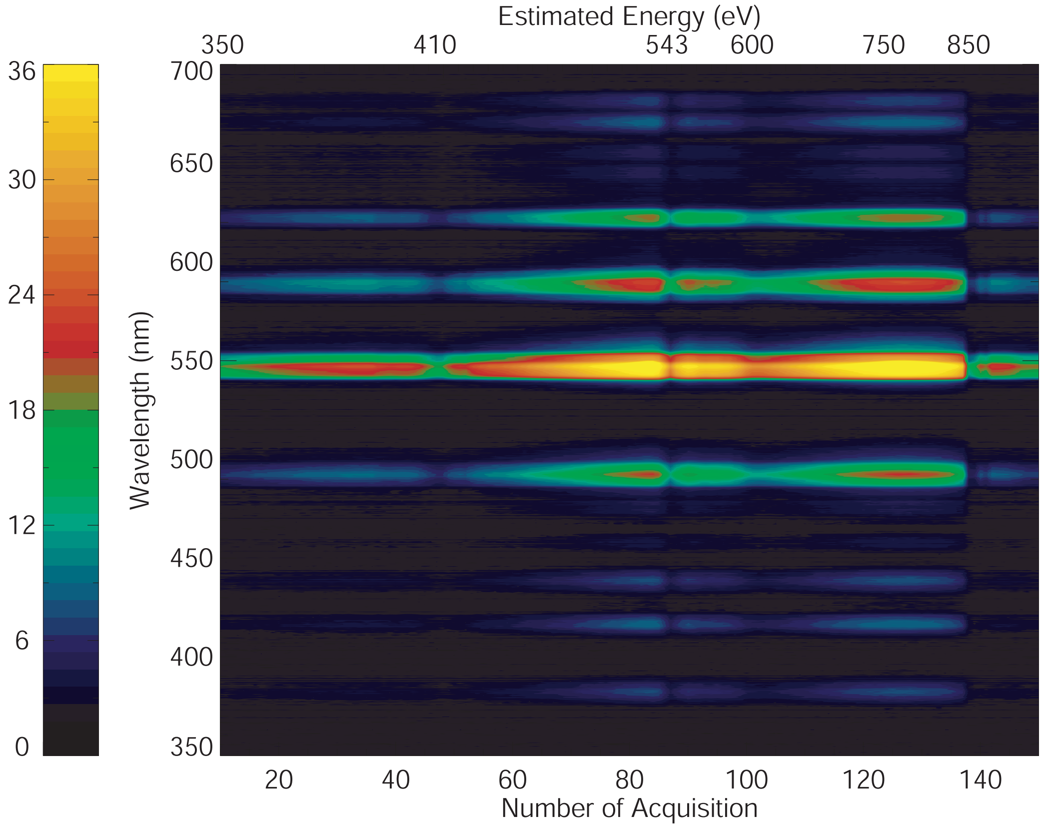

Figure 5.5: **Excitation Energy Dependant Scintillation of P43.** The luminescence spectra of P43 scintillator were taken over a broad range of x-ray excitation energies. The x-ray energy was scanned continuously but not necessary linearly since there was no communication between the spectrometer and the spherical grating mirror (SGM) of the beam line. Acquisition number therefore is the more reliable scale. The energies are retrieved by identification of the absorption lines of carbon, nitrogen and oxygen and other features. In future applications, the spectrometer could be feed back by the microscope. The luminescence signal is color coded and displayed logarithmic. The undulator flux profile at a gap size of 36 mm may be identified (see right part of figure 3.7).

Chapter 6

Quantum Dot Nanocrystals

6.1 The Concept of Quantum Dots

The term **quantum dot** (**qdot**) refers to a quasi zero dimensional electronic system with length scales near the Bohr radius, where the electronic structure is quantum confined [49]. This **quantum size effect** takes place where the size of the semiconductor becomes comparable to or smaller than the natural length scale of the electron or hole and therefore the carriers are confined by the boundaries of the material. This causes an atomic like optical behavior since valence and conduction bands become quantized into a ladder of hole and electron levels. In that sense, one is talking about 100 to 10000 atoms forming one particle, where the lower number is restricted by the stability of this cluster. The upper number on the other hand is bound to that size, where the separation of these atomic like energy states is so small that the charge carriers can move from one state to another by the thermal energy $k_BT \sim 25$ meV; in other words, when the length scale of the quantum confinement is surpassed and one observes bulk bands rather than separated states.

It is useful and common to classify quantum dots according to the magnitude of their confinement. As already mentioned, a helpful length scale to compare with is the Bohr radius:

$$a_B = \varepsilon \frac{m}{m^*} a_0 \tag{6.1}$$

with ε, the dielectric constant and $a_0 = 5.29 \times 10^{-11}$ m, the Bohr radius of the hydrogen atom. The variable m is the rest mass of the electron whereas m^* is the mass of the electron, the hole or the formed exciton, whichever is considered. Accordingly, there are three different Bohr radii that have to be taken into account, the electron a_e, the hole a_h and the exciton a_{exc}.

Using a to label the radius of the nanocrystal, one can define three different confinement regimes:

- $a < a_e, a_h, a_{\text{exc}}$ defines the **strong confinement regime**;
- if $a_h < a < a_e, a_{\text{exc}}$, one particle is strongly confined, but the other is not, this is referred to as the **intermediate confinement regime**, and;
- in the case where $a_e, a_h < a < a_{\text{exc}}$ the center of mass of the exciton, this is the **weak confinement regime**.

6.2 Electronic Structure of Quantum Dot Nanocrystals

The left part of figure 6.1 shows a simplified drawing of the electronic structure of an arbitrary quantum dot. Three parts of the system are indicated. The most important part of the structure is the photoluminescent semi-conducting core, covered by a shell of a different material and a higher band-gap. This might be a simple coating as ZnS for CdSe nanocrystals used for surface passivation. In terms of molecular beam epitaxy (MBE) generated confinement one might also think of a special designed two dimensional quantum well layer embedding the actual quantum dot (see chapter 6.3). The qdots are suspending in an embedding matrix. This can be a common organic solvent for nanocrystals or the MBE substrate.

For our considerations, a simple particle-in-a-sphere model should be sufficient to describe the quantum confinement that takes place within the core zone since we are at the moment not interested in quantitative prediction nor fine structure effects.

Solving the Schrödinger equation for an electron in a spherical potential well of radius a

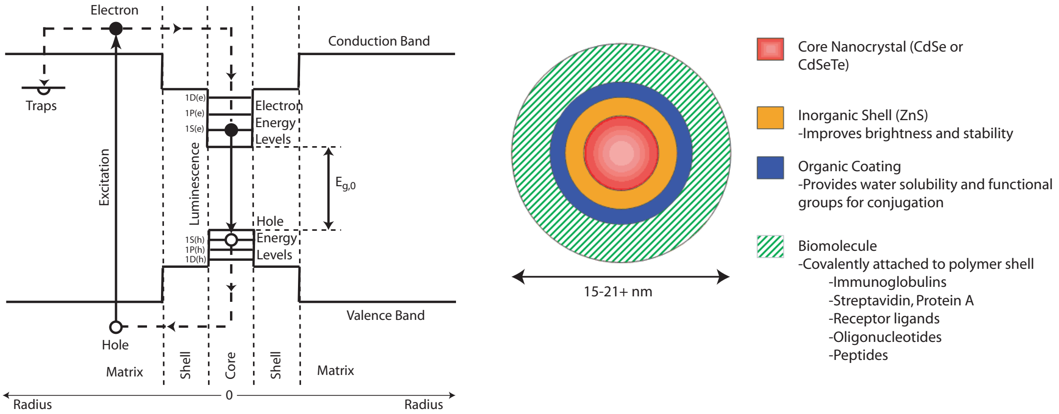

Figure 6.1: **Electronic Structure and Composition of Quantum Dots.** The electronic structure of a typical quantum dot environment (left). The substrate/matrix may be interfaced to the qdot by help of a two dimensional quantum well.
The composition of (CdSe)ZnS nanocrystal and their organic coating (right). (Image taken from Invitrogen Corp., General Information Brochure [6].)

$$V(r) = \begin{cases} 0 & r < a \\ \infty & r > a \end{cases} \tag{6.2}$$

yields a quantized energy level distribution of the form

$$E_{n,l} = \frac{\hbar^2 k_{n,l}^2}{2m_0} = \frac{\hbar^2 \alpha_{n,l}^2}{2m_0 a^2} \tag{6.3}$$

where $\alpha_{n,l}$ is the n^{th} zero of the l^{th} order spherical Bessel function, $k_{n,l} = \alpha_{n,l}/a$ and m_0 the mass of the particle captured in the well [49]. Due to the well known hydrogen like symmetry of this problem the *eigenfunctions* are simple atomic like orbitals which can be labeled by the quantum numbers $n = 1, 2, 3, ...$ and $l = \mathrm{s, p, d}, ...$

The energy level is proportional to $1/a^2$ and therefore strongly depends on the size of the sphere. The term “Artificial Atom” becomes understandable at this point since the atomic like energy levels of such an object can be designed by merely controlling its diameter.

More precisely, one can assume the effective mass approximation. More detailed calculations here approximate the following energy distribution of the conduction ($n = c$) and valence ($n = v$) bands as

$$E_k^c = \frac{\hbar^2 k^2}{2m_{\text{eff}}^c} + E_{\text{gap}} \tag{6.4}$$

$$E_k^v = -\frac{\hbar^2 k^2}{2m_{\text{eff}}^v} \tag{6.5}$$

where E_{gap} is the semiconductor band gap and the energies are relative to the top of the valence band. The charge carriers in this system behave as free particles with an effective mass, $m_{\text{eff}}^{c,v}$.

Graphically, the effective mass accounts for the curvature of the conduction and valence bands at $k = 0$. Physically, the effective mass attempts to incorporate the complicated periodic potential felt by the charge carriers in the lattice. Semiconductor atoms within the lattice are ignored; electrons and holes treated as free particles but with different mass.

This approximation reveals another characteristic of quantum confinement. The band gap energy of a bulk semiconductor is defined by the material. This is not true for a nanocrystal any more. Here, the gap energy is largely defined by the size of the particle. Luminescent transitions so can be precisely tuned to a desired emission wavelength.

6.3 Excursus: Quantum Dots and their Different Occurrences

As already mentioned in section 6.2, the term “quantum dot” implies significantly different kinds of material structures. Pertaining to this work we are basically interested in soluble quantum dot nanocrystals (QDNs) to use as biological labels. Beyond this chemical method of production, another very important group of quantum dots can be manufactured by molecular beam epitaxy (MBE). The main driving force for this research is the development of 1300 nm and 1550 nm diode lasers for fiber-telecommunication [50, 51]. Current basic research in this region focuses on GaAs based materials due to such advantages as low substrate cost and a higher conduction band offset that results in better temperature stability. Furthermore substrate compatibility with well developed GaAs/Al(Ga)As distributed Bragg reflectors makes GaAs attractive.

Since most characteristics of quantum confined semiconductors are, in principle, the same for different quantum systems, some basic properties of such systems, identified during a research project conducted in collaboration with Dirk Bisping from the Lehrstuhl für Technische Physik, Würzburg, in 2007, shall be discussed. Here, luminescence characteristics of so called "dot-in-a-well" structures were tested. Such two dimensional quantum well structures are generally limited to material pairs that are well lattice matched due to the limited strain tolerance of such planar systems. Quantum dot/quantum well nanocrystal structures with this characteristic have been already successfully synthesized such as ZnS(CdSe)ZnS where lattice mismatches up to 12 % can be handled without any problems [49].

During our research we investigated InAsN quantum dots that were embedded asymmetrically in a two dimensional GaInNAs quantum well by means of solid source MBE. The Indium content of the quantum well layer was approximately 17 %. A scanning electron microscope (SEM) image of the structure can be seen in figure 6.2 on the right hand side. On the left side of the figure, a transmission electron micrograph (TEM) of the quantum dot nanocrystals as used throughout this paper are shown for comparison.

The luminescence yield of InAsN quantum dots were tested with regards to their temperature and excitation power response using a similar setup as shown in figure A.1. The outcome of these experiments is rather exciting (see figure 6.3).

From the figure one can see that the photoluminescence (PL) intensity decreases rapidly for temperatures higher than 70 K. This is mainly caused by thermal escape of carriers out of quantum dot states but also by the presence of non radiative recombination centers at higher temperatures. In connection to this decrease in intensity, a distinct red shift of peak position can be seen on the left hand side of the figure.

The right hand side of the figure shows the luminescence at several excitation powers. "k.F." indicates that no filter was used, then, filtering increases with increasing filter classification number "015" to "100" and excitation power decreases respectively. The ratio of the left and right peak intensities decreases with decreasing excitation power. This gives reason to assume an excited

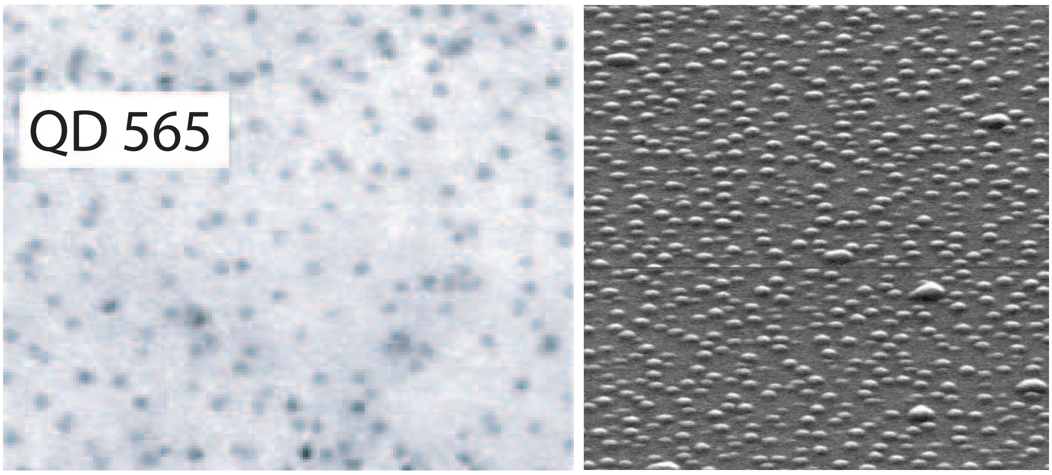

Figure 6.2: **Electron Micrographs of Quantumdots in Different Contexts.**
TEM of core-shell (CdSe)ZnS nanocrystals (left). Image provided by Mark Ellisman, National Center for Microscopy and Imaging Research, UCSD, San Diego, California and taken from [6].
SEM of MBE grown dot-in-a-well structure of InAsN$_{0.5\%}$ QDs embedded asymmetrically in a GaIn$_{17\%}$N$_{0.2\%}$As QW (right). array: 600 × 1750 nm, viewing angle: 20°, size of QDs is mainly constant with a homogeneous distribution. Image provided by Dirk Bisping, Würzburg, 2007.

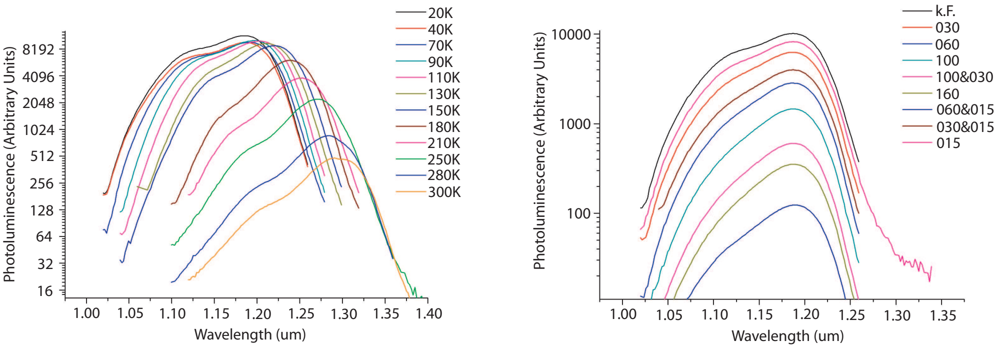

Figure 6.3: **Temperature- and Excitation Power Dependant Quantum Yield of MBE generated Quantum Dots.**

The quantum yield of the qdots at different temperatures (left). Low temperatures prohibit thermal escape of carriers out of quantum dot states and diminish the presence of non radiative recombination centers.

The luminescence spectra at different excitation powers reveal the characteristics of the qdots (right). In this case, lowering the excitation power leads to the left peak decreasing more than the right peak. This reveals the decay from an higher excited quantum dot state. In the other case where both peaks would decrease simultaneously, one would expect two different categories of qdot sizes resulting in two independent emission lines.

quantum dot state for the left peak that cannot decay radiation less at high powers since the lower energy states will always be occupied due to the finite life times. When illumination gets less, there will be no overflow any more and luminescence will emerge primarily from the lower energy state. Hence, the double peak structure emerges from luminescence coming from a higher energy state as *e.g.* 1P(e) in addition to 1S(e) (see figure 6.1).

What was learned from this research project on MBE quantum dot physics is the following. First, in the case of high flux synchrotron radiation, one cannot necessarily expect the sharp emission peaks that are obtained from VIS light microscopy. If high excitation flux is able to saturate the lowest excited state, higher excited states will become active from which luminescence will be possible. The emission peaks become broader or even split. Second, for absorption in the soft x-ray range, the quantum yield most likely will be much more efficient at low temperatures. Even though Invitrogen Corp. [6] claims that "fluorescence is not temperature dependent" for (CdSe)ZnS nanocrystals where they recommend their product to be stable at temperatures above 4°C due to stability and aggregation effects at the same time, quantum dot labeling might have cryogenic applications. Especially in organic samples that are treated with low concentrated quantum dot solution, shock freezing techniques might prevent aggregation at low temperatures of the nanocrystals and yield good labeling properties. These speculations ask for further investigation though.

6.4 Chemical Synthesis of (CdSe)ZnS Quantum Dots

A very elaborate description of the most successful synthesis in terms of quality and monodispersity of nanocrystals was done by Klimov *et al.* [49]. Here, the very basics shall be described for a better overview and understanding of the quantum dot concept.

Very successful in terms of the crystal quality and mono dispersity turns out to be the pyrolysis of metal-organic precursors in hot coordinating solvents at about 120 to 360°C. A temporally discrete nucleation event followed by relatively rapid growth from solution-phase monomers is followed by a slower growth, the so called Ostwald ripening, which implies a recrystallization and aging process (see figure 6.4).

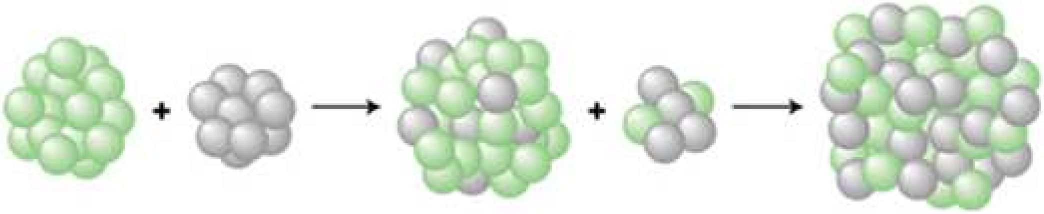

Figure 6.4: **Schematic of the Ostwald Ripening Process.** A dynamic on- and off going process reorders the elements of different clusters finally resulting in the end product. (Image taken from Bowker *et al.* [52].)

The nucleation is achieved by quick injection of a precursor into hot coordinating solvents. This results in a thermal decomposition of the precursor reagents and supersaturation of the formed monomers that are partially relieved by particle generation. Growth then proceeds by the addition of monomers from solution to the nanocrystal quantum dot nuclei. The monomer concentrations are kept below the critical concentration for nucleation. Thus, these species only add to existing particles, rather than forming new nuclei. Once the monomer concentrations are sufficiently depleted, growth can proceed by Ostwald ripening. Here, sacrificial dissolution of smaller (higher surface energy) particles results in growth of larger particles and, thereby, fewer particles in the whole system. Of course, there are many elaborate alternative methods nowadays.

Crucial aspects for the colloidal synthesis are particle size and size dispersion. Both are mainly controlled by time and temperature. After the reaction, there is still the possibility to sort the smaller particles from the larger ones by centrifugation. In terms of crystal quality, the dynamic behavior of the nucleation process is the most important parameter. Atoms going on and off the nucleus create a steady rearrangement that will improve lattice quality in the long term.

The quantum dot nanocrystals as we use them here are bond to ligands. Mostly in use are alkylphosphines, alkylphosphine oxides, alkylamines, alkylphosphates, *etc.* of various alkyl chain lengths and degrees of branching. The polar head group coordinates to the surface of the particle and the hydrophobic tail is exposed to the external solvent also called the matrix. Hence, nano particles are commonly soluble in non polar solvents as in our case decane. Moreover, ligands hinder aggregation of individual nanocrystals by shielding the van der Waals forces. Aggregation would lead to flocculation as shown later on in this chapter.

In order to reach higher quantum yields, the nano particles nowadays are usually passivated as in the case of CdSe with an epitaxial layer of ZnS. Without this coating, unsaturated dangling bonds on the surface of the crystal would act as surface traps for charge carriers. This causes recombination of trapped carriers which leads to so called “deep trap” emission bands on the low energy side of the “band-edge” photoluminescence which is associated with the recombination of carriers within the interior quantized states. Beyond that, confinement of electrons and holes to the particle core is enhanced by such a coating where the band gap of the shell material is larger than that of the core material as in the case of (CdSe)ZnS. An advantage of nanocrystal overcoating in contrast to flat heterostructures is, that much bigger lattice mismatches can be tolerated. For (CdSe)ZnS *e.g.* there is a 12 % difference [53]. The surface of the object can control the spectral shape, position and dynamics of the crystal. This can be exploited to bind the particles to many kinds of different molecules and use them for example as biological markers. Labeling two different types of proteins with two sizes of qdots emitting at two different wavelengths would allow co-localization studies.

6.5 Properties of (CdSe)ZnS Quantum Dots

CdSe as a nano particle material is a direct gap semiconductor that is easy to handle and has been studied excessively as a model system [49]. As a standard, one nowadays can achieve very high crystallinity, adequate surface passivation, solubility and good size monodispersity (about $\sigma \leq 5\%$ which corresponds to about one lattice constant) which makes them feasible for optical spectroscopy purposes. Beyond that, its exciton Bohr radius of about $a_{\text{exc}} \sim 6$ nm classifies it into the intermediate to strong confinement regime for typical particle radii of 5 nm.

The combination of TEM imaging and comparisons of experimental and simulated x-ray diffraction spectra provides a self-consistent description of crystallite structures as observed in these nanoparticles. Even for very small crystallites containing as few as 275 atoms (which corresponds to a diameter of about 20 Å), average bulk bond lengths and a predominantly hexagonal (wurtzite) crystal structure are found for CdSe [53].

For the chemical synthesis of CdSe quantum dots, one predominantly uses cadmium precursors including alkyl cadmium compounds (*e.g.* dimethylcadmium) and cadmium salts (*e.g.* cadmium acetate or cadmium oxide) combined with a selenium precursor prepared simply from Se powder dissolved in trioctylphosphine (TOP). As surfactant-solvent a combination of trioctylphosphine oxide (TOPO) and some phosphonic acids to mimic impurities are utilized [49].

As already mentioned, the CdSe core is not stable alone and is very reactive. It can collect counter ions and other impurities and will no longer fluoresce. Therefore it is protected by a ZnS shell that also increases the quantum yield. In this conformation it is still water-insoluble. In order to realize solubility in a polar media, sometimes an amphiphilic polymer (inner portion hydrophobic, outer portion hydrophilic, bound non-covalently to the shell) is provided to make the nanocrystal water-soluble and provide sites for conjugation. However the quantum dots that we use are not soluble in water but come in a decane matrix.

As can be seen in figure 6.5, CdSe quantum dots do have a broad absorption spectrum including a large Stokes Shift (see chapter 4.2). The luminescence spectra of the right part of the graphic were obtained by averaging over 200 spectra of 20 ms exposure time in the case of 532 nm excitation and over 100 spectra of 45 ms exposure time in the case of 407 nm excitation. The background was subtracted and spectra normalized to equal size of the emission peaks. The excitation peaks are coming from reflections of the experimental setup and therefore are not comparable to the emission intensity. The two different exciting light sources yield qualitatively identical narrow Gaussian peaks at the same mean wavelength and dispersion. The peaks are Gaussian rather than Lorentzian due to the size dispersion of the nano particles in the 1.0 ± 0.1 μMol solution. Even though all the flux of the 0.2 W - 532 nm - laser was incident on the sample, double peaks cannot be observed within a 6.5 nm resolution (see chapter 5.3.1). Obviously there is no photoluminescence from excited states. Even after longer exposure, quantum dots prove excellent photostability.

6.6 CdSe Quantum Dots and X-rays

The majority of the research to date using x rays to analyze quantum dot nanocrystals has involved small angle x-ray scattering (SAXS) techniques to characterize quantum dot structures. In general, the angular dependence of

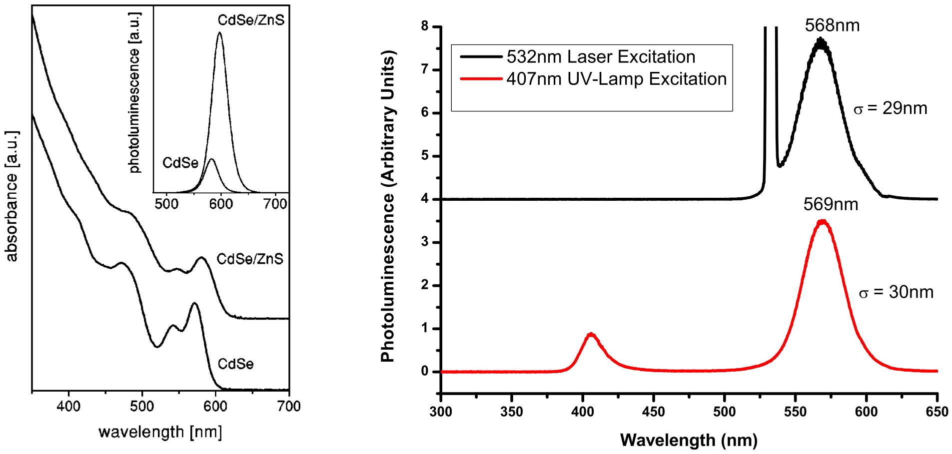

Figure 6.5: **Luminescence Characteristics of (CdSe)ZnS Nanocrystals.** The qualitative absorption and emission characteristics of (CdSe)ZnS qdots in contrast to uncapped CdSe qdots (left). A broad Stokes shift can be seen. (Image taken from Borchert *et al.* [54].)
The quantum dot emission with regards to UV and VIS excitation (right). Single Gaussian peaks even with high flux illumination were obtained (532 nm laser directly penetrated the sample). → No emission from higher excited states can be seen.

Groups	Material	Band Gap Energy @ 300K
II-VI	ZnO	3.35 eV
	CdSe	1.73 eV
	ZnS	3.6 eV
III-V	GaAs	1.43 eV

Table 6.1: **Band Gap of some Direct Semiconductors Discussed in this Work.** (Data taken from Streetman *et al.* [55].)

time averaged scattered radiation from the sample is measured and so an electron density map which represents the structure of the sample can be obtained.

In our case we are interested in the luminescence behavior of quantum dot nano particles using soft x rays. There are very few efficient biological labels that fluoresce when exposed to soft x rays. If quantum dots are an efficient label using soft x rays this would open a new area of research. The fundamental question we asked is "Will there be any luminescence at the characteristic wavelength and if yes, will radiation damage due to core level electron ionization affect the luminescence yield of the confinement system or not?" (cp. the band gap of CdSe in table 6.1 with typical soft x-ray energies). Are quantum dot nanocrystals feasible as efficient labels within soft x-ray excitation?

The manufacturer of the Qdot 565 nanocrystals, Invitrogen Corporation, clearly states that "...high energy radiation (such as x rays) will destroy Qdot nanocrystals..." and that the "...core structure will be fractured/disrupted by exposure to high energy..." [6]. In the same publication it is also argued that "...quantum dots can be excited by any wavelength below their emission peak, the lower the excitation wavelength, the higher the extinction coefficient, and they are brighter..." which probably takes UV excitation beyond the ionizing limit into account. However, the extent of these effects remains unclear and was not studied in detail according to the company. Thus we will discuss these statements in more detail.

6.6.1 Absorption and Conversion of Radiation in Scintillators

The absorption and scattering of x rays has been discussed in great detail in many papers and books [56]. But Birks [30] presents ideas about the actual mechanism, when it comes to scintillators, and unfortunately gives very pessimistic reasons why (CdSe)ZnS Nanocrystals might not be useful as luminescent markers in soft x-ray microscopy.

In general, the absorption of electromagnetic radiation is a single event procedure rather than continuous. Three well known effects are the Compton, the photoelectric and the pair production effects which describe the attenuation of the incident radiation. At soft x-ray energies, the photoelectric absorption is the dominant mechanism [57].

The total fraction of incident photons that will undergo one of these three effects can be written as

$$f = 1 - e^{-\mu d} \tag{6.6}$$

where μ is called the absolute linear attenuation coefficient. It consists of the Compton linear attenuation coefficient σ, the photoelectric linear attenuation coefficient τ which dominates at low energies and the pair production linear attenuation coefficient χ:

$$\mu = \sigma + \tau + \chi \tag{6.7}$$

For an absorber like a scintillator, the mass attenuation coefficient

$$\frac{\mu}{\rho} = \frac{N_A}{A} a_\mu \tag{6.8}$$

is independent of the physical state and density of the material and therefore serves as a better measure.

Here $a_\mu = a_\sigma + a_\tau + a_\chi$ is the total atomic cross section, N_A is Avogadro's number and A the atomic weight.

For a compound material one can simply add the mass attenuation coefficient of the different components i weighted by their fraction w_i

$$\frac{\mu}{\rho} = \sum_i \frac{\mu_i}{\rho_i} w_i \tag{6.9}$$

Using this formula, we can obtain the attenuation components for the three crucial compounds in cadmium selenide nanochristals: the core material CdSe, the shell ZnS and the solvent decane. Here we make use of the "Henke data collection" [32, 33]. The curves can be seen in figure 6.6.

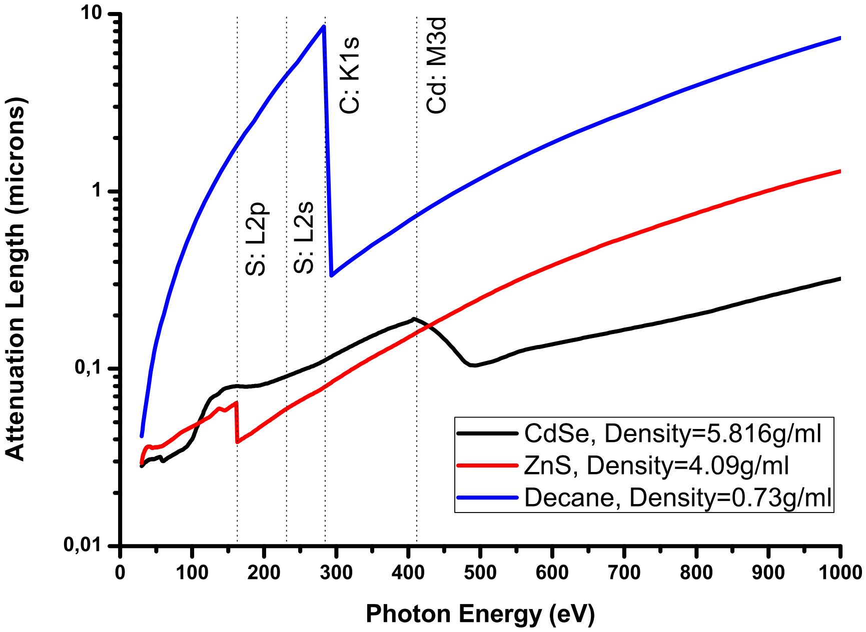

Figure 6.6: **Attenuation Lengths of the (CdSe)ZnS Elements.** The overall absorption of CdSe in contrast to ZnS quantitatively does not differ significantly. The absorption is mainly based on photoabsorption. (Data taken from Henke *et al.* [32, 33].)

Easily inferred from the graph is, that especially above 500 eV, attenuation of the CdSe and the ZnS absorption are quite similar in terms of magnitude. The absorption of incident energy there will be higher for CdSe and there are no important absorption features due to the photoelectric effect in this region. Why should CdSe therefore not be able to absorb enough energy for conversion to luminescent light as we have seen, for example for zinc sulfide (P31: see chapter 4.4.1)?

The crucial aspect relies on particle size. If a photon of relatively high energy E hits the scintillator material, it will generate secondary electrons, most likely within the core levels of the atoms. These electrons may have energies T from

Element	K1s	L$_{\mathrm{I}}$2s	L$_{\mathrm{II}}$2p$_{1/2}$	L$_{\mathrm{III}}$2p$_{3/2}$	M$_{\mathrm{I}}$3s
^{48}Cd	26711	4018	3727	3538	772.0
^{34}Se	12658	1652.0	1474.3	1433.9	229.6
^{30}Zn	9659	1196.2	1044.9	1021.8	139.8
^{16}S	2472	2309	163.6	162.5	
Element	M$_{\mathrm{II}}$3p$_{1/2}$	M$_{\mathrm{III}}$3p$_{3/2}$	M$_{\mathrm{IV}}$3d$_{3/2}$	M$_{\mathrm{V}}$3d$_{5/2}$	N$_{\mathrm{I}}$4s
^{48}Cd	652.6	618.4	411.9	405.2	109.8
^{34}Se	166.5	160.7	55.5	54.6	
^{30}Zn	91.4	88.6	10.2	10.1	
Element	N$_{\mathrm{II}}$4p$_{1/2}$	N$_{\mathrm{III}}$4p$_{3/2}$	N$_{\mathrm{IV}}$4d$_{3/2}$	N$_{\mathrm{V}}$4d$_{5/2}$	
^{48}Cd	63.9	63.9	11.7	10.7	

Table 6.2: **Absorption Edges of Cd, Se, Zn and S in** [eV]**.** Energies beyond 1000 eV are marked in red. The only element having more effective L absorption in the soft x-ray range is sulfur. For Cd and Se, M shell absorption plays a much more significant role. Hence, core level ionization will basically result in Auger decay rather than fluorescence (fluorescence yield below 1 %). (Data taken from the X-ray Data Booklet [58].)

0 to $T_{cm} = E/(1 + m_0c^2/2E)$ resulting from the Compton effect, $T_p = E - B_e$ resulting from the photo electric effect or $T_{pp} = E - 2m_0c^2$ resulting from the pair production effect. As already discussed earlier in this section, Compton and pair production effect can be neglected in comparison to photoelectron production at soft x-ray energies.

For an efficient scintillation, these electrons must distribute their energy within as much volume of the particle as possible, before they leave the material. The particles have to be big enough to yield convertible absorption!

In the primary photoelectric absorption process, the transition probability per unit time P_{if} from the initial state $|i\rangle$ to a final state $|f\rangle$ driven by a harmonic time-dependent perturbation $V(t) = V_0e^{-i\omega t}$ according to Fermi's rule is:

$$P_{if} = \frac{2\pi}{\hbar} \left|\langle f|V_0|i\rangle\right|^2 \zeta_f(E) \tag{6.10}$$

where $\zeta_f(E)$ is the density of final states.

The residual energy that was not transferred to electrons is in the soft x-ray range and M shell absorption typically used for Auger electrons [59]. A secondary process involves the radiative decay of a valence electron into the core hole, x-ray fluorescence (fluorescence yields below 1 %); photons of reduced energies B_e are created. Usually, these photons will have a higher probability of being absorbed than the primary photons. Therefore, the further the chain reaction goes throughout the scintillator, the less secondary photons will escape and the more of their energy actually will be converted into electron energy. Like the primary ones, these electrons will distribute their energy within the scintillator material. By a whole sequence of such multiple interaction the energy E of the incident photon may be completely converted into electron energy which contributes to the scintillation process.

In P31 - ZnS:Cu, particle sizes are on the order of 5 μm. This value is substantially above the corresponding attenuation length of ZnS and therefore, the overall yield of primary and secondary electrons will be high and have a huge volume to make electron hole pair production around the band gap possible. The (CdSe)ZnS nanoparticles with diameters on the order of 5 nm on the other hand are significantly beyond the attenuation length of CdSe. For the few photons and electrons generated in a primary interaction, there will be hardly any space to distribute their energy and hence, luminescence will be absent.

One might still think of the case where primary electrons liberated within the matrix/solvent (as in our case decane) followed by lower energy secondary electrons might serve as an energy distributor for the quantum dots. The total energy of this sequence of interactions is deposited within a range of 5 to 20 nm for $<$ 500 eV soft x-ray illumination [4]. Hence visible light emission should be well localized if this mechanism was responsible. The energy transfer to the quantum dots might be not high enough, though.

Where the absence of x-ray energy dissipation in nanocrystals becomes most obvious is with X-ray Photoelectron Spectroscopy (XPS). This is a method for surface structure studies that has successfully been applied to investigate the bonds between the CdSe and CdSe/ZnS core-shell nanocrystal surface and its trioctylphosphine/trioctylphosphine oxide and hexadecylaminena passivating ligands [54, 60]. Here, the quantum dots are illuminated by soft x rays while the kinetic energy and number of escaping electrons from the top 1 to 10 nm of the material are analyzed. Tuning the incident energy allows to vary the sampling depth. The idea is that generated photoelectrons created within the material will lose energy during their escape due to inelastic scattering. The electron mean free path thereby depends on the electron kinetic energy. In the soft x-ray regime, this value usually takes on values from about 5 to

25 Å reaching its minimum at 50 eV [59] depending on the actual valence electron density and electron cross section in the material. Hence, tuning the incident x-ray energy tunes different depths of the examined sample. In a volume sensitive XPS spectrum one therefore observes a peak broadening which is absent using surface sensitive x-ray energies. This broadening reflects the magnitude of energy loss of the electrons on their way out of the sample. Borchert *et al.* [54] worked with (CdSe)ZnS particles of 5.52 nm with a 7 % standard deviation, the ZnS shell was 0.64 nm and the ligand capping 1.63 nm. These parameters are essentially the same as the parameters for the qdots that we use in this thesis. In their studies, Borchert *et al.* directly observed a shift of the fitted Lorenzians widths from 0.18 to 0.29 eV for the Se 3d level using soft x-ray energies and even smaller broadening for the Cd 3d level (see table 6.2). The magnitude of this shift sets an upper boundary for energy that can be used to create electron hole pairs leading to luminescence. This value is far beyond the band gap of CdSe of 1.73 eV [55].

One can not exclude luminescence effects of (CdSe)ZnS nanoparticles completely. The huge volume difference of these nanocrystals in comparison to common scintillators like ZnS gives the rather pessimistic expectation of a quantum yield that is of the order of 10^3 to 10^9 less than these phosphors.

6.6.2 Experiment

General Issues concerning the Toxicity of Quantum Dots

Preparing quantum dot samples at the NSLS at Brookhaven National Laboratory is not unobjectionable. The lack of knowledge concerning the toxic impact of these nano structures give reason to raise the safety concerns. These include the use of a special laboratory as well as waste management and labeling infrastructure. Examination of unsealed samples therefore has become a general issue in recent years. Although cadmium and selenium are known to be toxic, there has been no toxicity known so far with intact nanocrystals at the recommended working concentration [6]. Most of the cell and animal experiments showed that when correctly capped by both ZnS and hydrophilic shells, no obvious CdSe nanocrystal toxicity was observed under normal experimental conditions [5]. On the other hand, cytotoxicity was observed when Cd^{2+} or Se^{2+} ions were released especially when the nano particle surface coating was not stable, exposing the CdSe to oxidization by air or UV damage.

Dried out Quantum Dots

Although it is mentioned in the literature that nanocrystals that are dried by air exhibit decreasing or even complete loss of luminescence signal over time [6], the first approach of sample preparation was similar to what is recommended by Borchert *et al.* [54].

The CdSe nanocrystals were washed removing an excess of stabilizing agents by use of ethanol and deposited on a cover glass substrate allowing the solvent to evaporate (see appendix B.5). These slides then where put into the inboard STXM with the qdots facing the x-ray beam. The chamber was pumped down to about 2.3 mtorr and refilled with helium to about 630 torr. According to Niederdraenk *et al.* [61], such a helium atmosphere also reduces radiation damage in the sample at least at a photon energy of about 9645 eV.

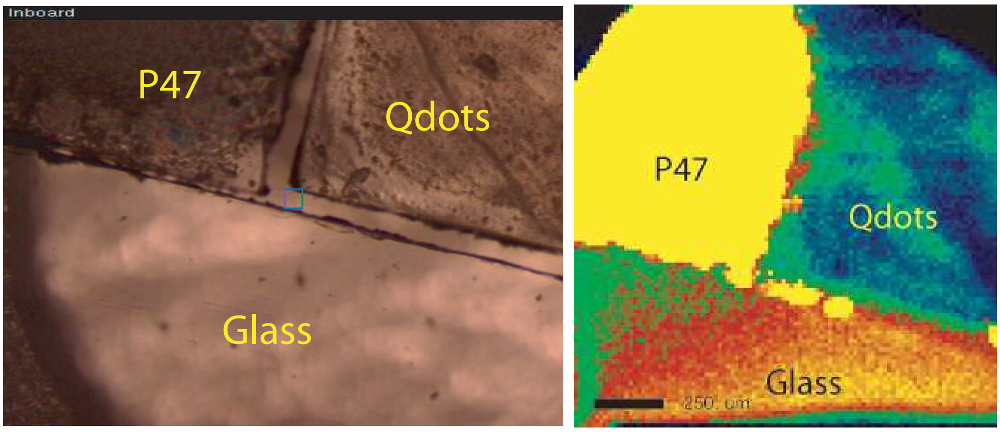

Figure 6.7: **Fluorescence from Dry (CdSe)ZnS Nanoparticles.**
A visible light microscope image indicates three different zones (left): P47 on glass, nanoparticles on glass and pure glass.
$600 \times 600\ \mu m^2$ Stepper Scan of the same sample at 400 eV excitation energy (right). Absorption of glass fluorescence is observed rather than luminescence.

The images in 6.7 show the results of the experiments. To avoid mixing of the P47 with the qdots, three different glass covers where prepared, one with Phosphor P47, one with quantum dots and one that was clear. To avoid mutual contamination, these samples were put together just before being placed into the microscope. The small gap between the glasses can be seen in figure 6.7. Although the preparation protocols where varied, no luminescence was observed. The same is valid for unwashed quantum dots in decane that where dried out. At this point, it is still most likely that quantum confinement was lost due to the presence of oxygen in the drying process and the destabilization through the washing process. Excitation of the samples with visible light also didn't yield any results.

Quantum Dots in Solution

The lack of control over what happens to the qdots during drying necessarily leads to the approach to test them in their natural context; (CdSe)ZnS nanocrystals in decane solution. Here, sample preparation turns out to be complicated since on the one hand qdots have to be kept in a sealed container to prevent them from drying out and being exposed to oxygen, and on the other hand the x rays have to be able to penetrate the sample. A modification of a "wet-cell" proved to be very promising.

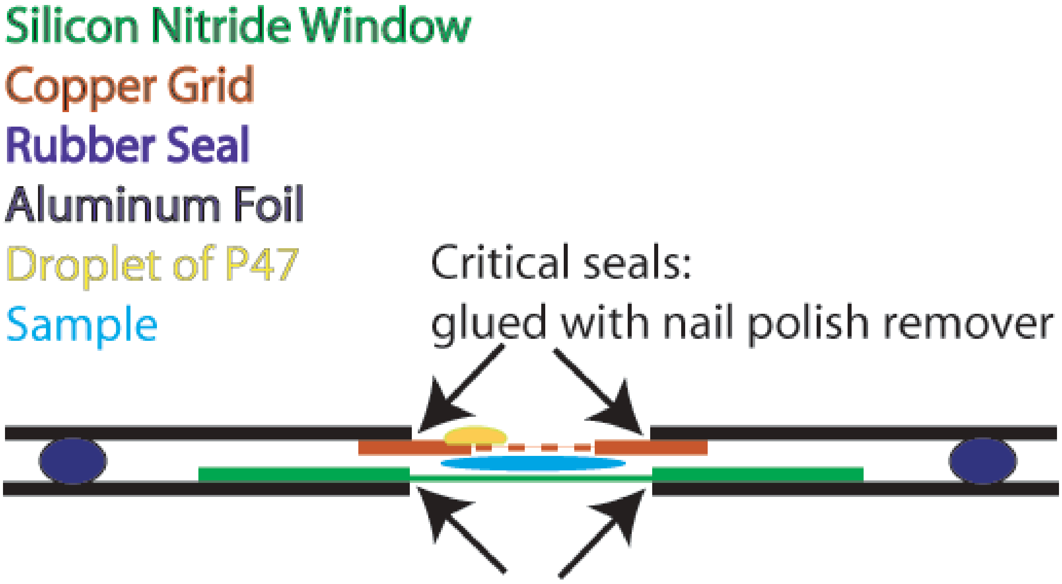

Figure 6.8: **A Modified Wet Cell to Study the Luminescence of (CdSe)ZnS Nanocrystals in Decane Solution.** The copper grid with 100 nm thick silicon monoxide windows was chosen due to better stability. The silicon nitride window was used in order to minimize fluorescence (as for example from a glass cover). A P47 droplet is provided as a reference signal.

As shown in figure 6.8, the sample is kept in between a sandwich of a 100 nm silicon nitride window and a copper grid with 100 nm thick silicon monoxide windows. The first was chosen in order to avoid any fluorescence that might result from a glass substrate. The latter turned out to be much more stable then another silicon nitride window. Especially in the case where the P47/gelatin droplet dried out, the silicon nitride window tended to break due to surface tension and adhesion of the droplet. The scintillator is provided as a reference signal I_0 and was also useful for focusing. By careful disposition of the droplet on the wet cell, very sharp boundaries can be achieved and used as orientation.

In order to compare with any background noise, the wet cell was measured first without and then with the quantum dot solution at excitation energies from 460 to 600 eV. Stepper scans of 1×2.4 mm^2 with a resolution of 20 μm were made for the blank sample, and stepper scans of 1.875×0.625 mm^2 with a resolution of 25 μm were chosen for the sample containing wet cell. Exemplary images of the empty and the filled wet cell can be seen in figure 6.9. The very left and the middle image are the same, but scaled differently. In the left one one can see the residual autofluorescence of the microscope objective resulting in a visualization of the copper grid structure. The middle and right hand images show the empty and filled containers respectively. Due to mechanical impact and chemical deterioration by decane, the boundaries of the P47 droplet slighly changed. The I/I_0 functions were calculated from regions of sample/qdots for I and P47 for I_0 for both STACKs respectively as described in the last bullet of chapter 2.2. To get the qdot response with respect to the incident x-ray flux rather the P47 signal, the quantum yield of P47 which goes as $E^{0.64}$ (see chapter 4.4.3) was taken into account. Both spectra are compared in figure 6.10.

Figure 6.10 implies that there is indeed some luminescence coming from the quantum dots, especially if one thinks of the PMT detector showing a ~ 6 times higher sensitivity for the P47 emission wavelength of 400 nm than for the expected luminescence wavelength of 569 nm for the qdots. (figure 3.3) Also, there is the possibility that the decane from the qdot solution mixed with the P47 and spread it all over the wet cell, although this was not observed visually. In addition, it turned out that the silicon monoxide windows embedded in the copper grid tend to break partially. The lack of knowledge about the actual composition of the emitted light spectrum so demands more elaborate techniques. The PMT-detector in combination with the microscope objective cannot answer this question whether qdots luminesce when exposed to soft x rays.

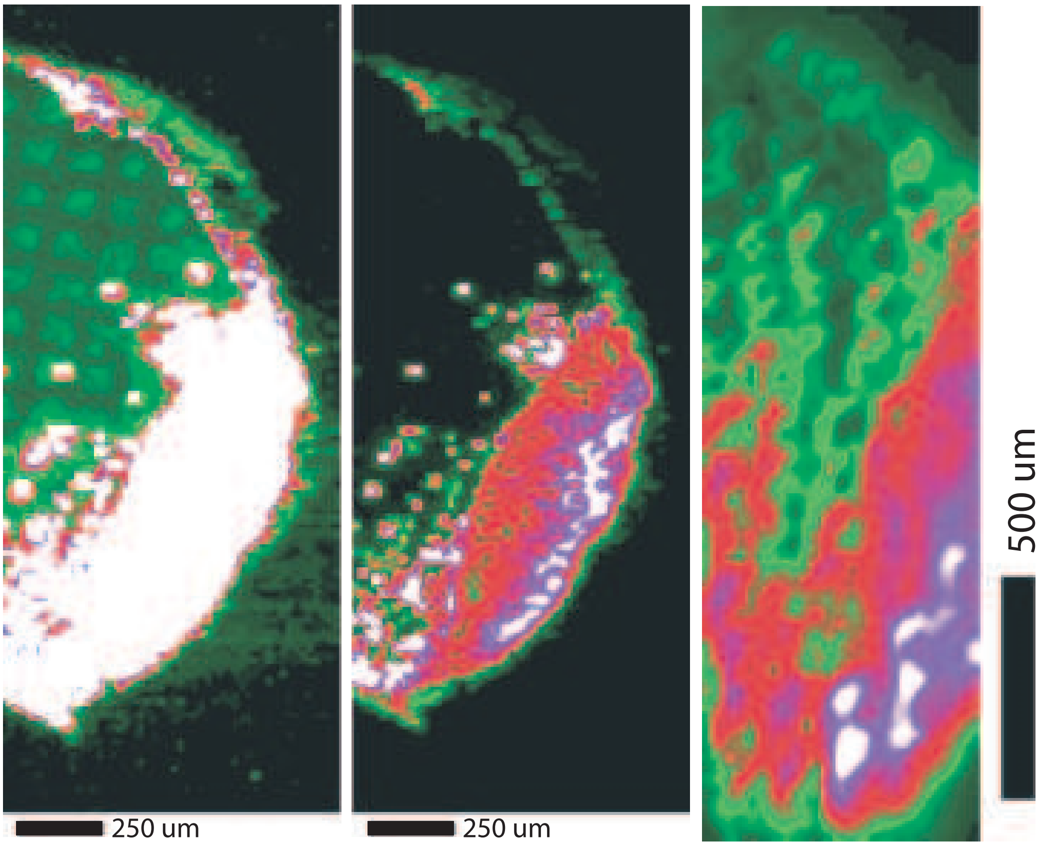

Figure 6.9: **(CdSe)ZnS Quantum Dots in a Wet Cell.**
A luminescence image of the empty wet cell at 520 eV scaled in such a way that the copper grid is visible (left). The signal results from an increased glass autofluorescence due to higher x-ray flux in the thin grid regions.
The same luminescence image of the empty wet cell at 520 eV but scaled such that it is comparable to the filled wet cell (middle).
A luminescence image of the filled wet cell at 520 eV (right). The P47 droplet signal is slightly changed, this may be due to decane that diffused through the glued connection and dissolved the phosphor or to mechanical influence.

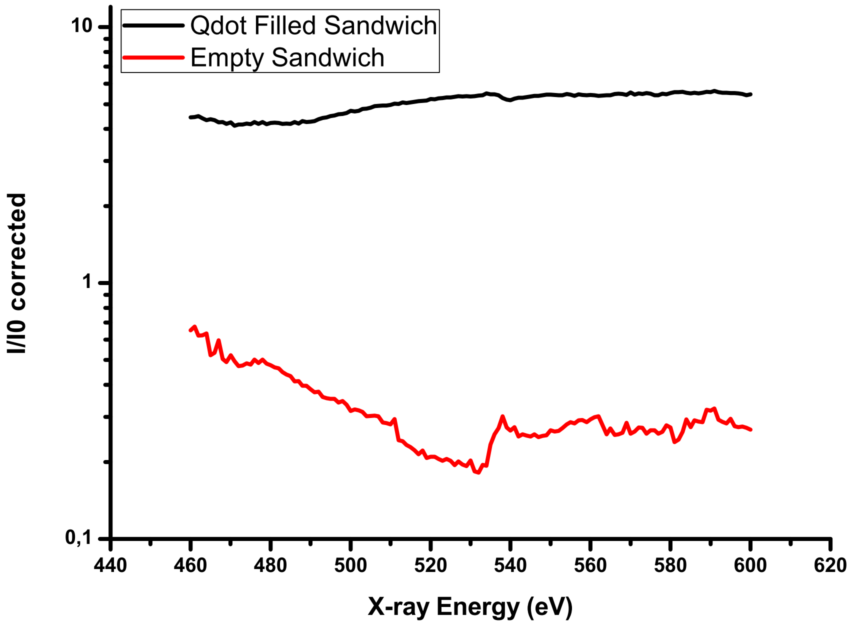

Figure 6.10: **X-ray Response of (CdSe)ZnS Nanocrystals Dissolved in Decane in Comparison to the Empty Wet Cell.** The spectra are corrected by the quantum yield of P47 $\propto E^{0.64}$. It appears that the quantum dot filled cell yields a higher visible light output, but the problems that emerged with the decane dissolving P47 and spreading it over the sample would give another explanation (see text).

UV/VIS/NIR Spectra of (CdSe)ZnS Nanocrystals in a Wet Cell

Unfortunately, experiments using the UV/VIS/NIR spectrometer were without any results. The qdots in decane solution were contained in wet cells of different thicknesses, from a couple of microns to about 2 mm (see figure 6.11). The sample was penetrated by soft x rays of various energies and at various fluxes. To make sure the spectrometer lens was well in place, a test sample was used for optimal alignment. To approve that the x-ray beam was actually hitting the sample, the proportional counter was used to collect the remaining photons that made it through the sample. In any case, even at very high integration times of about 1 s for the linear CCD array, there was no luminescence detected from the quantum dots.

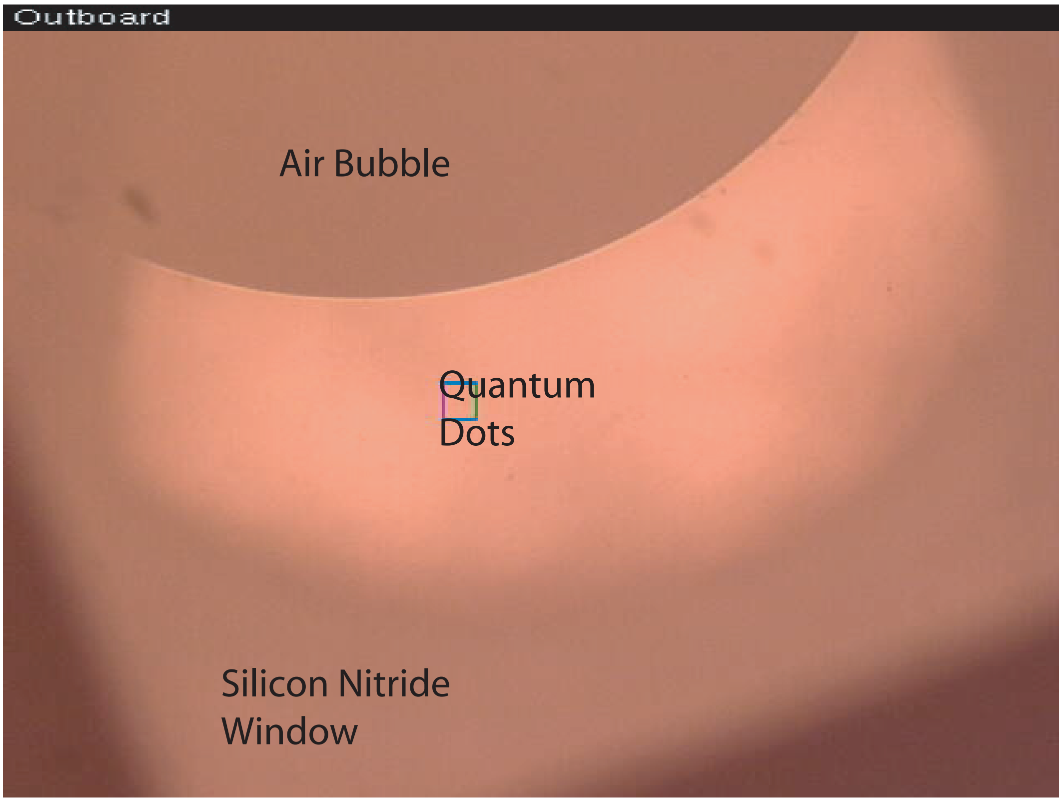

Figure 6.11: **Quantum Dots in a Large Volume Wet Cell.** Example for a sandwich that was created for a brute force experiment to check if there is any response coming from x-ray penetrated quantum dots. Two silicone nitride windows spaced by a 2 mm thick metal plate holds quantum dots in decane. Thereby, an air bubble was included on whose lower boundaries we focused in this visible light micrograph. Experiments did not lead to any results.

The Upper Boundary of the Quantum Efficiency

Of course, estimations about the actual quantum efficiency of the quantum dot nanoparticles with regards to soft x-ray excitation is only as good as the sensitivity of the detector. More precise, the signal to noise ratio is of significant importance. A rough estimation for the upper limit of the quantum yield of (CdSe)ZnS, using soft x-rays of about 500 eV, would be the following worst case scenario (see table 6.3). Assuming that in a low quality x-ray focus of 90 nm spot size with an illumination of about 10^6 photons per second, there would be at least one nanocrystal fully absorbing the incident radiation. This would correspond to about 3.1 kHz of absorbed photons. Estimating a really low performance quantum yield in the UV excitation range of about 15 % for uncapped nanocrystals (our qdots with luminescence of about 2.18 eV per photon are guaranteed to perform with a quantum efficiency of about 70 %), this would correspond to about 108.5 kHz of generated green photons of which 140 Hz will be recognized as a TTL pulse (see chapter 3.3.1). With typical dark counts of about 50 Hz, the signal to noise ratio therefore still would be around 2.7 and therefore the signal detectable. The limit where one could not see a significant signal any more is in the case where the signal to noise ratio is smaller or equal to one. Extrapolating back using the same principles as before, the quantum yield of (CdSe)ZnS nanoparticles can be placed below 5.6 % for soft x-rays. In reality, the quantum efficiency will be much lower: using a non-collimated UV excitation source to penetrate the qdots, the luminescence effect can be easily seen by the bare eye. Using bright x-ray undulator radiation on the other hand, this is not possible. Since the human eye usually works on a logarithmic scale, this indicates that the quantum efficiency might be at least one order of magnitude below this upper boundary. In any case, the luminescence of (CdSe)ZnS quantum dots due to soft x ray excitation is not a dominating effect and therefore not useful for SLXM.

I_{beam}	I_{qdot}	QY [%]	$\frac{\text{VIS}}{\text{x-rays}}$	I_{VIS}	$I_{\text{VIS det}}$	S/N
10^3	3.1	> 15	35	108.5	0.14	> 2.7
10^3	3.1	$\ll 5.6$	13	40	0.5	1

Table 6.3: **Quantum Yield of X-ray Excited (CdSe)ZnS Nanocrystals.** Expectations from our experiment are marked in blue, expectations of the behavior as it is known from UV excited quantum dots are marked in green and the corresponding estimations for upper boundaries are marked in red. I_{beam}, I_{qdot} and I_{VIS} are the total flux in the x-ray focus, on one quantum dot and the corresponding generated visible light photons, where only a fraction of $I_{\text{VIS det}}$ will generate a TTL pulse. S/N is the signal to noise ratio and QY the quantum yield.

Chapter 7

Conclusion

Throughout this work, some insight into the National Synchrotron Light Source at the Brookhaven Laboratory was given. After presenting the x-ray storage ring, some details about the undulator X1 and the beam line X1A with its x-ray microscopy end stations were discussed. The scanning transmission microscope was described as far as necessary to understand the terminology and methods throughout the rest of this paper. In the following, a new combined detection system for scanning transmission x-ray microscopy and scanning luminescence x-ray microscopy was presented. A scintillator screen combined with a light pipe and a photon counting head serves as an alternative to the other x-ray detectors now in use in the microscopes and the PMT detector turns out to be a reliable detector especially in the case of medium absorption contrasts and point spectra. The other configuration of the PMT detector where a microscope objective is installed, can be used to detect photons in the visible light range. A scintillator review furthermore discusses the internal working principle of x-ray converting scintillators focusing on three important materials: P31 - ZnS : Cu, P43 - Gd_2O_2S : Tb and P47 - Y_2SiO_5 : Ce. Screen deposition techniques as useful and necessary for the light pipe detector, were discussed. Moreover, the Photon Control SPM002-E Compact Spectrometer was presented in technical detail and its experimental setup was shown. A combined transmission/luminescence detector capable of scanning x-ray transmission and luminescence spectra at the same time, was proposed. With the help of the microscope objective/photomultiplier combination as well as with the spectrometer, it can be shown in the last part of this thesis that (CdSe)ZnS quantum dots are not useful for labeling in scanning luminescence x-ray microscopy as investigated at the NSLS.

Bibliography

[1] N. R. Comins, M. M. E. Hengstberger, and J.T. Thirlwall. Preparation and evaluation of P-47 scintillators for a scanning electron microscope. *J. Phys. E: Sci. Instrum.*, 11:1041–1047, 1978.

[2] Jan Warnking. Producing a thin, even, vacuum compatible phosphor layer on a small surface. One page protocol found at beam line X1A, September 1996.

[3] S. Tao, Z. H. Gu, and A. Nathan. Fabrication of Gd_2O_2S:Tb based phosphor films coupled with photodetectors for x-ray imaging applications. *J. Vac. Sci. Technol.*, A20(3):1091–1094, 2002.

[4] C. Jacobsen, S. Lindaas, S. Williams, and X. Zhang. Scanning luminescence x-ray microscopy: imaging fluorescence dyes at suboptical resolution. *Journal of Microscopy*, 172:121–129, 1993.

[5] Aihua Fu, Weiwei Gu, Carolyn Larabell, and A. Paul Alivisatos. Semiconductor nanocrystals for biological imaging. *Current Opinion in Neurobiology*, 15:568–575, 2005.

[6] *Qdot ®Nanocrystals: General Information.* Invitrogen Corporation, 1600 Faraday Avenue PO Box 6482 Carlsbad, California 92008, 2008.

[7] Jan Felix Steinbrener. Scanning luminescence x-ray microscopy exploring the use of quantum dot nanocrystals as high spatial resolution biological labels. Master's thesis, Stony Brook University, 2006.

[8] S. Fakra, A.L.D. Kilcoyne, and T. Tyliszczak. Scintillator detectors for scanning transmission x-ray microscopes at the advanced light source. *Synchrotron Radiation Instrumentation*, AIP Conference Proceedings (705):973–976, 2003.

[9] About the NSLS. `http://www.nsls.bnl.gov`. accessed on June 9th, 2008.

[10] C. Buckley, H. Rarback, R. Alforque, D. Shu, H. Ade, S. Hellman, N. Iskander, J. Kirz, S. Lindaas, I. McNulty, M. Oversluizen, E. Tang, D. Attwood, R. DiGennaro, M. Howells, C. Jacobsen, Y. Vladimirsky, S. Rothman, D. Kern, and D. Sayre. Soft x-ray imaging with the 35 period undulator at the NSLS. *Review of Scientific Instruments*, 60:2444–2447, 1989.

[11] A. M. Kondratenko and A. N. Skrinsky. Use of radiation of electron storage rings in x-ray holography of objects. *Optics and Spectroscopy*, 42: 189–192, 1977.

[12] C. Jacobsen and H. Rarback. Predictions on the performance of the soft x-ray undulator. In R. Tatchyn and I. Lindau, editors, *Insertion Devices for Synchrotron Sources*, volume 582, pages 201–212, Bellingham, Washington, 1985. Society of Photo-Optical Instrumentation Engineers (SPIE).

[13] S. Krinsky. Undulators as sources of synchrotron radiation. *IEEE Transactions: Nuclear Science*, NS-30:3078–3082, 1983.

[14] S. Krinsky, M. L. Perlman, and R. E. Watson. Characteristics of synchrotron radiation and of its sources. In E.-E. Koch, editor, *Handbook of Synchrotron Radiation*, volume IA, chapter 2, pages 65–171. North-Holland, Amsterdam, 1983.

[15] H. Rarback, C. Buckley, H. Ade, F. Camilo, R. DiGennaro, S. Hellman, M. Howells, N. Iskander, C. Jacobsen, J. Kirz, S. Krinsky, S. Lindaas, I. McNulty, M. Oversluizen, S. Rothman, D. Sayre, M. Sharnoff, and D. Shu. Coherent radiation for x-ray imaging—the soft x-ray undulator and the X1A beamline at the NSLS. *Journal of X-ray Science and Technology*, 2:274–296, 1990.

[16] H. Rarback, C. Buckley, K. Goncz, H. Ade, E. Anderson, D. Attwood, P. Batson, S. Hellman, C. Jacobsen, D. Kern, J. Kirz, S. Lindaas, I. McNulty, M. Oversluizen, M. Rivers, S. Rothman, D. Shu, and E. Tang. The scanning transmission microscope at the NSLS. *Nuclear Instruments and Methods in Physics Research A*, 291:54–59, 1990.

[17] B. Winn, H. Ade, C. Buckley, M. Feser, M. Howells, S. Hulbert, C. Jacobsen, K. Kaznacheyev, J. Kirz, A. Osanna, J. Maser, I. McNulty, J. Miao, T. Oversluizen, S. Spector, B. Sullivan, S. Wang, S. Wirick, and H. Zhang. Illumination for coherent soft x-ray applications: the new X1A beamline at the NSLS. *Journal of Synchrotron Radiation*, 7:395–404, 2000.

[18] W. Eberhardt, K. J. Randall, J. Feldhaus, A. M. Bradshaw, R. F. Garrett, and M. L. Knotek. The soft x-ray spectroscopy undulator beamline at NSLS X1. *Physica Scripta*, 41:745–748, 1990.

[19] B. Hornberger. *Phase Contrast Microscopy with Soft and Hard X-rays Using a Segmented Detector.* PhD thesis, Department of Physics and Astronomy, Stony Brook University, 2007.

[20] Douglas Vaughan Thompson Albert C. et al. X-ray data booklet. Lawrence Berkeley National Laboratory University of California Berkeley, California 94720, January 2001.

[21] J. Kirz. Phase zone plates for X rays and the extreme UV. *Journal of the Optical Society of America*, 64:301–309, 1974.

[22] Y. Wang. *Three-dimensional imaging in soft x-ray microscopy.* PhD thesis, Department of Physics and Astronomy, State University of New York at Stony Brook, 1998.

[23] M. Feser. *Scanning transmission x-ray microscopy with a segmented detector.* PhD thesis, Department of Physics and Astronomy, Stony Brook University, 2002.

[24] C. Jacobsen, G. Flynn, S. Wirick, and C. Zimba. Soft x-ray spectroscopy from image sequences with sub-100 nm spatial resolution. *Journal of Microscopy*, 197(2):173–184, 2000.

[25] Hamamatsu Photonics K. K. Editorial Committee. *Photomultiplier Tubes - Basics and Applications.* Hamamatsu Photonics K. K., third edition, 2006.

[26] Glenn F. Knoll. *Radiation detection and measurement.* John Wiley & Sons, Inc., first edition, 1979.

[27] *Photomultiplier Handbook.* BURLE INDUSTRIES, INC, 1980.

[28] *Head-On Integrated Photon Counting Head H6180-01.* Hamamatsu Photonics K.K., Electoron Tube Center, 314-5, Shimokanzo, Toyooka-village, Iwata-gun, Shizuoka-ken, 438-0193, Japan, 1996.

[29] P. Horowitz and W. Hill. *The Art of Electronics.* Cambridge University Press, 2nd edition, 1989.

[30] J. B. Birks. *The Theory and Practice of Scintillation Counting.* The Mac Millan Company, 1964.

[31] E. M. Gullikson, R. Korde, L. R. Canfield, and R. E. Vest. Stable silicon photodiodes for absolute intensity measurements in the VUV and soft x-ray regions. *Journal of Electron Spectroscopy and Related Phenomena*, 80:313–316, 1996.

[32] B. L. Henke, P. Lee, T. J. Tanaka, R. L. Shimabukuro, and B. K. Fujikawa. Low-energy x-ray interaction coefficients: photoabsorption, scattering, and reflection. *Atomic Data and Nuclear Data Tables*, 27:1–144, 1982.

[33] B. L. Henke, E. M. Gullikson, and J. C. Davis. X-ray interactions: Photoabsorption, scattering, transmission, and reflection at E=50–30,000 eV, Z=1–92. *Atomic Data and Nuclear Data Tables*, 54:181–342, 1993.

[34] T. Tanaka, C. Makochekanwa, H. Tanaka, M. Kitajima, M. Hoshino, Y. Tamenori, E. Kukk, X. J. Liu, G. Prümper, and K. Ueda. Symmetry-resolved absorption spectra of vibrationally excited CO_2 molecules. *Physical Review Letters*, 95:203002–1–203002–4, 2005.

[35] Y. Ma, C. T. Chen, G. Meigs, K. Randall, and F. Sette. High-resolution K-shell photoabsorption measurements of simple molecules. *Physical Review A*, 44(3):1848–1858, 1991.

[36] Spectroscopy applications - luminescence and fluorescence spectroscopy. `http://www.piacton.com/Spectroscopy`, 2007. accessed on May 22nd, 2008.

[37] Wikipedia: The free encyclopedia. `http://en.wikipedia.org/wiki`. accessed on June 10th, 2008.

[38] S. E. Derenzo, M. J. Weber, E. Bourret-Courchesne, and M. K. Klintenberg. The quest for the ideal inorganic scintillator. *Nuclear Instruments and Methods*, in press, 2002.

[39] I.L. McNulty. *X-ray Fourier transform holography: beyond the optical diffraction limit.* PhD thesis, Department of Physics, State University of New York at Stony Brook, 1991.

[40] Shigeo Shionoya and William H. Yen. *Phosphor Handbook.* Phosphor Research Society, 1999.

[41] B. X. Yang, J. Kirz, and S.Xu. Characterization of phosphors in the soft x-ray region. *Nuclear Instruments and Methods in Physics*, A258:141–145, 1987.

[42] N. Karar and Harish Chander. Luminescence properties of cerium doped nanocrystalline yttrium silicate. *J. Phys D: Applied Physics*, 38:3580–3583, 2005.

[43] S. Ves, U. Schwarz, N. E. Christensen, K. Syassen, and M. Cardona. Cubic ZnS under pressure: Optical-absorption edge, phase transition, and calculated equation of state. *Physical Review B*, 42(14):9113–9118, 1990.

[44] E. I. Gorokhova, V. A. Demidenko, S. B. Mikhrin, P. A. Rodnyi, and C. W. E. van Eijk. Luminescence and scintillation properties of Gd_2O_2S:Tb,Ce ceramics. *IEEE Transactions On Nuclear Science*, 52: 3129–3132, 2005.

[45] M. H. Cho, D. H. Ko, J. G. Seo, S. W. Whangbo, K. Jeong, I. W. Lyoa, C. N. Whang, D. Y. Noh, and H. J. Kim. Characteristics of Y_2O_3 films on Si(111) grown by oxygen-ion beam-assisted deposition. *Thin Solid Films*, 382:288–296, 2001.

[46] *Photon Control - SPM002 Compact Spectrometer - User Guide*. Photon Control Inc., Burnaby, B.C., Canada, 2.2.9 edition, March 2008.

[47] *Toshiba CCD Linear Image Sensor TCD1304DG*. TOSHIBA CORPORATION, 2004.

[48] *SPM002 Compact Spectrometer - Dynamic Link Library (DLL) Software Development Kit Guide*. Photon Control Inc., 1.5 edition, August 2006.

[49] Victor I. Klimov, editor. *Semiconductor and Metal Nanocrystals: Synthesis and Electronic and Optical Properties*. Marcel Dekker Inc., 2004.

[50] Fang-I. Lai, S. Y. Kuo, J. S. Wang, R. Hsiao, H. C. Kuo, J. Chi, S. C. Wang, H. S. Wang, C.T. Liang, and Y.F. Chen. Temperature-dependent optical properties of In0.34Ga0.66As1-xNx/GaAs single quantum well with high nitrogen content for 1.55 μm application grown by molecular beam epitaxy. *Crystal Growth*, 291(1):27–33, May 2006.

[51] S. Franchi, G. Trevisi, L. Seravalli, and P. Frigeri. Quantum dot nanostructures and molecular beam epitaxy. *Crystal Growth*, 47(2-3):166–195, 2003.

[52] Michael Bowker. The going rate for catalysts. *Nature Materials*, 1:205–206, 2002.

[53] C. B. Murray, D. J. Norris, and M. G. Bawendi. Synthesis and characterization of nearly monodisperse CdE (E=S, Se, Te) semiconductor nanocrystallites. *J. Am. Chem. Soc.*, 115:8706–8715, 1993.

[54] H. Borchert, D. V. Talapin, C. McGinley, S. Adam, A. Lobo, A. R. B. de Castro, T. Möller, and H. Weller. High resolution photoemission study of CdSe and CdSe/ZnS core-shell nanocrystals. *J. Chem. Phys.*, 119(3): 1800–1807, 2003.

[55] Ben G. Streetman. *Solid State electronic Devices*. Sanjay Banerjee, 5 edition, 2000.

[56] J. D. Jackson. *Classical Electrodynamics*. John Wiley & Sons, New York, second edition, 1975.

[57] M. J. Berger, J. H. Hubbell, S.M. Seltzer, J. Chang, J.S. Coursey, R. Sukumar, and D.S. Zucker. XCOM: Photon cross sections database. *NIST Standard Reference Database 8 (XGAM)*, 1990.

[58] A. Thompson et al. X-ray data booklet. Lawrence Berkeley National Laboratory, University of California, Berkeley, CA 94720, January 2001. Online at `http://xdb.lbl.gov/`.

[59] James E. Downes. *Soft X-ray Spectroscopic Studies of the Electronic Structure of Organic Molecular Superconductors and Semiconductors*. PhD thesis, Boston University, 2004.

[60] Holger Borchert, Dmitri V. Talapin, Nikolai Gaponik, Colm McGinley, Sorin Adam, Arun Lobo, Thomas Möller, and Horst Weller. Relations between the photoluminescence efficiency of CdTe nanocrystals and their surface properties revealed by synchrotron XPS. *J. Phys. Chem. B*, 107: 9662–9668, 2003.

[61] F. Niederdraenk, P.Luczak, K. Seufert, C.Kumpf, R.Neder, S.Dembski, C.Graf, E.Rühl, and E.Umbach. X-ray diffraction on core-shell nanoparticles for a precise structure determination.

[62] *Model 740A/D Optical Radiation Measurement System*. Optroncis Laboratories Inc., 36th Street, Orlando, Florida, 32611 USA, March 1984.

[63] Glen D. Gillen and Shekhar Guha. Use of michelson and fabryperot interferometry for independent determination of the refractive index and physical thickness of wafers. *Applied Optics*, 44(3):344–347, January 2005.

Appendix A

Miscellaneous

During the progression of the project, there were several occasions where results turned out different from what was expected. Specifically, the experimental setup which comprised the spectrometer as described in chapter 5, was initially designed as a more complex but much less effective setup. To be more precise, the plan was to built a photoluminescence experiment out of already purchased components. But, after several attempts at trying to use the already existing equipment, it was decided to purchase a new spectrometer.

A.1 The Original Idea

The original idea for an experimental setup to measure the photoluminescence of quantum dots and phosphors can be seen in figure A.1. The image shows the concept of the measurement using an excitation in the visible light range (here the 532 nm NdYAG-laser or another concentrated VIS/UV light source). The laser beam is directed and focused to a sample of luminescent material. Then, the reflected laser beam as well as the luminescence signal is passed into a Czerny-Turner monochromator through an entrance slit (typical slit size: 50 μm), this partially determines the resolution of the obtained spectrum. The signal is detected by a detector following the exit slit of the apparatus. The monochromator can be controlled by a computer which simultaneously reads in the wavelength as well as the detector signal and so yields a spectrum. For a better signal to noise ratio, the laser beam was chopped by a radially segmented wheel, whose turning frequency triggers a so called

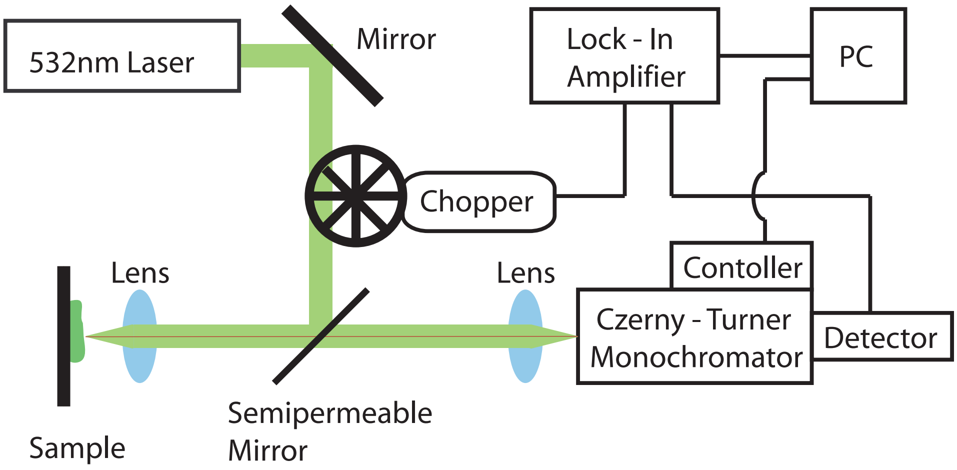

Figure A.1: **Initial Idea for an Experimental Setup to Measure the Photoluminescence of Quantum Dots.** An excitation source (here: 532 nm laser) is chopped by a wheel and focused onto a sample. The reflection as well as the luminescence signal are passed into a Czerny-Turner monochromator and collected by a detector on the other end. A Lock-In amplifier in combination with a controller and a data acquisition environment help to record low noise spectra automatically.

Lock-In amplifier. This amplifier filters the incoming detector signal according to the chopper triggering. The experimental data shown in chapter 6.3 *e.g.* was obtained by a similar assembly.

A.2 The Monochromator

After quite some work, it actually turned out to be the monochromator limiting the outcome of the whole experimental approach and therefore leading to a decision to try another approach. The device that was borrowed for the initial experimental setup was a 23 year old instrument, with an interface for an old Hewlett Packard, a Model 740A/D monochromator in combination with a Model 740-1C wavelength drive built by Optronics Laboratories Inc. [62]. The setup contains a double monochromator, with two diffraction gratings inside it. The Czerny-Turner configuration (see figure 5.2) includes two concave mirrors and a plane grating configured in the shape of the letter “M”. Behind each of the slits is a 45 ° mirror providing an in-line path for source and output. This classic design is widely used due to its aberration correcting properties and in our case provides a spectral range of 280 to 1070 nm. The 1200 groves/mm grating with a typical blaze wavelength of 500 nm should provide a dispersion of about 2.0 nm/mm. Typical slit widths of 0.5 mm, 1.25 mm, 2.5 mm and 5 mm would correspond to spectral band passes of 1 nm, 2.5 nm, 5 nm and 10 nm respectively. Without slits the bandpass would be around 25 nm. By means of a worm drive DC motor, the angles of the gratings can be altered and therefore the spectral range scanned continuously. For wavelength position feed back, the motor is coupled to a revolutions counter via a rubber belt. These counting pulses are sent to the control device "wavelength drive", which also regulates the speed and direction of the motor or in other words the direction of the wavelength scanning process. There is a BCD connector on the rear of the OL 740-1C wavelength drive controller receiving signals from the optical encoder attached to the monochromator wavelength drive. The wavelength encoder positions are read out in 17 bits where there are 4 times four bits encoding the decimals 0.1, 1, 10 and 100 nm and the last one to encode the 1000 nm. To control the monochromator, there are four input bits functions, "NEUTRAL", "START", "SLOW", "DECREASE", "STOP", "INCREASE" and "FAST". The read out of the wavelength as well as the control and the data acquisition of the detector were done by an UEIDAQ board in combination with a computer and an adapted LABVIEW example program. Unfortunately, the board used only had 8 digital inputs. So, even after applying several different configurations, the wavelength read out remained unreliable and the calibration a very complicated procedure. However, the motor control worked quite well and satisfactory. Some problems were encountered due to material aging effects. Due to the age of the equipment, several of the mechanical components, such as rubber belts and the brass worm had to be replaced. Furthermore, items such as the slits and adapters had to be machined anew and new cables had to be installed. Crucial parts, like the mirrors and the gratings, had oxidized over years and were not replaceable. Another issue would also have been the time one single spectrum would have taken to collect. A full wavelength range scan would have taken one minute in the best case, which is significantly slower then the spectrometer finally purchased for this project 5. The signal would have to have been filtered to diminish noise issues which justifies the whole experimental setup in figure A.1. The noise problem could have been solved by simple averaging over time and adjustment of exposure times as is done in new spectrometers, but the installation of this detector into the STXM at Brookhaven was not straight forward. Coupling the light into the spectrometer via a fiber would have been significantly harder than what was finally used which was a SMA connector; the loss of photons would have been unreasonable. Also, the size and weight of this equipment, 7.3 kg of the monochromator alone, not including the controller, the Lock-In amplifier, the chopper, the data acquisition cards and equipment to interface to, simply made it impossible to fit into the STXM and its circumference. All this could be accomplished by a 475 g USB spectrometer of the size of a cup. The affordable price and user friendliness of the state of the art spectrometers therefore justified the purchase of a new detector.

A.3 The Chopper Wheel

In order to chop the excitation laser beam at a constant frequency and therefore create a reference signal for the Lock-In amplifier to be able to filter the signal from background noise, a chopper wheel was needed. Since a well working application couldn't be found, a chopper circuit using a 5 V DC motor, a radially spaced blade and some electronic components as shown in figure A.2, was designed.

As it can be inferred from the wiring diagram, the circuit consists of two major parts. The transistor to control the motor frequency and a photoelectric barrier to generate the trigger signal. An inverter to invert and stabilize the output signal as well as a voltage regulator for a more precise regulation of the motor speed within a broader range might still be implemented for better results.

A.4 The Goniometer

A rotatable potentiometer with a resistance range of 50 kΩ within one single 360° revolution was mechanically combined with a circular nonius of 1/60° accuracy and a 5 VDC power supply. (see figure A.3) After calibration, it was possible to electronically read out angles with a precision of about 1/6° via a 0 to 5 VDC analog voltage. This device initially was meant to be able to rotate thin layered samples in the focus of a coherent laser beam. A Fabry-Perot-Interferometer technique as described by Gillen *et al.* [63] would have allowed to measure the thickness of the thin film by evaluating oscillations in an intensity-over-angle data set.

Except for trial and calibration measurements, this device was never used

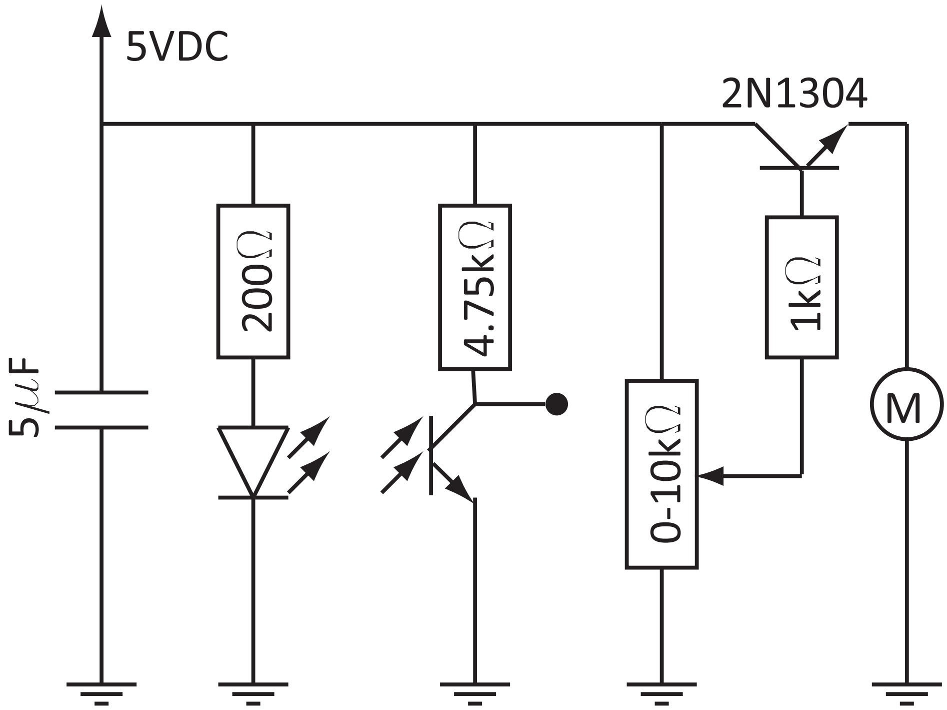

Figure A.2: **Electronic Circuit of the Chopper Wheel with TTL Output.** A capacitive stabilized 5 VDC source supplies a light barrier and a motor. The light barrier generates the pulse output, the motor that drives the chopper wheel can be roughly controlled in frequency.

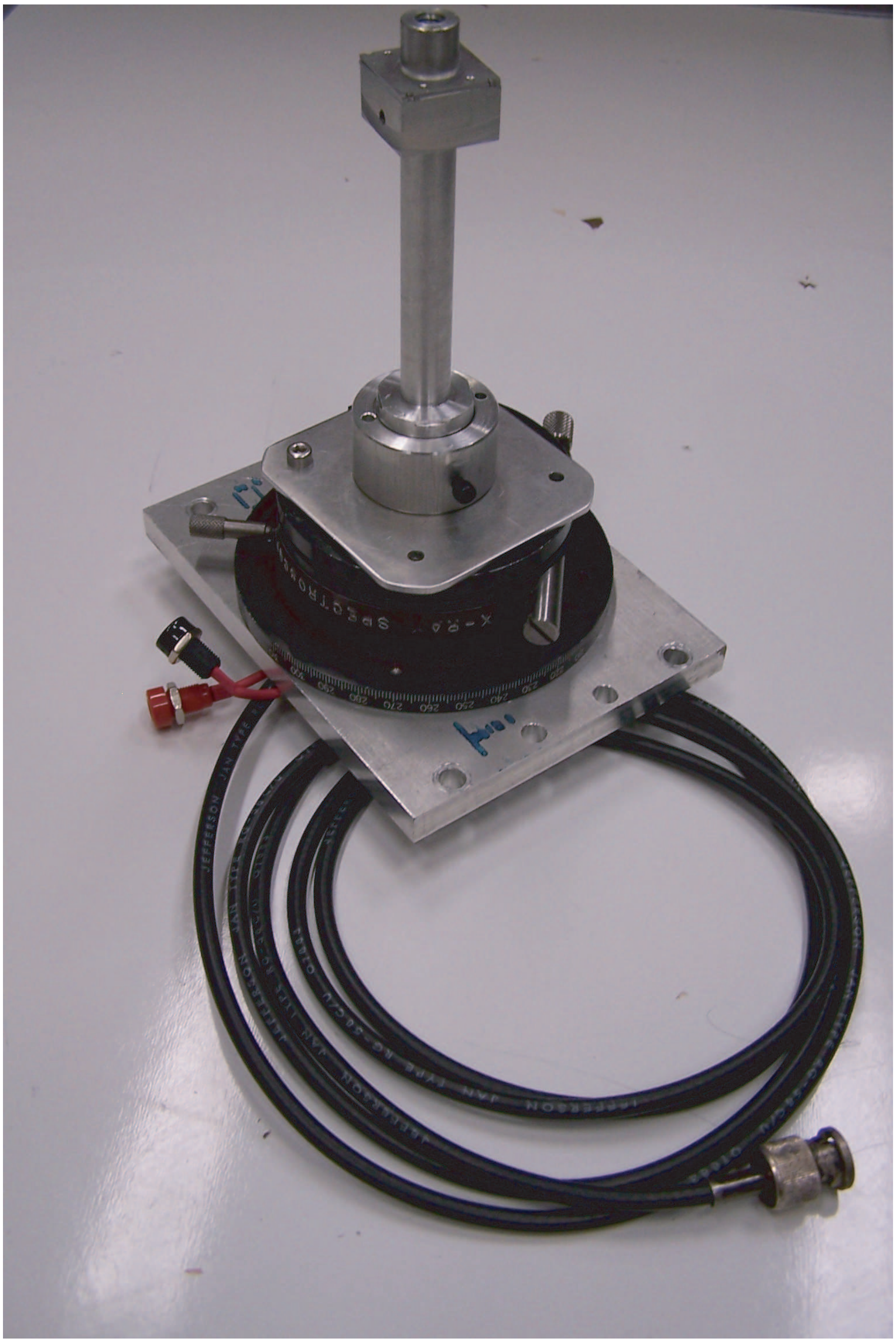

Figure A.3: **Photograph of the Goniometer.** A rotatable potentiometer with a resistance range of 50 kΩ within one single 360° revolution was mechanically combined with a circular nonius of 1/60° accuracy and a 5 VDC power supply.

for thickness measurements. The original idea was to use the goniometer to measure the thickness of wet cell samples used in the STXM but due to layer inhomogeneity of the wet cell this measurement was not feasible. Nevertheless this device might be applied to other tasks in the future.

Appendix B

Scintillator Screen Deposition

To form an efficient, uniform layer of phosphor on a substrate is not a simple task. In the following, we present four methods to deposit scintillators on a substrate. Some of these methods were used in this thesis work, some were not, some have been published, others were obtained through personnel communications.

B.1 P47 and Gelatin: Protocol by Comins *et al.* [1]

For a grain size distribution maximum of about 2.5μm the author used a P47 density in the range from $14 - 25$gm^{-2} and a gelatin density of 1.6gm^{-2} $-$ 2gm^{-2} which corresponds to 0.05 wt% in aqueous solution. P47 powder is ultrasonically dispersed in a low concentration solution of gelatin in distilled water. The suspension is applied in the form of a drop on the desired substrate and completely dried out by air.

Too much gelatin degrades the scintillator performance. The light output, although increasing with surface coverage at low screen densities, begins to decrease again for screen densities greater than about 15gm^{-2} and this can be attributed to light absorption and scattering losses in the thicker layers.

The P47 phosphor screens obtained by this procedure did not show mechanical deterioration after several months.

B.2 P31 and Water Glass: Protocol by Warnking *et al.* [2]

1 g of P31 phosphor is dispersed in water glass (Na silicate • $9H_2O$) (1 g in 200 ml of water)

After complete dissolution, the solution is stirred. Once the solution is well stirred, one waits for 10 min to let coarse grains settle (only the small grains are used to form the screen). Place the substrate into the solution so there is approximately 2 inches of water above the surface. (The surface has to be kept level in the horizontal plane to avoid washing the phosphor off while the overlying solution is drained.) After about 50 min the phosphor has settled out and one can carefully drain the supernatent. The scintillator is air dried over night.

The resulting layer is a monolayer of P31. If one waits 6.5 instead of 10 min, one gets 2 to 3 layers with about 90 to 95 % coverage.

To make the scintillator surface resistant to abrasion one needs to increase the concentration of the water glass. Also, water glass is hygroscopic so screens made using this method have to be kept dry.

B.3 Self Assembled Monolayer (SAM) with P47: Protocol by Tamas Haraszti

This method is an approach recommended by Tamas Haraszti from the University of Heidelberg. For a further development of this method, all parameters would have to be adjusted and several experiments undertaken to improve the resultant scintillator screen. Because of the extreme toxicity of chemicals needed for this method and because for our application a precise layer by layer structure is not needed, this method was never tried but may prove useful for future applications.

- Clean the substrate (glass) with piranha (Caro acid: mixture of 30 % hydrogen peroxide H_2O_2 and 70 % concentrated sulfuric acid H_2SO_4 in a ratio of 1/3. Always add H_2SO_4 to H_2O_2 and not vice versa! Read carefully the safety data sheets and use exhausts and saftey equipment!

- Dip substrate in $\sim 2\%$ PDDA (poly(diallyldimethylamonium)) solution for ~ 5 min, then
- rinse the substrate with water (use milliPore/MilliQ water with ~ 18 MΩ/cm resistance).
- Blow the substrate carefully dry with nitrogen gas, then
- prepare and shake up a $\sim 1 - 2\%$ P47 in PDDA suspension.
- Dip substrate in particle suspension for approx ~ 5 min, then
- rinse substrate ~ 5 min or dip it into fresh water 3×5 min and change water every time.
- Blow substrate carefully dry with nitrogen gas.
- Repeat this procedure as often as necessary.

B.4 Self Assembled Monolayer (SAM) with P43: Protocol by Tao *et al.* [3]

This method was designed specifically for P43: $Gd_2O_2S : Tb$ self assembled monolayers have been studied by Tao *et al.* [3] and the essence of this phosphor film fabrication shall be summarized here. The main components are P43-$Gd_2O_2S : Tb$ phosphor powder, polyvinyl alcohol (PVA) and H_2O coupled with a few organic additives. The fabrication works as the following:

- Prepare a coating solution by dissolving $3 - 10$wt% PVA into deionized water at $85 - 95$°C with proper agitation to avoid dead zones where PVA could agglomerate, then
- let PVA fully dissolve.
- Cool solution naturally down to room temperature and pour it into a vertical cylindrical, flat-bottomed glass vessel for mixing with phosphor particles.
- Stir solution and introduce a small amount of additives followed by gradual addition of weighted phosphor particles (The overall mixing process

must be subject to agitation until the phosphor particles are able to fully disperse into the polymer matrix. The rate of agitation plays a critical role. It must yield enough centrifugal force to keep the phosphor particles suspended in solution for dispersion. Meanwhile over agitation should be avoided since it can generate a large volume of foam that may remain and entrain into the film later.) Agitation rates are between $600 - 1300$ rpm dependent on particle sizes and PVA concentrations Agitation is terminated when the particles are fully dispersed and then a homogeneous coating system is achieved.

- The solution is then immediately but slowly transferred into a settling cylinder. The cylinder has a high aspect ratio (wall/diameter = 8/1) and a transparent wall to visually monitor the phase separation (During the sedimentation process, the phosphor particles are separated by gravity. On top of the solution is the transparent polymer solvent where phosphor particles have been fully separated from the solution, while at the bottom is a homogeneous phosphor solution. Between these two phases, a phase separation interface is formed where the sedimentation process is taking place. The sedimentation velocity is directly proportional to the weights of the phosphor particles that are related to particle sizes and inversely proportional to solution viscosity.)
- When all of the particles have settled, the phosphor-coated substrate must be removed and cured in a fume hood with controlled humidity and temperature

One single coating process can achieve film thickness of over 250 μm. The conversion efficiencies increase significantly when particle sizes change from 2.5 to 10 μm and somewhat saturate as the particle size is further increased.

B.5 Washing (CdSe)ZnS nano crystals

The following protocol as recommended by Invitrogen [6] was used slightly modified in order to wash the quantum dots from an extent of stabilizing agents (TOP, TOPO).

- Add a 4× volume of a 75/25 methanol/isopropanol mixture to a 1× volume of quantum dots in organic solution (ethanol also works; in general use a high volume of washing agent)

- Mix well and place in a sealable centrifuge tube, seal and centrifuge for 3 - 5 minutes at 3000 rpm.
- Discard the supernatant and re-disperse the pellet in the chosen organic solvent.

Appendix C

PMT Detector Use and Maintenance

C.1 Renewal of a Light Pipe

After extensive use, especially when the scintillator screens have been changed, the tips of the light pipe (LP) will need to be re-polished. The following procedure is for the fabrication of new light pipes, for the re-polishing of already fabricated light pipes ignore the first and the last two steps:

- use lucite rods, favorably in standard diameters
- cut LP to desired length
- sand LP with 400 sandpaper
- sand LP with 500 sandpaper
- sand LP with 1500 sandpaper
- polish LP with polishing agent (*e.g.* "Novus Fine Scratch Remover") on several layers of "KIMWIPE"
- prepare right sized center hole in lucite 1 1/3" flange adapter
- position the light pipe and glue it in tightly (*e.g.* with "Weld-On #16clear,

Thickened Cement for Acrylic” by IPS Corp. sheet)

All the sanding has to take place on a flat surface, so the lucite rods have to be mounted in such a way as to keep them stable and the tip flat during polishing.

C.2 Recovery of Helium Tightness

Helium penetrating the photomultiplier housing can cause after pulsing which is a phenomenon where the PMT produces a secondary pulse due to ionization of helium atoms and therefore results in the detector over counting. It is therefore paramount that the detector is sealed from any helium environment. To accomplish this the following procedure was used:

- prepare clean working environment and avoid dirt and dust
- prepare ethanol, “KIMWIPE”, allen keys and a fresh bag of silica gel
- loosen the 2 3/4” conflate flange/BNC connector feed through assembly at the back of the detector: (Attention! This is spring loaded!)
- take off the BNC connector assembly including complete photon counting head, silica bag and spring
- take off and detach the complete front of the detector
- clean all stainless steel parts carefully with ethanol and “KIMWIPE” cloths
- replace or clean all rubber gaskets and lubricate them with vacuum grease
- replace silica bag
- check electrical insulation of the spring
- rebuild everything in reverse order, taking care of the cable connections between PMT and BNC connector

- tighten all screws in starlike order and make sure the gaskets seal (for the light pipes, no high pressure is needed)

C.3 Change from Microscope Objective Option to Light Pipe Option

- prepare clean working environment and avoid dirt and dust
- prepare ethanol, “KIMWIPE”, allen keys and optical grease
- prepare light pipe according to C.1
- detach everything that is placed upstream to the 2 3/4” to 1 1/3” flange adapter
- clean stainless steal parts with ethanol
- replace or clean all rubber gaskets and lubricate them with vacuum grease
- carefully clean the photomultiplier window with ethanol and “KIMWIPE” cloths through the flange adapter hole, check that there is no dust left on the window
- put a small drop of optical grease on the downstream tip of the light pipe
- attach light pipe to the adapter, one should feel a decent pressure coming from the spring load
- illuminate the light pipe using a lamp, one should clearly see the photocathode of the photomultiplier

C.4 Change from Light Pipe Option to Microscope Objective Option

- prepare clean working environment and avoid dirt and dust

- prepare ethanol, “KIMWIPE” and allen keys
- detach everything that is placed upstream to the 2 3/4” to 1 1/3” flange adapter, don’t scratch the tip of the light pipe
- clean stainless steal parts with ethanol
- replace or clean all rubber gaskets and lubricate them with vacuum grease
- carefully clean the photomultiplier window with ethanol and “KIMWIPE” cloths through the flange adapter hole, try to avoid spreading the optical grease and check that there is no dust left on the window
- attach glass window and the objective slide to the adapter
- slide the microscope objective mounted on the objective carriage on the slide and move it as far downstream as possible
- adjust the telescope after the detector is installed into the microscope and always check clearance to the piezo stage

C.5 Detector Dimensions

In the following, some crucial detector dimensions are shown. Since the detector was developed in an “on the flight” kind of way, the drawings were made after the detector was built up. The author recommends to confirm these values previous ordering replacement parts.

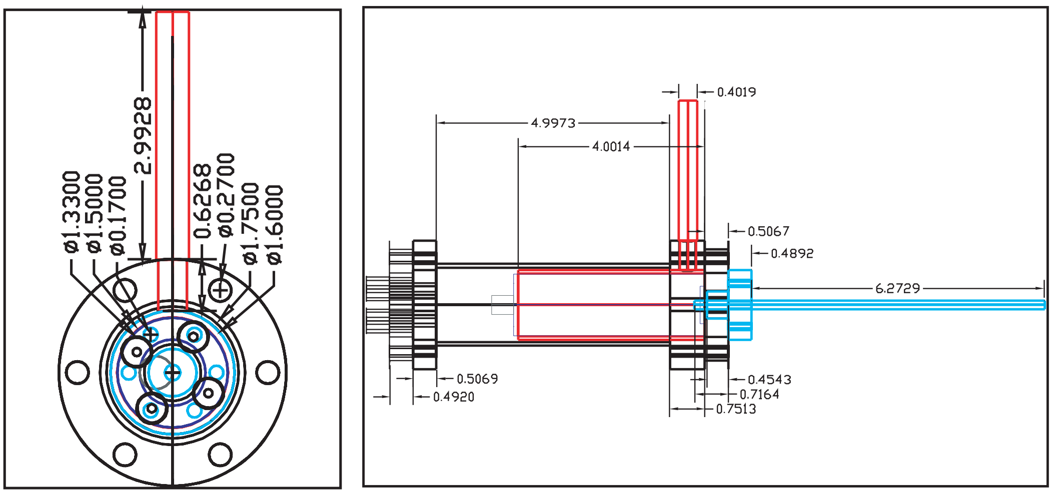

Figure C.1: **CAD Drawing of the Light Pipe Detector: Dimensions.** (All dimensions are indicated in inch.)
Dimensions in the frontal plane of the detector (left).
Dimensions in the side plane of the detector (right).

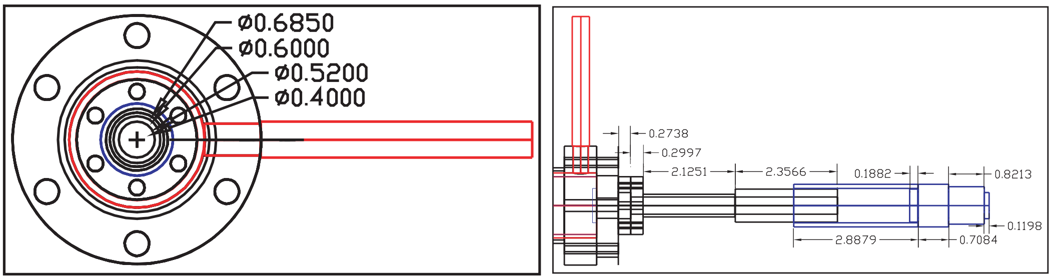

Figure C.2: **CAD Drawing of the Microscope Objective Detector: Dimensions.** (All dimensions are indicated in inch.)
Dimensions in the frontal plane of the detector (left). These are especially the diameters of the objective slide and the objective mount.
Dimensions in the side plane of the detector (right). The back part does not change from light pipe to microscope objective option and is shown in figure C.1.

Appendix D

Using the Spectrometer in STXM: Lens Alignment

As described in chapter 5, the SPM002-E can be used to examine x-ray excited luminescence. The signal is collected by a collimating lens, coupled into a fiber, and feeded out of the microscope chamber to the spectrometer. Since, at the moment, it is not connected to the microscope control at all, alignment of the lens has to be undertaken differently. Following procedure proved to be useful:

- Check the lens and fiber mount being fixed to the detector stage (*e.g.* the space designated for the counter detector)(see figure D.1 left).
- Completely retract the lens-tube.
- Insert an empty sample mount, insert an x-ray detector and align the sample mount in x-ray focus.
- Insert the lens ("Insert Counter") and move it approximately into focus, using "Move Detector" for x- and y-direction and your hand, to adjust the z-direction.
- Replace the empty sample mount by a sample mount with a LED (see figure D.1 right), the LED faces the upstream direction.
- Monitor the LED signal (Gaussian peak: $\sim$ 566 nm, FWHM $\sim$ 27 nm) on the spectrometer and adjust x- y- and z- directions until the highest signal can be reached (typically a signal of 950 should be possible with

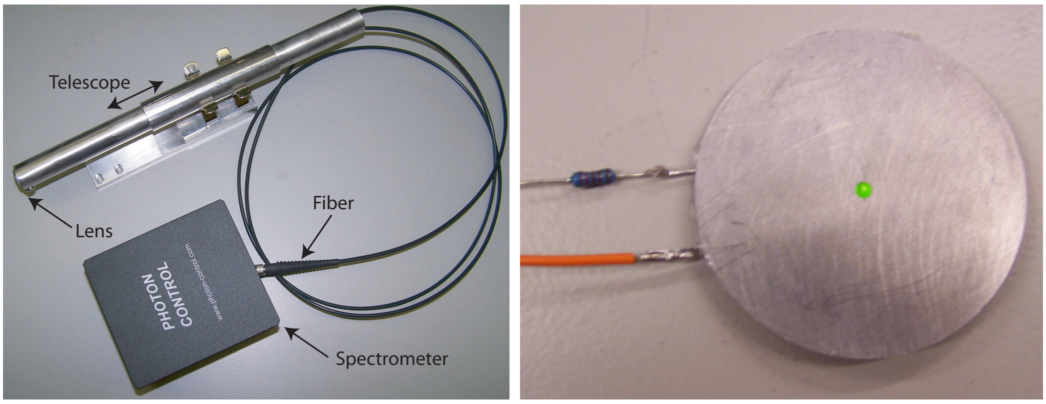

Figure D.1: **The Fiber Spectrometer Setup.**
The Spectrometer with fiber and lens mounted on a detector platform that is adjustable in beam direction (left).
The Lens alignment tool (right). After the x-ray beam is aligned to the sample stage, this device is inserted and the green LED illuminated. The lens is inserted into the piezo stage and its position adjusted by maximizing the signal of the diode (Gaussian peak: $\sim$ 566 nm, FWHM $\sim$ 27 nm) on the SPECSOFT screen using the command "MOVE" in sm_gui.

an exposure time of 100 ms)

- Record Detector aligned